

Summer 2021

Polyaromatic-Terminated Iron Polypyridyl Complexes For The Functionalization Of Carbon Surfaces And Electrocatalytic Hydrogen Generation

Caroline Marie Margonis

William & Mary - Arts & Sciences, carolinemaronis@gmail.com

Follow this and additional works at: <https://scholarworks.wm.edu/etd>

 Part of the [Chemistry Commons](#)

Recommended Citation

Maronis, Caroline Marie, "Polyaromatic-Terminated Iron Polypyridyl Complexes For The Functionalization Of Carbon Surfaces And Electrocatalytic Hydrogen Generation" (2021). *Dissertations, Theses, and Masters Projects*. Paper 1627047877.

<http://dx.doi.org/10.21220/s2-6z54-np26>

This Thesis is brought to you for free and open access by the Theses, Dissertations, & Master Projects at W&M ScholarWorks. It has been accepted for inclusion in Dissertations, Theses, and Masters Projects by an authorized administrator of W&M ScholarWorks. For more information, please contact scholarworks@wm.edu.

Polyaromatic-Terminated Iron Polypyridyl Complexes for the Functionalization of
Carbon Surfaces and Electrocatalytic Hydrogen Generation

Caroline Marie Margonis

Charlotte, North Carolina

Bachelor of Science, The University of North Carolina at Chapel Hill, 2018

A Thesis presented to the Graduate Faculty of The College of William & Mary in
Candidacy for the Degree of
Master of Science

Department of Chemistry

College of William & Mary
May 2021

APPROVAL PAGE

This Thesis is submitted in partial fulfillment of
the requirements for the degree of

Master of Science

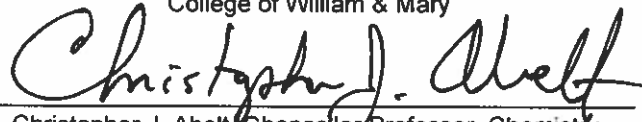


Caroline Marie Margonis

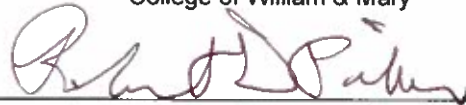
Approved by the Committee April, 2021



Committee Chair
William R. McNamara, Associate Professor, Chemistry
College of William & Mary



Christopher J. Abelt, Chancellor Professor, Chemistry
College of William & Mary



Robert D. Pike, Professor, Chemistry
College of William & Mary

ABSTRACT

Artificial Photosynthesis (AP) focuses on developing methods for the conversion of solar energy into chemical fuel in the form of H₂ and O₂. Heterogeneous photocatalytic systems incorporating carbon nanotubes (CNTs) have shown much promise but are currently limited and expensive due to their reliance on noble metals.

To that end, this work focuses on the development and synthesis of cheaper naphthalene- and pyrene-terminated iron polypyridyl complexes for use in the simultaneous functionalization of carbon surfaces, electrocatalytic proton reduction, and eventual incorporation in photocatalytic systems. Cyclic voltammetry was used to characterize the adsorption behavior of each complex on the surface of a glassy carbon electrode. For the naphthalene variant, electrode-surface adsorption saturation was reached after 720 minutes with a maximum surface coverage of 7.7×10^{-11} mol/cm², and the complex was found to be relatively surface-stable in solvents lacking hydrogen-bond donors or acceptors. Upon the addition of TFA, proton reduction catalysis occurred at -1.13 V vs. SCE in CH₃CN with an overpotential of 480 mV. Additionally, the surface-adsorbed naphthalene-functionalized complex was found to be active for hydrogen generation from purely aqueous buffer solutions of pH = 3.8 – 6.2.

A pyrene variant was synthesized through a palladium-catalyzed amination. Its maximum surface coverage on a glassy carbon electrode was found to be 3.9×10^{-11} mol/cm². The complex was found to be a weak electrocatalyst for proton reduction, with proton reduction catalysis occurring at -1.00 V vs. SCE upon the addition of TFA.

TABLE OF CONTENTS

Acknowledgements	iii
List of Tables	iv
List of Figures	v
Chapter 1. Introduction	1
The Global Energy Crisis	1
Artificial Photosynthesis Inspired by Nature	6
Development of Homogeneous AP Systems	9
From Homogeneous to Heterogeneous Systems	14
Incorporation of Carbon Surfaces into Heterogeneous Photocatalysis	16
Polyaromatic-Terminated Metal Complexes for Carbon Surface Functionalization	21
References	26
Chapter 2. Synthesis, Characterization, Carbon-Surface Functionalization, and Catalytic-Hydrogen Generation of a Naphthalene-Terminated Iron Electrocatalyst	30
Introduction	30
Experimental Procedure	33
Results and Discussion	43
Conclusion	69
References	71
Appendix A	73
Chapter 3. Preparation of a Pyrene-Terminated Iron Electrocatalyst and Future Directions	80
Introduction	80
Experimental Procedure	82

Results and Discussion	93
Conclusion	101
Future Directions	102
References	105
Appendix B	106

ACKNOWLEDGEMENTS

I would first like to first thank Professor McNamara for his support, wisdom, and guidance throughout my time at William & Mary. There have been a few points during my research project in which I felt like I was stuck and stagnant, but you always believed, offered encouragement, and challenged me to think differently and consider other perspectives. Thank you for helping me navigate all of the difficulties I faced along the way while simultaneously allowing me to build self-confidence and independence. I also want to express appreciation of the lab members in the McNamara research group for their collaboration, help, and for making lab such an enjoyable experience, despite the current situation regarding COVID. In particular, I would like to think Marissa Ho for all of her support during some tricky syntheses.

I would also like to thank Professor Abelt and Professor Pike for serving on my thesis committee. Dr. Abelt was always willing and available to assist me with whatever spectroscopy issue I encountered. As both the Director of Graduate Studies and my inorganic professor, Dr. Pike has provided much help and guidance, whether pertaining to graduate life or research. His expertise in X-ray crystallography and crystal growth has been invaluable. Most importantly, both Dr. Abelt and Dr. Pike have demonstrated immense kindness and respect throughout my time at William & Mary.

Finally, I would like to thank my family for their constant support throughout my education. At every stage of my life, my parents have always been there to offer encouragement, comfort, and love. I could not be more grateful.

LIST OF TABLES

1. Table 2.1. Preparation of Buffer Solutions	39
2. Table 2.2. Selected Bond Lengths [Å] and Angles [°] for [FeCl₂(L-Nap)]	45
3. Table 2.3. Catalytic-Wave Features in Cyclic Voltammograms of [FeCl₂(L-Nap)] upon TFA Addition	58
4. Table A.1. Crystal Data and Structure Refinement for [FeCl₂(L-Nap)]	79

LIST OF FIGURES

1. Figure 1.1. Global Direct Primary Energy Consumption	2
2. Figure 1.2. Global Atmospheric Carbon Dioxide Levels over Time	4
3. Figure 1.3. Simplified Z-Scheme of the Light Reactions in Photosynthesis	7
4. Figure 1.4. Water-Splitting Half Reactions and their Potentials	8
5. Figure 1.5. Outline of a Homogeneous AP System	9
6. Figure 1.6. Cobalt and Nickel-Based Photocatalysts	11
7. Figure 1.7. Iron Polypyridyl Photocatalysts	13
8. Figure 1.8. Energy Levels for the VB and CB of TiO ₂ and the Redox Potentials of Water	15
9. Figure 1.9. Model for SWCNT-Enhanced TiO ₂ Photocatalysis	18
10. Figure 1.10. Effect of CNT Surface Treatment and Metal in CdS/CNT/M Hydrogen Evolution Systems	20
11. Figure 1.11. Naphthalene- and Pyrene-Terminated Cobalt Complexes for Carbon Surface Functionalization	22
12. Figure 1.12. Electrochemical Behavior of the Naphthalene- and Pyrene-Terminated Cobalt Complexes	23
13. Figure 1.13. Proposed Naphthalene- and Pyrene-Terminated Iron Complexes for Carbon Surface Functionalization and Electrocatalytic Hydrogen Generation	25
14. Figure 2.1. Structure of and Models for Glassy Carbon	31
15. Figure 2.2. Structures of [FeCl₂(L)] and [FeCl₂(L-Nap)]	32
16. Figure 2.3. Complete Synthesis of [FeCl₂(L-Nap)]	34
17. Figure 2.4. Complete Synthesis of [FeCl₂(L)]	37
18. Figure 2.5. ORTEP Diagram of [FeCl₂(L-Nap)]	43
19. Figure 2.6. Scan Rate Study for [FeCl₂(L-Nap)]	46
20. Figure 2.7. Cyclic Voltammograms of [FeCl₂(L)] and [FeCl₂(L-Nap)]	47

21. Figure 2.8. Relationship between I_{cp} and Potential Sweep Rate for [FeCl₂(L-Nap)]	49
22. Figure 2.9. Variable Catalyst Electrode Adsorption Study	50
23. Figure 2.10. Time-Dependent Electrode Soak Study for [FeCl₂(L-Nap)]	51
24. Figure 2.11. Electrode Adsorption Kinetics for [FeCl₂(L-Nap)]	52
25. Figure 2.12. Impact of Solvent Soaks on [FeCl₂(L-Nap)] Adsorption Stability	53
26. Figure 2.13. Impact of Solvent on the Redox Couple of [FeCl₂(L-Nap)]	55
27. Figure 2.14. TFA Additions for [FeCl₂(L)]	57
28. Figure 2.15. TFA Additions for [FeCl₂(L-Nap)] and the Relationship between Catalytic Reduction Current and Potential Sweep Rate	58
29. Figure 2.16. Calculation of I_c/I_p for [FeCl₂(L-Nap)]	59
30. Figure 2.17. Calculation of Overpotential for [FeCl₂(L-Nap)]	60
31. Figure 2.18. Tosic Acid Additions for [FeCl₂(L-Nap)]	63
32. Figure 2.19. Acetic Acid Additions for [FeCl₂(L-Nap)]	64
33. Figure 2.20. [FeCl₂(L-Nap)] Catalytic Activity in Aqueous Buffers	66
34. Figure 2.21. Relationship between Fe(III)/Fe(II) & Proton Reduction Potentials and pH	66
35. Figure 2.22. Proposed Mechanism for Proton Reduction by [FeCl₂(L-Nap)]	69
36. Figure A.1. ¹ H NMR Spectrum of L-NO₂	73
37. Figure A.2. ¹ H NMR Spectrum of L-NH₂	74
38. Figure A.3. ¹ H NMR Spectrum of L-Nap	75
39. Figure A.4. ¹ H NMR Spectrum of L	76
40. Figure A.5. ORTEP Diagram of [FeCl₂(L-Nap)] with Naphthalenyl Disorder	76
41. Figure A.6. Scan Rate Study for [FeCl₂(L)]	77

42. Figure A.7. Acetic Acid Additions for [FeCl₂(L)]	78
43. Figure 3.1. Structures of [FeCl₂(L)] and a Proposed Pyrene-Functionalized Complex	81
44. Figure 3.2. Synthesis of L-NH₂	82
45. Figure 3.3. Synthesis of L-Py1	84
46. Figure 3.4. Synthesis of L-Py2a and L-Py2b	86
47. Figure 3.5. Synthesis of FeCl₂(L-Py2b)	87
48. Figure 3.6. Synthesis of L-Py3	88
49. Figure 3.7. Synthesis of FeCl₂(L-Py3)	90
50. Figure 3.8. Proposed Structures for a Pyrene-Functionalized Polypyridyl Ligand	93
51. Figure 3.9. Simplified Mechanism for the Buchwald-Hartwig Amination	96
52. Figure 3.10. Cyclic Voltammograms of [FeCl₂(L-Nap)] and [FeCl₂(L-Py3)]	98
53. Figure 3.11. Scan Rate Study and Relationship between <i>I</i> _{cp} and Potential Sweep Rate for [FeCl₂(L-Py3)]	99
54. Figure 3.12. TFA Additions for [FeCl₂(L-Py3)]	100
55. Figure 3.13. Tosic Acid Additions for [FeCl₂(L-Py3)]	101
56. Figure 3.14. Alternative Synthesis for a Pyrene-Functionalized Polypyridyl Ligand	103
57. Figure 3.15. Proposed Heterogeneous AP System Incorporating FeCl₂(L-Nap) as the Catalyst	104
58. Figure B.1. ¹ H NMR Spectrum of L-NO₂	106
59. Figure B.2. ¹ H NMR Spectrum of L-NH₂	107
60. Figure B.3. ¹ H NMR Spectrum of L-Py2b	108
61. Figure B.4. ¹³ C NMR Spectrum of L-Py2b	109
62. Figure B.5. ¹ H NMR Spectrum of L-Py3	110

Chapter 1. Introduction

The Global Energy Crisis

As a result of rapid population growth and global industrialization, energy consumption and demands have spiked over the past few decades. From 1950 to 2019, global direct primary energy usage has more than quintupled, increasing from 28,000 to 159,000 TWh.¹ Furthermore, energy consumption is expected to see a 2-fold increase by the year of 2050 based on trends and data collected in the mid-2000's.² Much of this energy-demand increase can be attributed to the continuing population growth and economic development of India, China, and several South American countries, all of which are nonmembers of the Organization for Economic Cooperation and Development (OECD). In contrast to OECD countries, which are projected to have consistent energy demands relative to population growth, nonmembers' energy consumption is expected to grow by 2.2% per year, heightening their usage of total worldwide energy from 54% in 2010 to 65% by 2040.³ The strain placed on energy demands by non-OECD members stems from their current lack of stable energy-distribution systems and the economic renovations they would have to undergo in order to advance.⁴

Since the Industrial Revolution, nonrenewable energy sources, such as coal, petroleum, and natural gas, have dominated the energy market and are currently the most utilized energy sources; combined, these nonrenewables make up 85% of the global direct primary energy consumption (Figure 1.1).⁵ In

order to examine the lifetime of these energy sources, it is important to make the distinction between resources and reserves. The former, which accounts for the majority of global-fossil fuels, are unable to be safely and cost-effectively extracted and brought to market with available technologies. On the other hand, reserves make up the small fraction of fossil fuels that are economically harvestable. Based on currently-recognized reserves and production levels in 2015, the world has about 115 years of coal production and 50 years each of oil and natural gas remaining.⁶

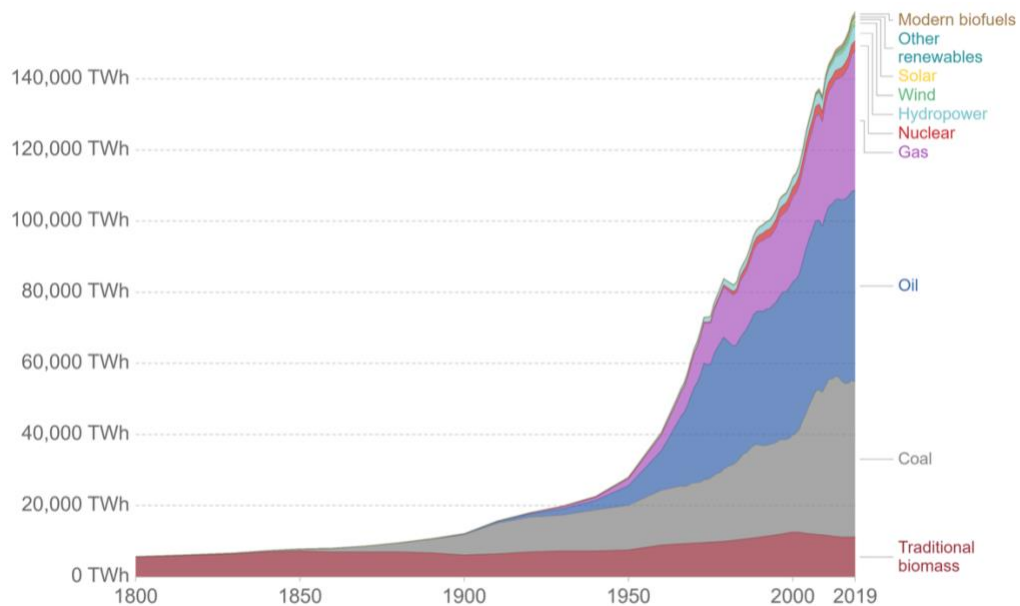


Figure 1.1. Global direct primary energy consumption.¹

Though innovative technologies will likely allow for the conversion of some resources into reserves in the future, continued reliance on fossil fuels still carries a plethora of problems. One issue arises from the danger associated with the extraction of these resources themselves. Notably, on April 20, 2010, the Deepwater Horizon drilling rig located in the Gulf of Mexico exploded and

subsequently caught fire, causing the death of 11 workers. Over the next several days, crude oil leaked from the rig, generating a total discharge of over 780,000 m³, resulting in extensive, long-term damage to marine and wildlife habitats and the immediate death to animals living within.⁷

In addition to risks associated with harvesting these resources, the combustion of fossil fuels expels toxic byproducts into the environment. Released from the combustion of fossil fuels, sulfur dioxide and nitrogen oxides react with atmospheric water, oxygen, and various pollutants to form sulfuric and nitric acids, leading to acidic rain, lakes, and streams.⁸ Furthermore, these particles can result in nutrient depletion of the soil, nutrient imbalances in river basins, and expedited crop decomposition.⁸ Other particulate matter released into the atmosphere contributes to smog and is linked to a variety of human-health conditions, such as respiratory illnesses and cardiovascular diseases.⁹

Another combustion byproduct posing a threat to the health of Earth's environment and wildlife is carbon dioxide. As a greenhouse gas, atmospheric carbon dioxide is capable of absorbing and radiating heat. For millions of years, Earth's lands and oceans have continuously radiated thermal infrared energy, which has been absorbed by greenhouse gases and gradually reradiated back to Earth's surface. This natural cycle is responsible for maintaining the climate and temperatures humans and other species have been accustomed to for thousands of years.¹⁰ However, due to the relatively modern reliance on the combustion of fossil fuels, atmospheric carbon dioxide levels have increased from approximately 315 ppm to over 409 ppm since 1960.¹¹ These elevated levels,

which far exceed those measured in the natural atmospheric carbon dioxide cycle over the past 800,000 years, have resulted in excessive reradiation of heat back to Earth (Figure 1.2).

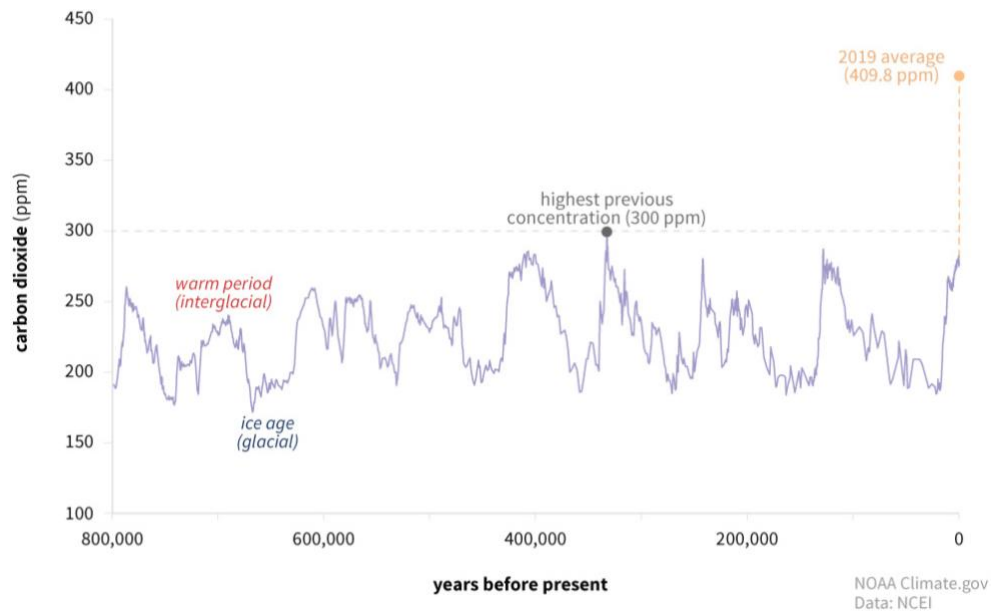


Figure 1.2. Global atmospheric carbon dioxide concentrations, derived from ice core data, during the past 800,000 years.¹⁰

Consequently, the global-surface temperature over the past 100 years has risen by about 0.8 °C, and 16 of the 17 warmest years recorded have occurred since 2001.¹⁰ In addition to a rise in our planet's temperature, climate change brings an increase in extreme weather. The intensity of hurricanes is predicted to increase due to a larger temperature difference between the warm, tropical ocean and the cold, upper atmosphere.¹² Lightning strikes are predicted to see a 50% increase, and floods, droughts, and wildfires are becoming more dangerous and less manageable.¹² Permafrost has decreased by 10% since the early 1900's, and sea ice is melting, which has lowered the amount of heat reflected

back into the atmosphere and has, in turn, perpetuated further temperature increases and ice melt. If greenhouse gas emissions are not addressed, global sea levels could rise by as much as 0.9 meters by 2100 as a result of melting polar ice.¹³ Furthermore, carbon dioxide absorption by the ocean and the subsequent formation of carbonic acid has resulted in a 30% increase in ocean-water acidity since the Industrial Revolution. This has led to the erosion of coral reefs and a decrease in the availability of carbonate, a key component of aquatic shells and skeletons.¹⁴

However, it is important to note that these former models for energy demand, usage, and environmental impact did not account for one major recent event: the COVID-19 pandemic. In addition to disrupting the lifestyle of the human population, the pandemic caused a huge disturbance in the energy sector; with a sharp transition from a heavy global reliance on travel to worldwide stay-at-home orders and social distancing, coupled with less funding available for larger economic projects and expansions, global energy demand dropped by 5% and energy investment by 17% in 2020.¹⁵ Investments in coal, oil, gas, and nuclear fuels all experienced a 8.5% decrease, yet renewable-energy investments rose by 0.9%. While it is still too soon to gauge the long-term effects of the pandemic on the energy sector, it is clear that, with the finite supply, countless risks, and detrimental effects stemming from the use of fossil fuels as our primary energy source, development of methods to reliably harvest and process renewable sources is vital to long-term global health.

Evidenced by an increase in renewable energy funding despite COVID-19 budget cuts, there has been significant focus on the development of cleaner energy sources over the past couple decades. Though nonrenewable carbon sources dominate the energy sector, renewable energy sources, such as wind, solar, biomass, and hydropower, contributed 11% to global energy consumption in 2018.¹⁶ Furthermore, renewable energy is the fastest growing sector, showing a 100% increase from 2000 to 2018 in the United States.¹⁷ Of renewable energy sources, solar energy is predicted to see the largest growth due to its widespread abundance and potential for harvestable energy; with over 100,000 TW of solar energy reaching Earth's surface yearly, the sun provides enough energy per hour to meet human-energy demands for an entire year.¹⁸ As such, development of technologies capable of capturing, storing, and distributing solar energy are essential to transform sunlight into a more reliable and marketable energy source.

Artificial Photosynthesis Inspired by Nature

As seen in natural photosynthesis, one potential approach is to store solar energy in the form of chemical bonds. In photosynthesis, solar energy is used to convert carbon dioxide and water into chemical energy in the form of sugars with oxygen released as a byproduct. Photosynthesis can be broken down into two related photosystems: Photosystem I (PSI) and Photosystem II (PSII). Photosynthesis begins upon solar irradiation of PSI, resulting in its excitation and the initiation of an electron transfer process. Electrons are passed from PSI,

resulting in its oxidation, and are ultimately used to reduce NADP^+ (nicotinamide adenine dinucleotide phosphate) to NADPH. By acting as both a proton and electron source, this reduced molecule subsequently takes part in the Calvin Cycle, in which carbon dioxide is converted to carbohydrates. Electron transfer from PSII to the oxidized PSI returns this photosystem to its original state. Subsequently, the oxidized PSII drives the water splitting reaction, catalyzed by a CaMn_4O_x cluster, to produce oxygen gas (Figure 1.3).¹⁸

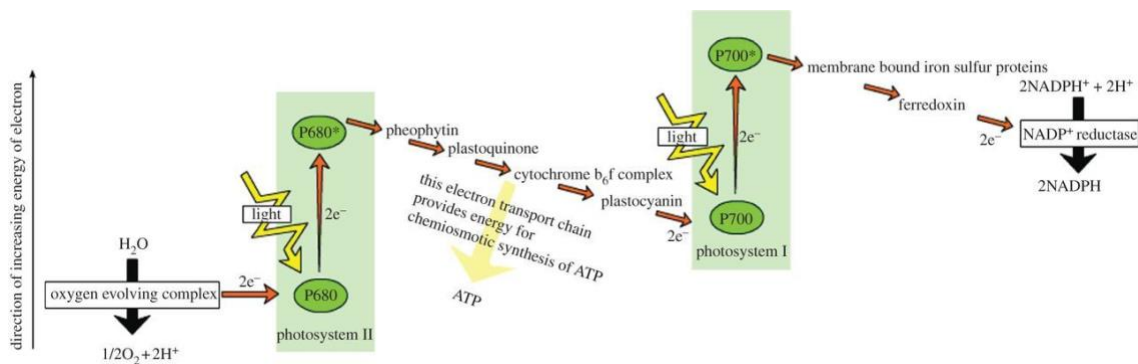


Figure 1.3. Simplified Z-scheme of the light reactions in photosynthesis.¹⁸

Inspired by natural photosynthesis, Artificial Photosynthesis (AP) systems aim to convert solar energy to chemical energy by splitting water into molecular oxygen and hydrogen. The water-splitting redox process can be divided into two half reactions: the reduction of water to H_2 and the oxidation of water to O_2 (Figure 1.4).¹⁹ The generated hydrogen can either be cleanly burned for energy harvest, leaving water as a byproduct, or combined with oxygen in a fuel cell to produce electricity.¹⁸

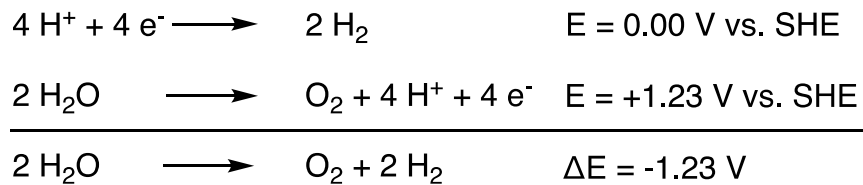


Figure 1.4. Water-splitting redox half reactions with potentials given at pH 7 vs. SHE.¹⁹

Though a complete AP system would involve the combination of both, the redox half reactions are typically studied and optimized individually. Focusing on the reductive side of this process, a popular method for hydrogen generation involves combining an active electrocatalyst with a chromophore and a sacrificial source of electrons. For such a system to be successful, the excited state of the chromophore must be capable of electron transfer at or past the catalyst's working potential, and the catalyst must be capable of accumulating charge during the process. Furthermore, long-term operation relies on the stability of each component throughout irradiation.²⁰ With these conditions met, upon absorption of light, the chromophore enters an excited state, from which it can be reduced by the sacrificial electron donor. The electron from the reduced chromophore can then be transferred to the catalyst, which uses the electrons to reduce protons in the solution to hydrogen gas. Ideally, since the catalyst is regenerated in this process, hydrogen gas production is sustained until consumption of the sacrificial electron source or decomposition of the chromophore (Figure 1.5).

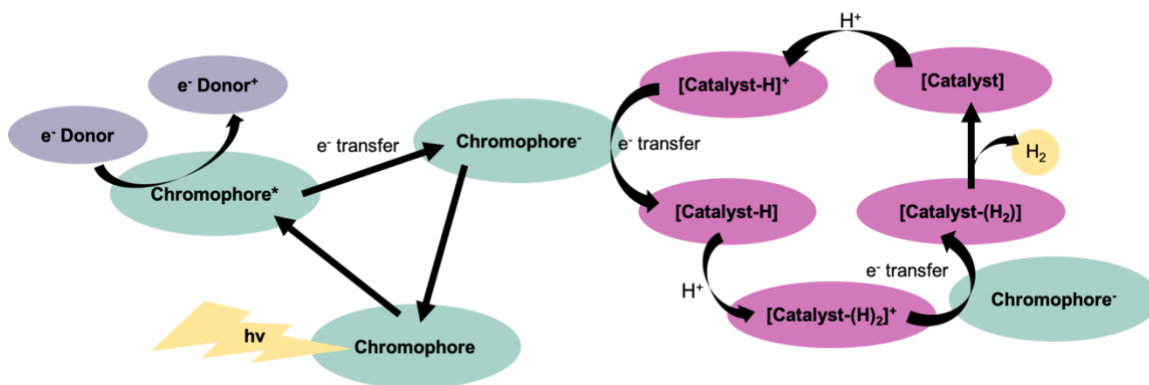


Figure 1.5. Simplified outline of a photocatalytic system for hydrogen generation highlighting a reductive-quenching pathway.

Development of Homogenous AP Systems

When designing a catalyst for incorporation into an AP system, there are several criteria that must be met: the complex must be active, efficient, stable, and economically viable. Catalytic activity is measured by its turnover frequency (TOF), which refers to the number of catalytic cycles occurring at the center per unit of time. Catalytic efficiency is related to its overpotential, which is the potential difference between a half-reaction's thermodynamically determined reduction potential and the potential at which the redox event is experimentally observed.²¹ With a lower overpotential, less energy is wasted in the driving of the catalytic cycle. Catalytic stability is directly related to its turnover number (TON), which is the ratio of the moles of product produced per mole of catalyst. Furthermore, an AP ideal catalyst requires stability in the presence of both water and oxygen to allow for a longer shelf-life and incorporation into aqueous AP systems. Economic viability accounts for the cost of materials, which is a major factor dictating catalyst design and widespread availability. While noble-metal catalysts, such as platinum or iridium complexes, are excellent hydrogen

producers due to their ability to form hydride bonds, their high cost and limited availability restrains their wide-scale use.²² To allow for universal operation, AP systems that incorporate catalysts containing cheap, Earth-abundant transition metals (Co, Fe, Ni) are essential.

Inspired by Ni and Fe hydrogenases found in nature, cobalt complexes acting as artificial hydrogenases for the photocatalytic generation of H₂ have become attractive. One of the first cobalt-based AP systems reported in 1981 utilized [Co(bpy)_n]²⁺ as the catalyst, [Ru(bpy)₃]²⁺ as the chromophore, and ascorbic acid as the sacrificial electron donor. Upon light irradiation at 420 nm, a quantum yield of 13% was achieved for H₂ generation at the optimal pH of 5.0, which may have assisted the formation of a cobalt-hydride intermediate.²³ Since then, cobalt-based systems have seen immense improvement. Reported in 2009 by Eisenberg et al., a series of cobaloxime complexes, paired with a Pt terpyridyl acetylide chromophore and triethanolamine as the sacrificial donor, were found to be active for hydrogen evolution in aqueous mixtures of acetonitrile (Figure 1.6, a). The most active of such complexes achieved ~2150 TONs of H₂ after only 10 hours of photolysis.²⁴ However, reliance on a platinum-based chromophore and a 24:1 acetonitrile:water reaction mixture adds a high cost to this system and limits widespread usage. In later years, expanded photocatalytic activity was achieved through the use of a cobalt-dithiolene complex paired with [Ru(bpy)₃]²⁺, a less expensive photosensitizer (Figure 1.6, b). This system, which successfully operated in 1:1 acetonitrile:water solution, reached turnovers up to 9,000 with respect to catalyst and had an initial TOF of up to 3450 h⁻¹. Enhanced

hydrogen generation was achieved by incorporating more electron-withdrawing substituents, leading to a more positive reduction potential for $\text{CoL}_2^-/\text{CoL}_2^{2-}$. However, decomposition of the catalyst and chromophore lead to a plateau in hydrogen evolution after 6 – 10 h.²⁵

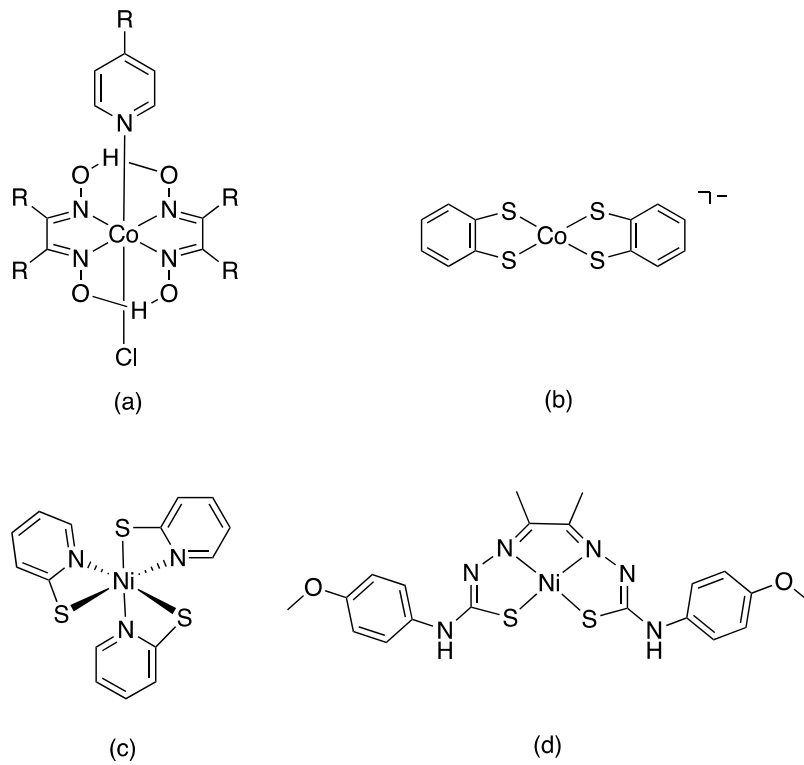


Figure 1.6. Examples of cobalt and nickel-based photocatalysts.²⁴⁻²⁷

Like cobalt, nickel incorporation in AP catalyst design is promising due to its relatively low cost and function in natural hydrogenases. In 2012, Eisenberg et al. reported a pyridine thiolate nickel complex that mimicked the [Fe-Ni]-hydrogenase active site. In their system, fluorescein and Eosin Y were utilized as the photosensitizer and triethylamine as the sacrificial donor (Figure 1.6, c). When combined with fluorescein and triethylamine in 1:1 ethanol:water, this

noble-metal-free catalytic system was found to be highly active for hydrogen generation, achieving 5500 TONs after 40 hours of irradiation.²⁶ An initial TOF of 250 moles of H₂ per mole catalyst per hour was observed, but the lifetime of this system was limited by the coupled decomposition of the catalyst and fluorescein.

Another recently emerging class of nickel complexes are thiosemicarbazone electrocatalysts. The presence of S-donors and N-atoms within the ligand framework of these complexes allows for protonation and proton relays to occur, making them promising candidates for catalytic hydrogen generation. In 2019, Orio et al. reported such a system incorporating a bis-thiosemicarbazone nickel (II) complex (NiTSC-OMe) paired with triethylamine as the electron donor (Figure 1.6, d). In addition to studying the effect of catalyst concentration, the pH of the buffer solution, and the effect of the solvent ratio on the photocatalytic system, [Ir(ppy)₂(bpy)]PF₆, [Ru(bpy)₃]Cl₂, and [ZnTMePy]PCl₄ (TMePy = 2,4,6-trimethylpyridine) were each tested respectively as photosensitizers. The optimized system, which incorporated NiTSC-OMe (5*10⁻⁸ M), [Ir(ppy)₂(bpy)]PF₆ (ppy = 2-phenylpyridine) (5*10⁻⁴ M), TEA (5% (v/v)) at pH 10 in 4:1 CH₃CN/H₂O solution, reached TON and TOF values greater than 11,300 and 7,900 h⁻¹ respectively. Though high catalytic activity was achieved using the iridium-based photosensor, no hydrogen evolution was observed using the noble-metal free [Ru(bpy)₃]Cl₂ and [ZnTMePy]PCl₄ variants.²⁷

Though there are many examples of active cobalt and nickel complexes, there are far fewer examples of iron catalysts for hydrogen generation in aqueous solutions. As the most Earth-abundant metal, iron is widely accessible

and relatively low in cost, which makes its incorporation into large-scale AP systems more economically feasible. Much work involving synthesis of iron catalysis has focused on mimicking the active site of natural hydrogenases. Though such catalysts have been found to be electrocatalytically active, hydrogen generation is far less than [Fe]H₂ase, and activity is limited to nonaqueous media. Overcoming these concerns, the McNamara research group has recently reported several iron polypyridyl catalysts that are active in aqueous media (Figure 1.7).²⁸

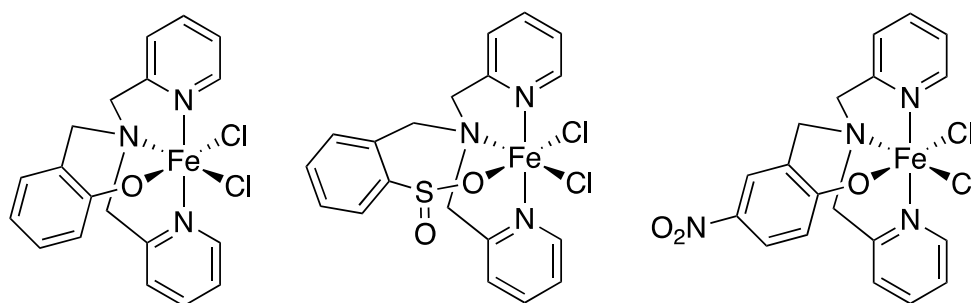


Figure 1.7. Iron polypyridyl complexes.²⁸

Each complex was found to be highly active and could function as a stable electrocatalyst for proton reduction upon the addition of trifluoroacetic acid (TFA) in acetonitrile solutions. Furthermore, incorporation of water enhanced the electrocatalytic activity. When assessed for photocatalytic activity, the unfunctionalized complex was found to be the most active, followed by the nitro- and sulfinato- complexes respectively. Upon irradiation with green light-emitting diodes, this complex achieved TONs greater than 2100 after 24 hours when paired with fluorescein (1.9 mM) and triethylamine (5% (v/v)) in a 1:1

ethanol:water mixture. This catalyst was also found to be active in aqueous mixtures containing local lake water, which holds promise for the incorporation of such a system into less industrialized areas of the world.²⁸

From Homogeneous to Heterogeneous Systems

A major barrier limiting the catalytic activity of homogeneous systems is diffusion; in order for electrons to be relayed from the sacrificial donor to the chromophore followed by the catalyst, these molecules must be in close proximity to one another. Heterogeneous systems aim to overcome these issues and expedite the electron-transfer process by anchoring the chromophore and catalyst to a wide band gap semiconductor, such as TiO_2 or SrTiO_3 , to develop a linked system. In these metal oxide semiconductors, an electron-hole pair is generated when a photon having energy greater or equal to the band gap energy of the semiconductor is absorbed, resulting in the promotion of an electron to the conduction band (CB) and leaving a hole in the valence band (VB). Since the band gap of semiconductors is void of energy levels, the lifetime of electron-hole pair is sufficient enough to allow for their migration to the surface of the semiconductor without recombination. These electrons and holes have the respective potential to reduce or oxidize adsorbed reactants on the semiconductor.²⁹

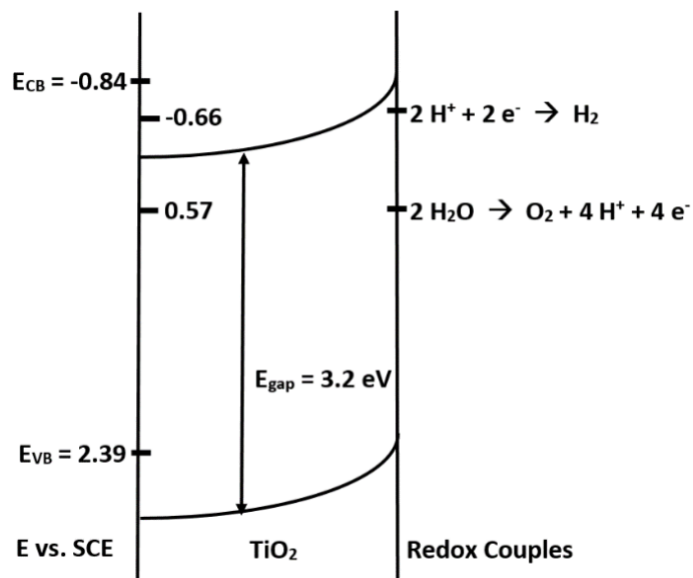


Figure 1.8. Energy levels for the VB and CB of TiO₂ and the redox potentials of water at pH = 7. Band bending across the x-axis reflects local changes in electronic structure due to space-charge effects and charge-neutrality imbalances.³⁰

Charge transfer from semiconductor to reactant is dependent on the semiconductor's conduction and valence band positions in respect to the redox potential of the reactant. For incorporation in an AP system, the conduction band must be more negative than the proton reduction potential, and the valence band must be more positive than the water oxidation potential. As such, wide band gap semiconductors, such as TiO₂ (band gap >3 eV), are of interest due to their capability to fulfill these criteria (Figure 1.8).³⁰

Though encompassing both proton reduction and water oxidation potentials, the wide band gap energy of TiO₂ comes with the caveat that its photocatalytic activity is limited to light with wavelengths below 385 nm, which is only about 4% of what solar energy provides. Furthermore, when photocatalytic TiO₂-mediated water-splitting was first put into practice, the system suffered from

fast photo-generated electron-hole pair recombination before participation in the redox reaction. Additionally, the system operated with a high overpotential for H₂ and O₂ evolution.³¹ As such, much work has gone into surface modification of TiO₂ and development of other semiconductors.

Incorporation of Carbon Surfaces into Heterogeneous Photocatalysis

Mechanically robust and thermochemically stable, carbon nanotubes (CNTs) have received recent attention for use in the alteration of semiconductor surfaces. Depending on the type used, CNTs can exhibit electrical conductivity, act as semiconductors, demonstrate high tensile strength, or provide thermal conductivity.³² CNTs can be broken into two broad categories: single-walled carbon nanotubes (SWCNTs) and multi-walled carbon nanotubes (MWCNTs). Structurally, SWCNTs can be visualized as rolled-up sheets of graphene (sheet of sp² hybridized carbons), and these nanoparticles typically possess semiconducting or metallic prosperities depending on their chiral angle. MWCNTs consist of many SWCNTs bound together by Van der Waals interactions and tend to display conducting or metallic behavior. In applications to photocatalytic activity, the primary role of CNTs is likely to be the CB electron acceptor since the work function of CNTs (4.8 eV for SWCNTs and 4.3 – 5.1 eV for MWCNTs) is larger than the CB energy levels of TiO₂ (4.21 eV). This indicates that charge transfer from TiO₂ to CNTs is favorable in both cases.³³

To study the difference in photocatalytic activity between unaltered TiO₂ samples and composite CNT/TiO₂ samples, Yao and coworkers monitored

electron-hole pair recombination occurrence based on photoluminescence behavior.³⁴ When electron-hole pair recombination occurs after irradiation, photons are emitted, resulting in detectable photoluminescence. As the measured photoluminescence intensity increases, so does the amount of electron-hole pair recombination, which limits participation in redox chemistry.

In comparison to unaltered TiO₂ samples, composite CNT/TiO₂ samples showed diminished photoluminescence, indicating reduced charge recombination. Photoluminescence reduction was found to be greater in the SWCNT/TiO₂ composites than the MWCNT/TiO₂ composites due to better attachment of the SWCNTs to TiO₂. To explain decreased charge-recombination capacities of the composite samples compared to unaltered TiO₂, it is important to consider the placement of the CB and VB in each sample. Upon UV illumination, electrons are excited from the TiO₂ VB to its CB. Without CNT modification, most of these charges in TiO₂ quickly recombine, preventing involvement in redox chemistry and photocatalysis. Conversely, since the CB of SWCNTs lies slightly below that of TiO₂, electrons in the composite sample are able to transfer from the TiO₂ CB to that of the attached SWCNTs, providing charge separation, stabilization, and hindered recombination (Figure 1.9). The longer lived charges in the composite sample allow for higher catalytic activity.³⁴

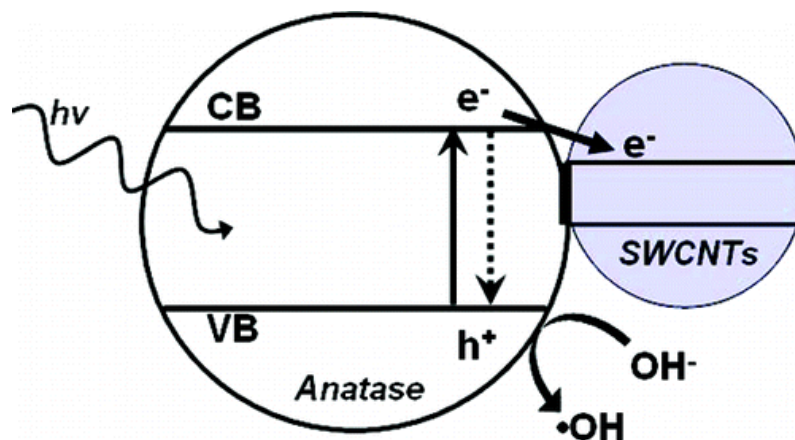


Figure 1.9. Proposed model for SWCNT-enhanced TiO₂ photocatalysis.³⁴

Applying these findings to photocatalysis in 2009, Wei and coworkers reported a system using a MWCNT/TiO₂ nanocomposite for visible-light hydrogen generation.³⁵ The MWCNT/TiO₂ nanocomposites, which were joined hydrothermally by the direct growth of TiO₂ on the MWCNT surfaces, were loaded with Pt by stirring with H₂PtCl₆ under an Hg-lamp. Compared to pristine TiO₂, the composite nanoparticles exhibited amplified adsorption of visible light, which could be attributed to the enhancement of the surface-electric charge of the oxides. This arises from the possible electronic transition of $\pi \rightarrow \pi^*$ of MWCNTs and $n \rightarrow \pi^*$ between the n-orbital of the oxygen species of TiO₂ and MWCNTs. Under visible light irradiation with a Pt loading of 1 wt% and 15 vol% triethanolamine as the sacrificial donor, the MWCNT/TiO₂ nanocomposites peaked at 960 $\mu\text{mol H}_2 \text{g}^{-1}$, and photocatalytic activity was relatively steady throughout a 5 hour irradiation period, though a slight drop was observed after 3 h. This decline was attributed to consumption of the electron donor, for the system's photolytic activity could be recovered with the addition of more triethanolamine.³⁵

Mechanistically, the group proposed that electrons in the MWCNTs, which act as the photosensitizer, move from the VB to the CB upon photoexcitation, leaving behind a hole in the VB. These electrons are transferred from the CB of the MWCNTs to that of the chemically-attached TiO₂. Then, the loaded Pt nanoparticles use these electrons to catalyze proton reduction. Throughout this process, triethanolamine is oxidized by donating an electron to the holes in the MWCNTs to regenerate and restore the catalytic cycle.³⁵ However, it is important to note that this proposed mechanism, assuming MWCNTs function as the photosensitizer, may be incorrect, as the energy required to remove an electron from the MWCNTs is higher than the TiO₂ band gap.³⁴ Though this system demonstrated hydrogen generation using visible light, a 32-fold increase in activity was observed with irradiation under the full spectra, which is a poor mimic of natural sunlight. Additionally, the system's reliance on Pt limits its expansive economic use.

Photocatalytic enhancement of semiconductors by CNTs is not just limited to TiO₂ but has also been applied to chalcogenide semiconductors, like CdS, due to their higher visible-light adsorption arising from a lower band gap of 2.4 eV. The CB energy level of CdS is around 3.49 eV, which, like TiO₂, indicates favorable charge transfer from CdS to CNTs since the work function of CNTs is larger. Additionally, emission of CdS was found to be completely quenched when bound to SWCNTs, suggesting electron transfer from CdS to the CNT.³⁶ In 2010, a photocatalytic system taking advantage of these properties was reported by Kim and coworkers, who examined both the effect of different CNT treatments

and different loaded metals on hydrogen generation.³³ First, crude CNT powders (c-CNT) were treated with either heat (h-CNT) or acid (a-CNT) in order to enhance the purity of each sample. While these treatments did not alter the surface morphologies of c-CNT, both heat and acid treatment resulted in carboxylic acid functionalization due to oxidation. Each of these CNT samples was then loaded with a metal (Pt, Ru, Cu, Ni, Ag, and Au) via sequential chemical adsorption and reduction and were subsequently immobilized on CdS to create CdS/CNT/M hybrids. An aqueous suspension of the nanoparticle hybrids (1 g/L) and the electron donors, Na₂S or Na₂SO₃ (0.1 M), was irradiated with visible and infrared radiation ($\lambda > 400$ nm) using a 300 W halogen lamp, and hydrogen production was measured using gas chromatography.

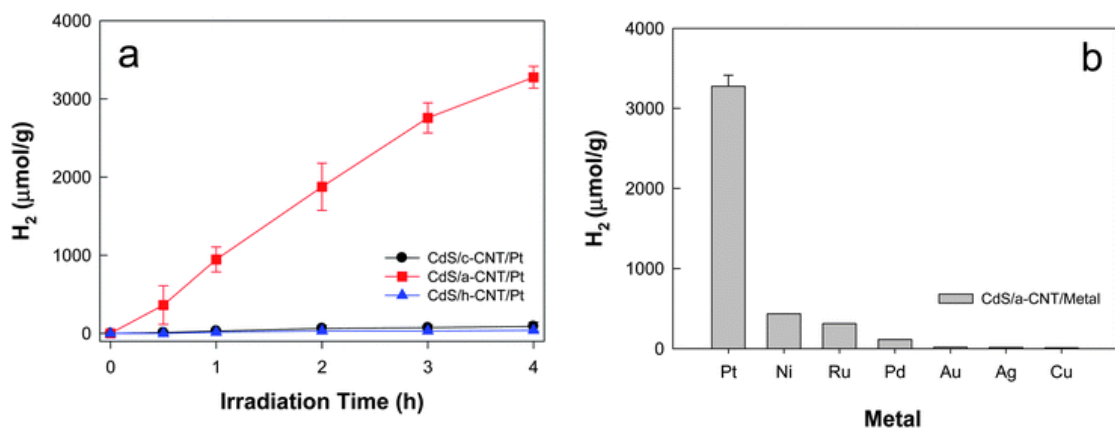


Figure 1.10. (a) Effect of surface treatment and (b) effect of metal on hydrogen production for the CdS/CNT/M systems.³³

As the most active of the metal-nanoparticle hybrids, the CdS/a-CNT/Pt system produced about 3.3 mmol g⁻¹ of hydrogen, which was 8 times greater than that of the unloaded CdS/CNT particles, in a 4-hour time period. Ni, Ru, and

Pd showed moderate hydrogen production whereas Au, Ag, and Cu had little activity. In terms of the effect of surface treatment on catalytic activity, a-CNT severely outperformed both h-CNT and c-CNT (Figure 1.10). This large difference could arise from a higher metal percentage in the a-CNT hybrid compared to the others, as inductively coupled plasma mass spectrometry indicated that metal contents for the Pt hybrid were 0.12, 0.14, and 1.24 wt% in the c-CNT, h-CNT, and a-CNT hybrids respectively.³³ Though the optimized photocatalytic system was effective, its reliance on Pt makes it costly. Additionally, hydrogen production was extremely sensitive to surface treatment; failure to properly treat CNTs with acid before use can nullify any expected catalytic activity.

Polyaromatic-Terminated Metal Complexes for Carbon Surface

Functionalization

Though incorporation of CNTs into photocatalytic systems due to its ability to function as an electron acceptor, transporter, and suppressor of electron-hole pair recombination shows much promise, it is clear that work is needed on the development of cheaper metal catalysts. Instead of directly loading a metal, an alternative approach is to design a catalyst that is able to covalently adsorb to CNT surfaces through π - π stacking interactions, which arise from attraction of positive electrostatic potential of one aromatic surface to negative electrostatic potential of another. As a non-covalent interaction, these forces are typically much weaker than covalent bonds, but the magnitude of attraction can be

modified by altering the size of the pi-stacking network; calculations on the strengths of π - π -stacking interactions between aromatic molecules and CNTs suggest that binding energies are in the range of 10-25 kJ/mol per benzene ring, signifying that the strength of the system increases with the size of the polyaromatic network. Furthermore, adsorption of two π - π stacking molecules is reversible, meaning that the electronic properties of each is kept intact.³⁷

In 2009, Goldsmith et al. reported naphthalene and pyrene terminated cobalt complexes ($[\text{Co}(\text{tpy}\sim\text{nap})_2]^{2+}$ and $[\text{Co}(\text{tpy}\sim\text{py})_2]^{2+}$ respectively) for the functionalization of carbon surfaces via pi-stacking interactions (Figure 1.11).³⁸ Electrochemical techniques were used to investigate the behavior and adsorption processes of these polyaromatic complexes onto a glassy carbon electrode. Though not as large or pristine as the graphene surfaces present in CNTs, the surface of glassy carbon electrodes contain smaller domains of graphene-like areas and make it a convenient proxy.

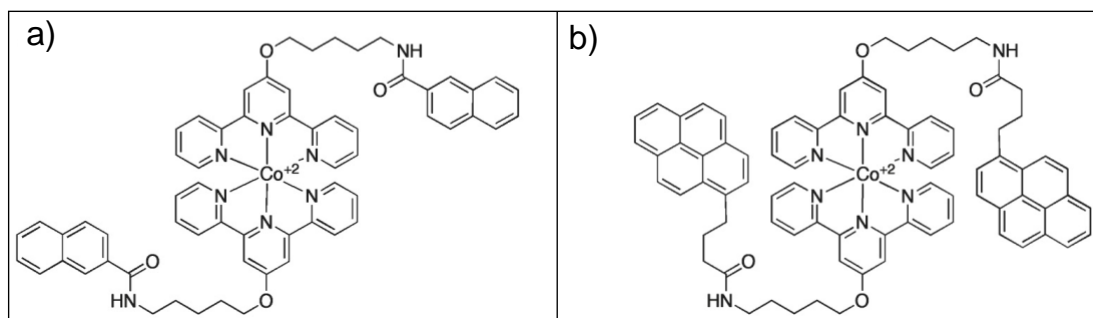


Figure 1.11. a) Naphthalene and b) pyrene terminated cobalt complexes for the functionalization of carbon surfaces.³⁸

In their study, a glassy carbon electrode was soaked overnight in a 0.5 mM solution of either $[\text{Co}(\text{tpy}\sim\text{nap})_2]^{2+}$, $[\text{Co}(\text{tpy}\sim\text{py})_2]^{2+}$, or $[\text{Co}(\text{tpy})_2]^{2+}$, the base

complex without aromatic functionalization. The electrode was removed, rinsed with acetonitrile, and added to an electrochemical cell containing pure 0.1 M TBAH/CH₃CN. The potential of the working electrode was cycled between -0.45 and +0.15 V vs. Fc/Fc⁺ to focus on the Co(II/III) redox process. Since no redox-active material was added to the solution, any electrochemical response observed must arise from material adsorbed to the electrode surface. Without aromatic functionalization, no redox couple was observed for the [Co(tpy)₂]²⁺-soaked electrode. However, the redox couples present in cyclic voltammograms of [Co(tpy~nap)₂]²⁺ and [Co(tpy~py)₂]²⁺ indicate successful adsorption to the electrode surface (Figure 1.12).³⁸ Additionally, the peak current increased linearly with the potential sweep rate, and the separation between the cathodic and anodic wave peaks was less than 58 mV, both of which are characteristic of electroactive material adsorbed to the working electrode.

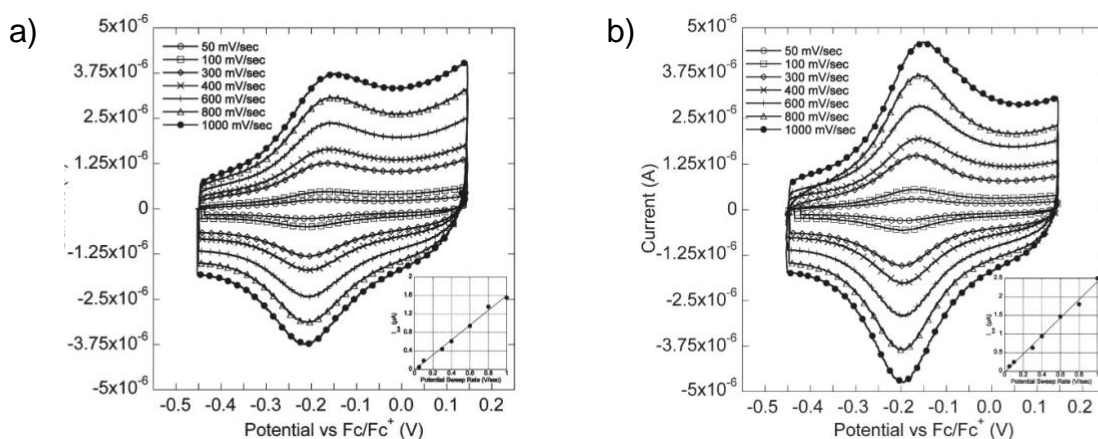


Figure 1.12. Cyclic voltammograms of a) [Co(tpy~nap)₂]²⁺ and b) [Co(tpy~py)₂]²⁺ adsorbed to the surface of a glassy carbon electrode.³⁸

Though both polyaromatic functionalized complexes were able to adsorb to the electrode surface, $[\text{Co}(\text{tpy}\sim\text{py})_2]^{2+}$ demonstrated a greater strength of attraction; the peak current for the pyrene complex was larger and only diminished by 25% after 2 hours of continuous cycling. In contrast, the naphthalene complex suffered from rapid desorption from the electrode surface. To quantify these observations, the Langmuir Isotherm model was used to calculate the free energy of adsorption, which was found to be -41 kJ/mol for $[\text{Co}(\text{tpy}\sim\text{py})_2]^{2+}$ and -30 kJ/mol for $[\text{Co}(\text{tpy}\sim\text{nap})_2]^{2+}$.³⁸ These differences can be rationalized by considering the pi-networks of each molecule; since naphthalene has a smaller delocalized π system, adsorption via π - π stacking is less favorable when compared to pyrene's larger network. Though a weaker adsorbant, $[\text{Co}(\text{tpy}\sim\text{nap})_2]^{2+}$ demonstrated greater surface-area coverage due to the smaller size of its polyaromatic ring. The cyclic voltammetry data and thermodynamic calculations from this study indicate that complexes with polyaromatic components can be successfully used in the functionalization of sp^2 -hybridized carbon surfaces via pi-stacking interactions.

Using the framework that has been successful for the electro and photocatalytic generation of hydrogen in the McNamara groups' homogeneous systems, the work presented in this thesis aims to synthesize naphthalene- and pyrene-functionalized iron polypyridyl complexes (Figure 1.13). The adsorption behavior of these complexes on a glassy carbon electrode will first be tested using cyclic voltammetry followed by their ability to act as electrocatalysts for proton reduction in both organic and aqueous media. Once electrocatalytic

behavior has been confirmed, photocatalytic proton reduction and applications to such systems could be examined. Through the incorporation of an iron-based complex instead of reliance on noble metals, this heterogeneous catalytic system circumvents the issue of high cost associated with previously reported CNT-based systems.

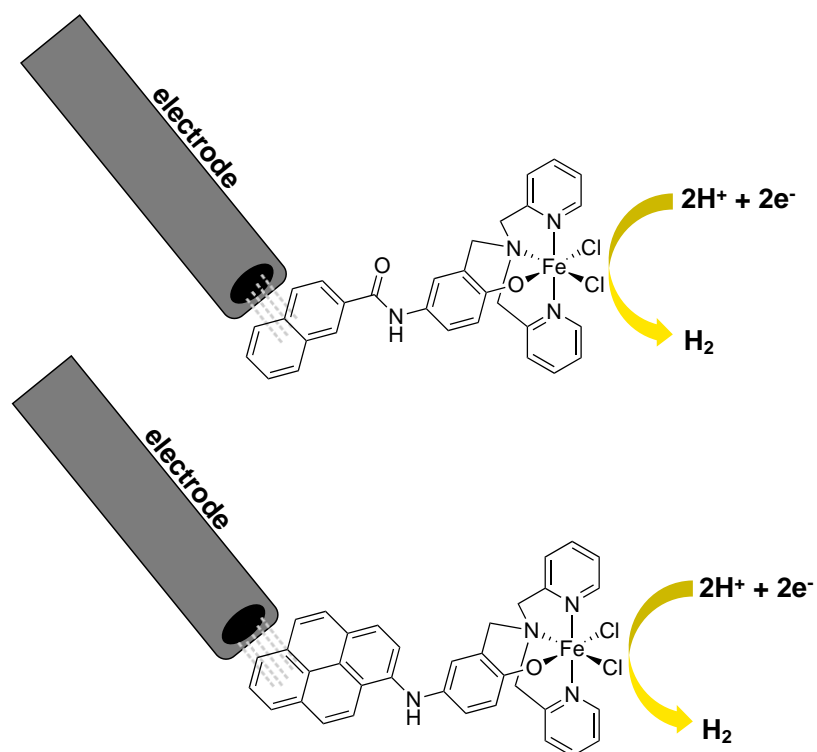


Figure 1.13. Proposed naphthalene- and pyrene-terminated iron complexes for the functionalization of carbon surfaces.

References

1. "Global direct primary energy consumption". Our World in Data. **2020**. <https://ourworldindata.org/grapher/global-primary-energy> (accessed December 12, 2020).
2. Lewis, N. S.; Nocera, D. G. Powering the planet: chemical challenges in solar energy utilization. *Proc. Natl. Acad. Sci.* **2006**, 103, 15729-15735.
3. "Future world energy demand driven by trends in developing countries". U.S. Energy Information Administration. **2013**. <https://www.eia.gov/todayinenergy/detail.cfm?id=14011> (accessed February 13, 2021).
4. Capuano, L. International Energy Outlook. EIA. **2020**, 2-7.
5. Statistical Review of World Energy. BP. **2019**, 68, 2-12.
6. "How long before we run out of fossil fuels?". Our World in Data. **2017**. <https://ourworldindata.org/how-long-before-we-run-out-of-fossil-fuels> (accessed February 17, 2021).
7. On Scene Coordinator Report on Deepwater Horizon Oil Spill. National Response Team. **2011**, 44-47.
8. Pisupati, S. "Products of Combustion". PennState College of Earth and Mineral Sciences. **2020**. <https://www.e-education.psu.edu/egee102/node/1951> (accessed February 18, 2021).
9. Crinnion W. Particulate Matter Is a Surprisingly Common Contributor to Disease. *Integr Med (Encinitas)*. **2017**, 16 (4), 8-12.
10. (a) Lüthi, D.; Le Floch, M; Bereiter, B; et al. High-resolution carbon dioxide concentration record 650,000-800,000 years before present. *Nature*. **2008**, 453, 379-382. (b) Lindsey, R. "Climate Change: Atmospheric Carbon Dioxide". NOAA. **2020**. <https://www.climate.gov/news-features/understanding-climate/climate-change-atmospheric-carbon-dioxide> (accessed February 17, 2021).
11. (a) Trends in Atmospheric Carbon Dioxide. Scripps Institution of Oceanography, Global Monitoring Laboratory. **2020**. <https://www.esrl.noaa.gov/gmd/ccgg/trends/mlo.html> (accessed February 11, 2021). (b) Beck, E. *Energy & Environ.* **2007**, 18, 259-282.
12. (a) Wang, C.; Lee, SK. Global warming and United States landfalling hurricanes. *Geophys. Res. Lett.* **2008**, 35 (2). (b) Romps, D. M.; et al. Projected increase in lightning strikes in the United States due to global warming. *Science*. **2014**, 346 (6211), 851. (c) Min, SK.; Zhang, X.; Zwiers, F; et al. Human contribution to more-intense precipitation extremes. *Nature*. **2011**, 470, 378-381.
13. Church, J.A; et al. Sea Level Change. *Climate Change 2013: The Physical Science Basis. Contribution of Working Group I to the Fifth Assessment*

- Report of the Intergovernmental Panel on Climate Change*. Cambridge University Press, Cambridge, United Kingdom and New York, NY, USA.
14. (a) De'ath, G.; Lough, J. M.; et al. Declining Coral Calcification on the Great Barrier Reef. *Science*. **2009**, 323 (5910), 116-119. (b) Doney, S. C.; Fabry, V. J.; et al. Ocean Acidification: The Other CO₂ Problem. *Annu. Rev. Mar. Sci.* **2009**, 1, 169-192.
 15. "World Energy Outlook 2020". IEA. **2020**. <https://www.iea.org/reports/world-energy-outlook-2020> (accessed February 17, 2021).
 16. Global Status Report. REN21. **2019**. https://www.ren21.net/gsr-2020/chapters/chapter_01/chapter_01/ (accessed February 18, 2021).
 17. Renewable Energy. Center for Climate and Energy Solutions. **2020**. <https://www.c2es.org/content/renewable-energy/> (accessed February 18, 2021).
 18. Barber, J.; Tran, P. D. From natural to artificial photosynthesis. *J. R. Soc. Inter.* **2013**.
 19. Du, P.; Eisenberg, R. Catalysts Made of Earth-Abundant Elements (Co, Ni, Fe) for Water Splitting: Recent Progress and Future Challenges. *Energy Environ. Sci.* **2012**, 5 (3), 6012-6021.
 20. Eckenhoff, W. T.; McNamara, W. R.; Du, P.; Eisenberg, R. Cobalt complexes as artificial hydrogenases for the reductive side of water splitting. *Biochim. Biophys. Acta. Bioeng.* **2013**, 1827, 958-973.
 21. Bard, A. J.; Faulkner, L. R. *Electrochemical Methods, 2nd ed.* J. Wiley & Sons: New York, **2001**.
 22. Gartner, F.; Denurra, S.; Losse, S.; et al. Synthesis and characterization of new iridium photosensitizers for catalytic hydrogen generation from water. *Chem. Eur. J.* **2012**, 18 (11), 3220-3225.
 23. Krishnan, C.V.; Sutin, N. Homogeneous catalysis of the photoreduction of water by visible light. 2. Mediation by a tris(2,2'-bipyridine)ruthenium(II)-cobalt(II) bipyridine system. *J. Am. Chem. Soc.* **1981**, 103, 2141-2142.
 24. Du, P.; Schneider, J.; Luo, G.; Brennessel, W. W.; Eisenberg, R. Visible light-driven hydrogen production from aqueous protons catalyzed by molecular cobaloxime catalysts. *Inorg. Chem.* **2009**, 48, 4952-4962.
 25. McNamara, W. R.; Han, Z.; Yin, C-J.; Brennessel, W. W.; Holland, P. L.; Eisenberg, R. Cobalt-dithiolene complexes for the photocatalytic and electrocatalytic reduction of protons in aqueous solutions. *PNAS*. **2012**, 109 (39), 15594-15599.
 26. Han, Z.; McNamara, W. R.; Eum, M-S.; Holland, P. L.; Eisenberg, R. A nickel thiolate catalyst for the long-lived photocatalytic production of hydrogen in a noble-metal free system. *Ang. Chem. Int. Ed.* **2012**, 51 (7), 1667-1670.

27. Panagiotakis, S.; Landrou, G.; Nikolaou, V.; Putri, A.; Hardré, R.; Massin, J.; Charalambidis, G.; Coutsolelos, A. G.; Orio, M. Efficient Light-Driven Hydrogen Evolution Using a Thiosemicarbazone-Nickel (II) Complex. *Front. Chem.* **2019**, *7*, 405.
28. (a) Hartley, C. L.; DiRisio, R. J.; Screen, M. E.; Mayer, K. J.; McNamara, W. R. Iron polypyridyl complexes for photocatalytic hydrogen generation. *Inorg. Chem.* **2016**, *55*, 8865-8870. (b) Hartley, C. L.; DiRisio, R. J.; Chang, T. Y.; Zhang, W.; McNamara, W. R. Electrocatalytic hydrogen evolution by an iron complex containing a nitro-functionalized polypyridyl ligand. *Polyhedron.* **2016**, *114*, 133-137. (c) Cavell, A. C.; Hartley, C. L.; Liu, D.; Tribble, C. S.; McNamara, W. R. An iron sulfinate complex for electrocatalytic proton reduction. *Inorg. Chem.* **2015**, 3325-3330. (d) Connor, G. P.; Mayer, K. J.; Tribble, C. S.; McNamara, W. R. Hydrogen evolution catalyzed by an iron polypyridyl complex in aqueous solutions. *Inorg. Chem.* **2014**, *53*, 5408-5410.
29. Ibadon, A. O.; Fitzpatrick, P. Heterogeneous photocatalysis: recent advances and applications. *Catalysis.* **2013**, *3*, 189-218.
30. Jaeger, C. D.; Bard, A. J. Spin Trapping and Electron Spin Resonance Detection of Radical Intermediates in the Photodecomposition of Water at Titanium Dioxide Particulate Systems. *J. Phys. Chem.* **1979**, *83* (24), 3146-3152.
31. Chen, X.; Mao, S. Titanium Dioxide Nanomaterials: Synthesis, Properties, Modifications, and Applications. *Chem Rev.* **2007**, *107*, 7, 2891-2959.
32. (a) Iijima, S.; Ichihashi, T. Single-shell carbon nanotubes of 1-nm diameter. *Nature.* **1993**, *363*, (6430) 603-605. (b) Wildoer, J. W. G.; Venema, L.C.; Rinzler, A.G.; Smalley, R.E.; Dekker, C. Electronic structure of atomically resolved carbon nanotubes. *Nature.* **1998**, *391*, (6662) 59-62. (c) Yu, M.; Lourie, O.; Dyer, M. J.; Moloni, K.; Kelly, T. F.; Ruoff, R. S. Strength and Breaking Mechanism of Multiwalled Carbon Nanotubes Under Tensile Load. *Science.* **2000**, *287* (5453), 637-640.
33. Kim, Y.; Park, H. Light-harvesting multi-walled carbon nanotubes and CdS hybrids: Application to photocatalytic hydrogen production from water. *Energy Environ. Sci.* **2011**, *4*, 685-694.
34. Yau, Y.; Li, G.; Ciston, S.; Lueptow, R.; Gray, K. Photoreactive TiO₂/Carbon Nanotube Composites: Synthesis and Reactivity. *Environ. Sci. Technol.* **2008**, *42* (13), 4952-4957.
35. Dai, K.; Peng, T.; Ke, D.; Wei, B. Photocatalytic hydrogen generation using a nanocomposite of multi-walled carbon nanotubes and TiO₂ nanoparticles under visible light irradiation. *Nanotechnology.* **2009**, *20*, 12.

36. Robel, I.; Bunker, B. A.; Kamat, P. V. Single-Walled Carbon Nanotube–CdS Nanocomposites as Light-Harvesting Assemblies: Photoinduced Charge-Transfer Interactions. *Adv. Mater.* **2005**, 17, 2458.
37. Kar, T.; Bettinger, H. F.; Scheiner, S.; Roy, A. K. Noncovalent π – π Stacking and CH--- π Interactions of Aromatics on the Surface of Single-Wall Carbon Nanotubes: An MP2 Study. *J. Phys. Chem.* **2008**, 112 (50), 20070-20075.
38. Smith, H. L.; Usala, R. L.; McQueen, E. W.; Goldsmith, J. I. Novel Polyaromatic-Terminated Transition Metal Complexes for the Functionalization of Carbon Surfaces. *Langmuir*, **2010**, 26 (5), 3342-3349.

Chapter 2. Synthesis, Characterization, Carbon-Surface Functionalization, and Catalytic-Hydrogen Generation of a Naphthalene-Terminated Iron Electrocatalyst

Introduction

In order to develop an iron catalyst capable of non-covalent adherence to carbon surfaces, the catalyst must be functionalized with an appropriate polyaromatic group. To that end, naphthalene is a promising candidate; it is commercially available, has a relatively low cost, is easy to incorporate synthetically, and much work has been published demonstrating its affinity towards carbon surfaces. On the environmental side, removal of naphthalene and other polycyclic aromatic hydrocarbons via the use of activated carbon has demonstrated naphthalene's affinity towards carbon surfaces. In one example, rice husk activated carbon derived from agricultural waste was used to adsorb and filter out naphthalene from aqueous solutions.¹ Adsorption was favorable with equilibrium between the carbon surface and naphthalene being reached after 24 hours.¹ Naphthalene has also made its way into the polymer industry, where it has been incorporated into the framework of various polymers for the non-destructive functionalization of MWCNTs. The compatibilizer, which adheres via pi-stacking, leads to well-dispersed MWCNTs in a nylon matrix, resulting in improved mechanical and electrical properties.² Furthermore, as previously mentioned, electroactive naphthalene-terminated cobalt complexes have allowed for the successful non-covalent functionalization of carbon surfaces in the form of a glassy carbon electrode.³

Though not identical to SWCNTs or MWCNTs, glassy carbon electrodes can still serve as a useful proxy when studying electrochemical and electrocatalytic activity of an adsorbed species. As a non-graphitizing carbon, glassy carbon demonstrates very high thermal stability, resistance to acid, and slower oxidation rates than other carbon types. High-resolution electron micrographs of several glassy-carbon variants revealed the microstructure consists of tightly curled single sp^2 carbon layers, which enclose micropores in the order of 1 – 5 nm in diameter. The micropores are surrounded by faceted or curved graphitic walls, typically containing 2 – 4 layer planes that resemble a giant, multi-layered fullerene (Figure 2.1). As such, glassy carbon can be modeled as mainly consisting of broken or imperfect multi-layered fullerene nanoparticles.⁴ Though not as large or pristine as the graphene surfaces found in CNTs, these smaller domains of graphene-like areas present in glassy carbon still allow for pi-stacking interactions to be studied.

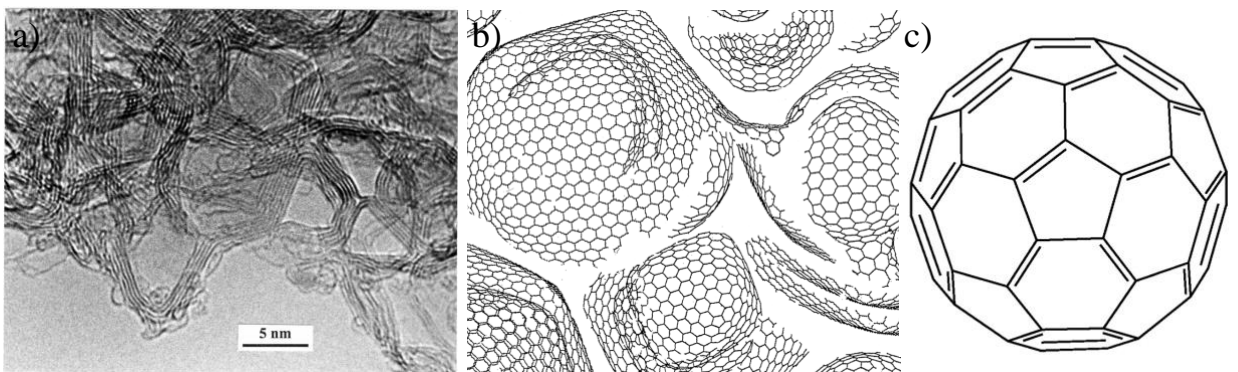


Figure 2.1. (a) TEM Image of Toyo Tanso glassy carbon GL-200 heated to 3000°C, (b) Model for the structure of high-temperature glassy carbon, and (c) Fullerene C₆₀.⁴

This work focuses on the modification of the parent catalyst $[\text{FeCl}_2(\text{L})]$, previously shown to be electrocatalytically and photocatalytically active in homogeneous systems, through the addition of a terminal naphthalene group to enable functionalization of carbon surfaces (Figure 2.2). Following synthesis, the structure of the complex was characterized and verified using X-ray crystallography. Cyclic voltammetry was then used to assess the heterogeneous behavior and time-based adsorption of this catalyst on a glassy carbon electrode surface. Additionally, the stability of the observed pi-stacking interactions between the electrode surface and the naphthalene group was tested in multiple solvent systems. Electrocatalytic hydrogen generation activity upon the addition of either TFA, tosic acid, or acetic acid was probed in addition to such activity in aqueous buffer solutions. The effects seen from varying the concentration of the acids and the identity of the acids themselves were used to support a proposed mechanism for catalysis.

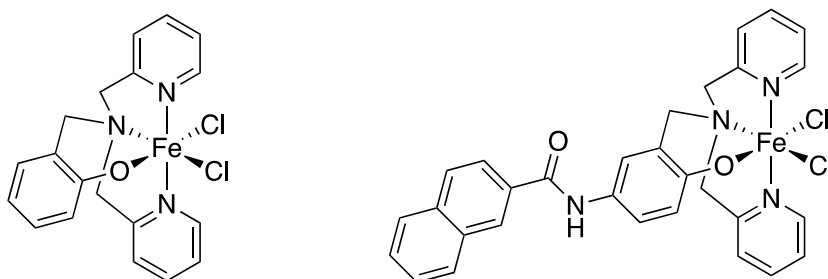


Figure 2.2. *Left:* Structure of the iron polypyridyl parent complex $[\text{FeCl}_2(\text{L})]$ and *Right:* structure of the naphthalene-functionalized complex $[\text{FeCl}_2(\text{L-Nap})]$.

Experimental Procedure

Materials

All experiments were carried out using standard Schlenk techniques under an Ar atmosphere unless otherwise indicated. All reagents were purchased from Acros Organics, Alfa Aesar, Fisher Scientific, or TCI and were used without further purification unless otherwise noted. Tetra-*n*-butylammonium hexafluorophosphate (TBAPF₆) was recrystallized from absolute ethanol.

Instrumentation

¹H and ¹³C NMR spectra were recorded on an Agilent 400MR DD2 spectrometer operating in the pulse Fourier transform mode. Chemical shifts are reported in ppm and referenced to residual solvent.

X-ray Diffractometry

Data collection, structure solution, and structure refinement were conducted by William W. Brennessel at the University of Rochester's X-ray Crystallographic Facility. A single crystal was placed onto a thin glass optical fiber and mounted onto a Rigaku XtaLab Synergy-S Dualflex diffractometer equipped with a HyPix-6000HE HPC area detector. Data collection was carried out using a PhotonJet (Cu) X-ray source. The structure was solved using SHELXT and refined using SHELXL.

Syntheses

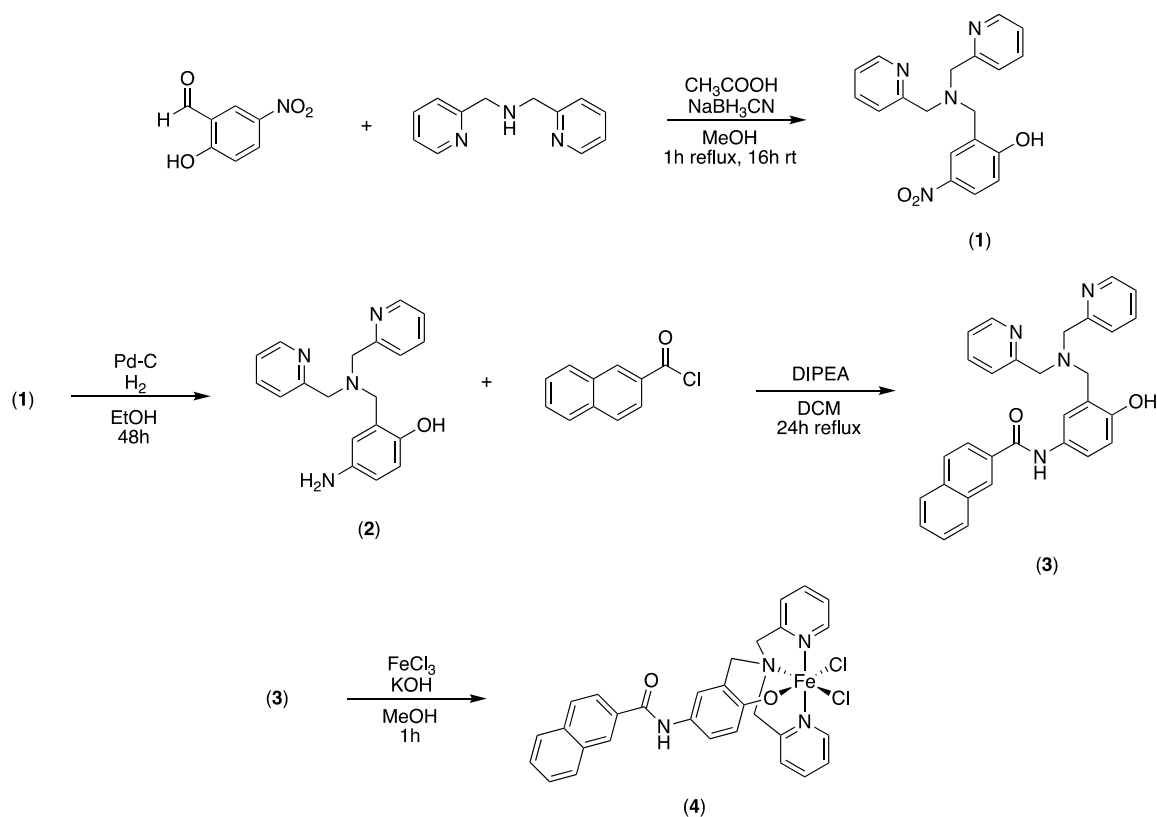


Figure 2.3. Complete synthesis of the naphthalene-functionalized iron polypyridyl complex ($[\text{FeCl}_2(\text{L-Nap})]$, 4).

Synthesis of 2-((bis(pyridin-2-ylmethyl)amino)methyl)-4-nitrophenol (1, L- NO_2)

Compound 1 was synthesized using a modified literature procedure (Figure 2.3).⁵

To a solution of 2-hydroxy-5-nitrobenzaldehyde (3.34 g, 20 mmol) in 100 mL of MeOH was added bis(pyridine-2-ylmethyl)amine (3.6 mL, 20 mmol). Glacial acetic acid (3 drops) was added followed by a solution of sodium cyanoborohydride (0.62 g, 10 mmol) in 30 mL of MeOH. After refluxing for 1 hour, the solution was stirred at room temperature overnight. 1 M HCl was added

to the resulting solution until it reached pH = 4. The red solution was evaporated to dryness, dissolved in 100 mL of saturated Na₂CO₃, and extracted with chloroform (3 x 100 mL). The organic layers were combined, dried with Na₂SO₄, and filtered through celite. The solvent was removed under vacuum to yield a red oil, which was purified using silica gel chromatography with 9:1 dichloromethane:methanol to give 1.80 g of **1** (62% yield). ¹H NMR (CDCl₃): δ 8.58 (m, 2H), 8.12 (d, 1H), 8.05 (d, 1H), 7.66 (td, 2H), 7.30 (d, 2H), 7.21 (t, 2H), 6.95 (d, 1H), 3.93 (s, 4H), 3.85 (s, 2H) (Figure A.1). ¹³C NMR (CDCl₃): δ 164.27, 157.71, 148.69, 139.68, 137.06, 126.54, 125.61, 123.52, 123.08, 122.41, 117.17, 58.67, 56.10.

Synthesis of 4-amino-2-((bis(pyridin-2-ylmethyl)amino)methyl)phenol (2**, L-NH₂)**

Compound **2** was synthesized using a modified literature procedure (Figure 2.3).⁶ To a solution of **1** (1 g, 2.86 mmol) in 180 mL EtOH, palladium on activated carbon (10% Pd) (0.1 g) was added. The reaction vessel was degassed, replenished with hydrogen gas, and allowed to stir at room temperature for 2 days. The brown solution was filtered through celite and evaporated to dryness to give 0.87 g of **2** (95 % yield). ¹H NMR (CDCl₃): δ 8.56 (m, 2H), 7.63 (td, 2H), 7.34 (d, 2H), 7.15 (m, 2H), 6.74 (d, 1H), 6.57 (dd, 1H), 6.48 (d, 1H), 3.85 (s, 4H), 3.71 (s, 2H) (Figure A.2).

Synthesis of *N*-(3-((bis(pyridin-2-ylmethyl)amino)methyl)-4-hydroxyphenyl)-2-naphthamide (3**, L-Nap)**

Compound **3** was synthesized using a modified literature procedure (Figure 2.3).⁷ To a solution of **2** (0.80 g, 2.5 mmol) in 40 mL of DCM was added a solution of 2-naphthoyl chloride (0.48 g, 2.5 mmol) and diisopropylethylamine (DIPEA, 0.44 mL, 2.5 mmol) dissolved in 20 mL DCM. The solution was refluxed for 24 hours before being diluted with 60 mL H₂O and extracted with DCM (3 x 60 mL). The organic layers were combined and washed with a saturated NaHCO₃ solution (3 x 60 mL). The organic layer was collected, dried with MgSO₄, and filtered. The volatiles were removed to yield a dark red oil, which was purified using silica gel chromatography with 9:1 dichloromethane:methanol to give 0.79 g of **3** (66% yield). ¹H NMR (CDCl₃): δ 8.57 (m, 2H), 8.36 (s, 1H), 7.90 (m, 5H), 7.64 (td, 2H), 7.57 (m, 3H), 7.36 (m, 3H), 7.15 (m, 2H), 6.94 (d, 1H), 3.90 (s, 4H), 3.82 (s, 2H) (Figure A.3). ¹³C NMR (CDCl₃): δ 165.53, 158.14, 154.77, 148.86, 136.87, 134.76, 132.64, 132.37, 129.36, 128.94, 128.67, 127.79, 127.76, 127.35, 126.87, 123.58, 123.30, 123.06, 123.03, 122.28, 121.70, 116.90, 58.98, 56.80.

Synthesis of [FeCl₂(L-Nap)] (4**)**

Compound **4** was synthesized using a modified literature procedure (Figure 2.3).⁷ To a solution of **3** (0.20 g, 0.42 mmol) and KOH (0.024 g, 0.42 mmol) in 10 mL MeOH was added a solution of FeCl₃•6H₂O (0.11 g, 0.42 mmol) in 8 mL MeOH. The solution immediately turned blue with a visible precipitate. The reaction mixture was stirred at room temperature for 1 hour and filtered. The solid was

collected and washed with cold MeOH (3 x 10 mL) to give 0.18 g of **4** (72% yield). The product was crystallized by diffusion of toluene into a concentrated solution of **4** in DCM. Crystals suitable for X-ray diffraction were grown using the same procedure but with the omission of KOH during the synthesis.

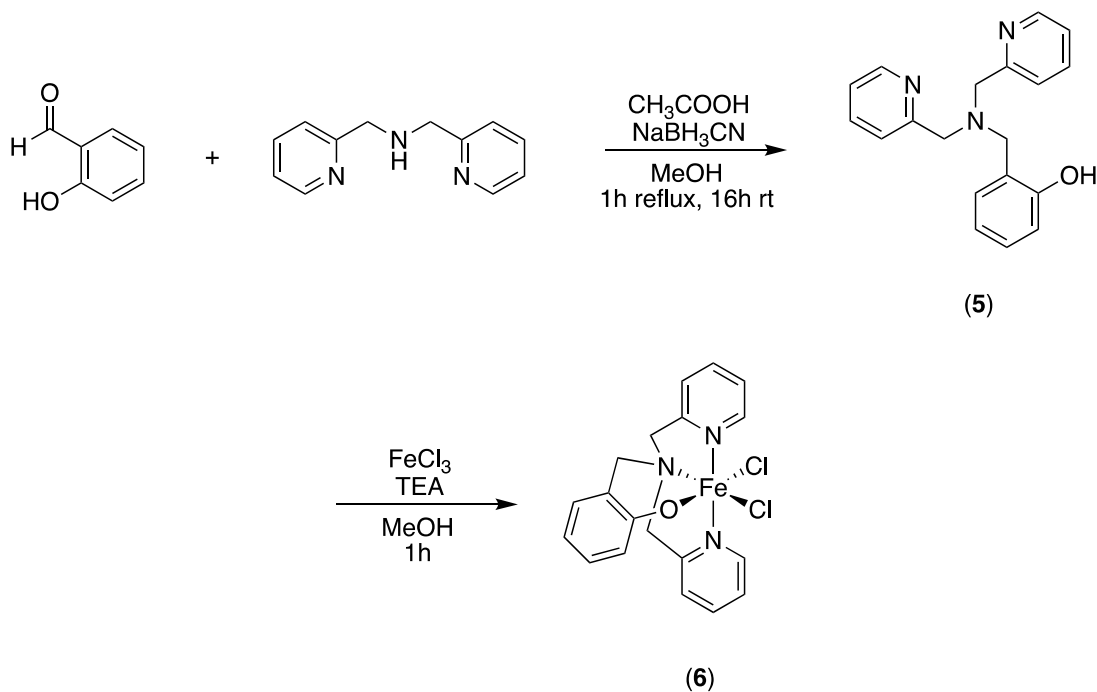


Figure 2.4. Complete synthesis of the iron polypyridyl parent complex $[\text{FeCl}_2(\text{L})]$, **6**.

Synthesis of 2-((bis(pyridin-2-ylmethyl)amino)methyl)phenol (**5**, L)

Compound **5** was synthesized using a modified literature procedure (Figure 2.4).⁵

To a solution of salicylaldehyde (1.00 mL, 10 mmol) in 50 mL of MeOH was added bis(pyridine-2-ylmethyl)amine (1.8 mL, 10 mmol). Glacial acetic acid (3 drops) was added followed by a solution of sodium cyanoborohydride (0.31 g, 5 mmol) in 15 mL of MeOH. After refluxing for 1 hour, the solution was stirred at room temperature overnight. 1 M HCl was added to the resulting solution until it

reached pH = 4. The amber solution was evaporated to dryness, dissolved in 75 mL of saturated Na₂CO₃, and extracted with chloroform (3 x 75 mL). The organic layers were combined, dried with Na₂SO₄, and filtered through celite. The solvent was removed under vacuum to yield an amber oil, which was purified using silica gel chromatography run sequentially with 19:1 and 9:1 dichloromethane:methanol to give 1.92 g of **1** (63% yield). ¹H NMR (CDCl₃): δ 8.49 (m, 2H), 7.57 (td, 2H), 7.29 (d, 2H), 7.10 (m, 3H), 7.00 (d, 1H), 6.84 (d, 1H), 6.70 (t, 1H), 3.81 (s, 4H), 3.73 (s, 2H) (Figure A.4). ¹³C NMR (CDCl₃): δ 158.22, 157.37, 148.77, 136.81, 129.05, 123.19, 122.87, 122.19, 118.86, 116.51, 59.05, 56.93.

Synthesis of [FeCl₂(L)] (6**)**

Compound **6** was synthesized using a modified literature procedure (Figure 2.4).⁵ To a solution of **5** (1.00 g, 3.27 mmol) and triethylamine (0.36 mL, 2.61 mmol) in 6 mL MeOH was added a solution of FeCl₃•6H₂O (0.71 g, 2.61 mmol) in 5 mL MeOH. The solution immediately turned navy blue with a visible precipitate. The reaction mixture was stirred at room temperature for 1 hour and filtered. The solid was collected and washed with cold MeOH (3 x 10 mL) to give 0.83 g of **6** (73% yield). The product was crystallized by diffusion of either hexane or diethyl ether into a concentrated solution of **6** in DCM.

Preparation of Buffer Solutions

A citric acid/sodium phosphate buffer system was used for analyses. The buffers were prepared in batches of 20 mL using aqueous solutions of 0.1 M citric acid and 0.2 M Na₂HPO₄ (Table 2.1).

Table 2.1. Preparation of Buffer Solutions.

pH	Citric Acid (0.1 M, mL)	Na ₂ HPO ₄ (0.2 M, mL)
3.8	12.90	7.10
4.6	10.65	9.35
5.4	8.85	11.15
6.2	6.78	13.22

Electrochemistry Experiments

Cyclic Voltammetry

All electrochemical experiments were performed under an atmosphere of Ar using a CH Instruments 620D potentiostat with a CH Instruments 680 Amp booster. Cyclic voltammograms were acquired using a standard three-electrode cell. A saturated calomel reference electrode (SCE) was used for all experiments. Prior to each acquisition, the platinum auxiliary electrode was polished using 0.05 μm alumina powder paste on a cloth-covered polishing pad, followed by rinsing with water and acetonitrile. The glassy carbon working electrode (diameter = 0.30 cm) was polished in the same manner and was subsequently added to either the electrochemical cell or catalyst-soak solution

depending on the experiment (specific details below). Ferrocene was used as an internal standard to correct for drifting of the reference electrode.

Scan Rate Dependence Study

A polished glassy carbon electrode was soaked overnight in a 0.5 mM solution of **[FeCl₂(L-Nap)]** in acetonitrile. The electrode was thoroughly rinsed with acetonitrile and added to an electrochemical cell containing 5 mL of 0.1 M TBAPF₆ in CH₃CN. Cyclic voltammograms were taken at a scan rate of 1000, 800, 600, 400, and 200 mV/s respectively.

Adsorption Time-Dependence Study

A polished glassy carbon electrode was soaked in a 0.5 mM solution of **[FeCl₂(L-Nap)]** in acetonitrile for time periods ranging from 1 – 1710 minutes. After soaking, the electrode was thoroughly rinsed with acetonitrile and added to an electrochemical cell containing 5 mL of 0.1 M TBAPF₆ in CH₃CN. Cyclic voltammograms were taken at a scan rate of 200 mV/s 5 minutes after adding the glassy carbon electrode to the cell.

Variable Solvent-Stability Study

A polished glassy carbon electrode was soaked overnight in a 0.5 mM solution of **[FeCl₂(L-Nap)]** in acetonitrile. The electrode was thoroughly rinsed with acetonitrile followed by the solvent (CH₃CN, DCM, acetone, pentane, EtOH, or water) used in the subsequent soak. The electrode was suspended in 15 mL of a

particular solvent (CH₃CN, DCM, acetone, pentane, EtOH, or water) for 30 minutes before being removed, rinsed with acetonitrile, and added to an electrochemical cell containing 5 mL of 0.1 M TBAPF₆ in CH₃CN. Cyclic voltammograms were taken at a scan rate of 200 mV/s 2 minutes after adding the glassy carbon electrode to the cell.

Variable Catalyst-Adsorption Control Study

Polished glassy carbon electrodes were soaked overnight in a 0.5 mM solution of either **[FeCl₂(L)]**, **[FeCl₂(L-Nap)]**, **[FeCl₂(L-NO₂)]**, **[FeCl₂(L-(NO₂)₂)]**, or **[FeCl₂(L-Cl₂)]** in acetonitrile. After soaking, the electrodes were thoroughly rinsed with acetonitrile and added to respective electrochemical cells containing 5 mL of 0.1 M TBAPF₆ in CH₃CN. Cyclic voltammograms were taken at a scan rate of 200 mV/s 10 minutes after adding the glassy carbon electrode to the cell.

Acid Addition Studies

A polished glassy carbon electrode was soaked overnight in a 0.5 mM solution of **[FeCl₂(L-Nap)]** in acetonitrile. The electrode was rinsed with acetonitrile and added to an electrochemical cell containing 5 mL of 0.1 M TBAPF₆ in CH₃CN. Cyclic voltammograms, which were taken 10 minutes after addition of the working electrode, were taken without acid and after additions of 10, 20, 30, and 40 μ L of either trifluoroacetic acid (TFA, 0.2 M), p-toluenesulfonic acid (tosic acid, 0.2 M), or glacial acetic acid (2.0 M). The working electrode was polished and resoaked overnight in **[FeCl₂(L-Nap)]** before each scan.

pH Dependence Study

A polished glassy carbon electrode was soaked overnight in a 0.5 mM solution of **[FeCl₂(L-Nap)]** in acetonitrile. The electrode was rinsed with acetonitrile and water before it was added to an electrochemical cell containing 5 mL of an aqueous buffer solution (pH = 3.8 – 6.2), which served as the electrolyte. Cyclic voltammograms, which were run 2 minutes after addition of the electrode, were taken at 100 mV/s from 0.0 to -1.4 V for pH = 3.8 and from 0.0 to -1.6 V for pH = 4.6 – 6.2.

Results and Discussion

Synthesis and Structural Characterization

Synthesis began with the reductive amination of 2-hydroxy-5-nitrobenzaldehyde to give **L-NO₂** in good yield. Reduction of the nitro- group was accomplished via a palladium-catalyzed hydrogenation to give **L-NH₂**, which was coupled to 2-naphthoyl chloride through amide-bond formation to give **L-Nap**. The ligand was coordinated to Fe(III), and crystals suitable for X-ray diffraction were grown through the slow diffusion of toluene into a concentrated solution of **4** in DCM.

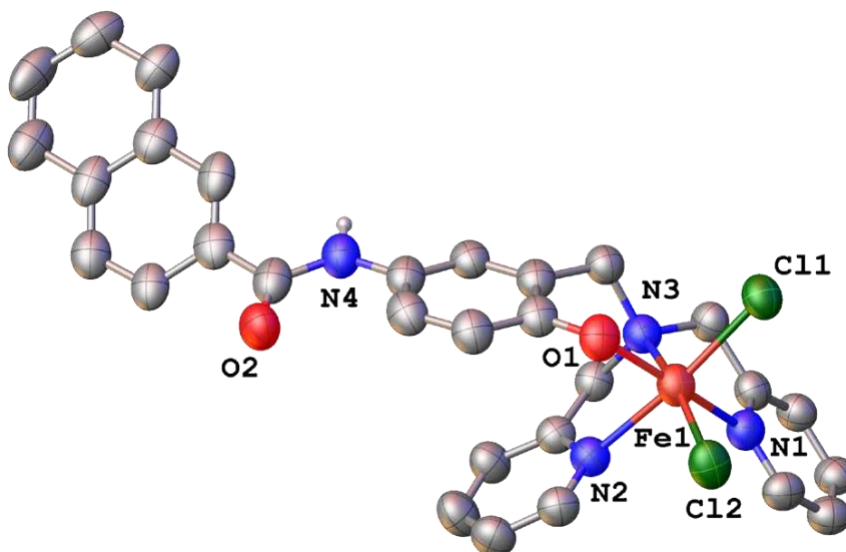


Figure 2.5. ORTEP diagram of **4** with Fe (orange), O (red), N (blue), Cl (green), and C (gray). Hydrogen atoms are omitted for clarity. Anisotropic displacement ellipsoids are drawn at the 50% probability level.

The complex presents itself as a disoriented octahedron, with the Fe(III) center bound to two chlorides and ligand **3** (Figure 2.5). Distortion is evident

based on deviation from the expected octahedral-bond angles, which are 180° and 90° for axial and equatorial respectively. Exemplifying this are the O(1)-Fe(1)-N(1) and N(1)-Fe(1)-N(3) bond angles, which are 163.21° and 74.13° respectively. Departure from octahedral-bond angles likely occurs to minimize strain arising from the 6-membered chelate ring, which results from coordination of the phenolate and N(3) to the iron center. Additionally, disorder within the crystal arises from a planar flip of the naphthalenyl group, which is modeled as being disordered over two positions (0.80:0.20); because the two orientations do not fill the exact same relative special volume, the co-crystallized solvent is disorganized to accommodate them (Figure A.5). Important bond lengths and angles are shown in Table 2.2, and X-ray crystallographic data is given in Table A.1 for reference.

Table 2.2. Selected bond lengths [Å] and angles [°] for **[FeCl₂(L-Nap)]**.

Bond Length (Å)	
Fe(1)-O(1)	1.890(2)
Fe(1)-N(1)	2.172(3)
Fe(1)-N(2)	2.208(3)
Fe(1)-N(3)	2.234(3)
Fe(1)-Cl(1)	2.3272(10)
Fe(1)-Cl(2)	2.3115(10)
Bond Angle (°)	
N(1)-Fe(1)-Cl(1)	89.68(8)
N(1)-Fe(1)-Cl(2)	95.68(8)
N(1)-Fe(1)-N(2)	87.71(10)
N(1)-Fe(1)-N(3)	74.13(10)
N(2)-Fe(1)-Cl(1)	169.45(8)
N(2)-Fe(1)-Cl(2)	93.10(8)
N(2)-Fe(1)-N(3)	76.36(10)
N(3)-Fe(1)-Cl(1)	93.09(7)
N(3)-Fe(1)-Cl(2)	165.41(8)

Adsorption Behavior and Characterization

Electrochemical examination of **4** began with using cyclic voltammetry to observe and characterize its adsorption behavior on the surface of glassy carbon electrodes. These electrodes were soaked overnight in a concentrated solution of **4** in acetonitrile before being removed, rinsed with CH₃CN, and added to an electrochemical cell containing pure 0.1 M TBAPF₆/CH₃CN. The working electrode was cycled between +0.60 and -0.55 V vs. SCE to observe only the

Fc⁺/Fc (internal standard) and Fe(III)/Fe(II) redox couples and to minimize the possibility of reductive desorption.

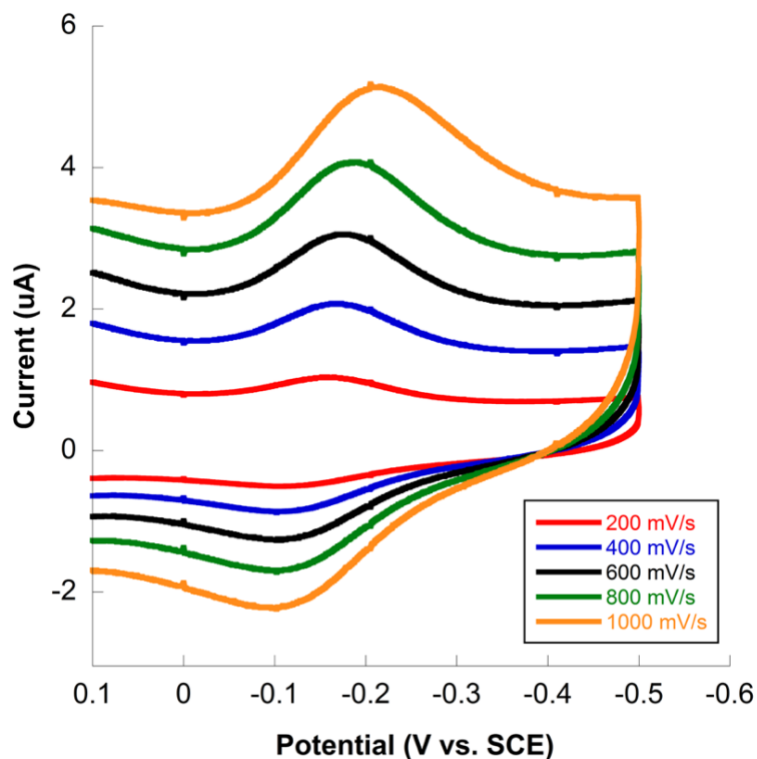


Figure 2.6. Cyclic voltammograms of **4** adsorbed to the surface of a glassy carbon electrode in 5 mL of 0.1 M TBAPF₆ in CH₃CN taken at scan rates of 200 – 1000 mV/s.

Since there was no redox-active material added to the electrochemical cell besides the ferrocene internal standard, the observed response must come from catalyst adsorbed to the surface of the electrode. Cyclic voltammograms of **4** taken at various potential sweep rates show a reversible Fe(III)/Fe(II) reduction at -0.20 V vs. SCE, which is about 100 mV more positive than the homogeneous parent complex **6** (Figure 2.6). For an electroactive adsorbate, the expected peak separation between the anodic and cathodic waves (ΔE_p) is expected to be less

than 58 mV.⁸ This behavior is observed for the 200 and 400 mV/s scans, in which ΔE_p is 42 and 43 mV respectively, of **4**. However, ΔE_p continues to increase with the scan rate and reaches upwards of 104 mV with a potential sweep rate of 1000 mV/s. This deviation from the ideal behavior indicates that a kinetic barrier to electron transfer exists.⁹ Despite these variations, ΔE_p for the naphthalene complex is still significantly less than **6** at all potential sweep rates (Figure A.6); the ΔE_p for **6** ranges from 150 mV – 380 mV in comparison to 42 – 104 mV for **4** using potential sweep rates of 200 – 1000 mV/s. A direct comparison between the two complexes is shown in Figure 2.7, which highlights the smaller potential difference of the redox couple in **4**. The smaller range indicates **4** has adsorbed onto the electrode surface and is not free in solution like **6**.

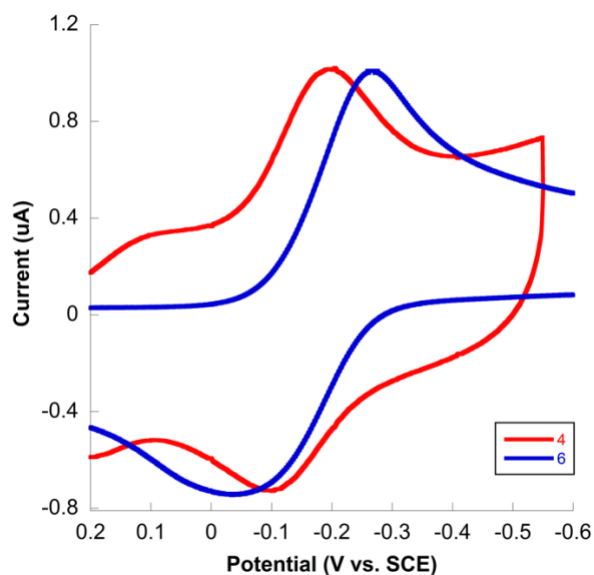


Figure 2.7. Cyclic voltammograms of **4** adsorbed onto the surface of a glassy carbon electrode and 0.1 mg of **6** in 5 mL of 0.1 M TBAPF₆ in CH₃CN at a potential sweep rate of 200 mV/s. The current intensity of **6** has been scaled down by a factor of 10 for ease of comparison.

Freely diffusing and adsorbed material can also be distinguished by the relationship between peak current and scan rate. For freely-diffusing material, the peak current increases linearly with the square root of the sweep rate.⁹ However, for an electrode-adsorbed species, the current increases linearly with the sweep rate as described by (Equation 2.1):

$$i_p = \frac{n^2 F^2}{4RT} \nu A \Gamma^* \quad (2.1)$$

where i_p is the peak current, n is the number of electrons transferred in the redox event, F is the Faraday constant, R is the gas constant, T is the temperature, ν is the potential sweep rate, A is the surface area of the electrode, and Γ^* is the surface coverage of the adsorbed species.⁹ The linearity observed ($R^2 = 0.99972$) in the plot of cathodic peak current (i_{cp}) versus potential sweep rate for **4** confirms that the electrochemical response is due to material adsorbed on the surface of the glassy carbon working electrode rather than from material freely diffusing in solution (Figure 2.8).

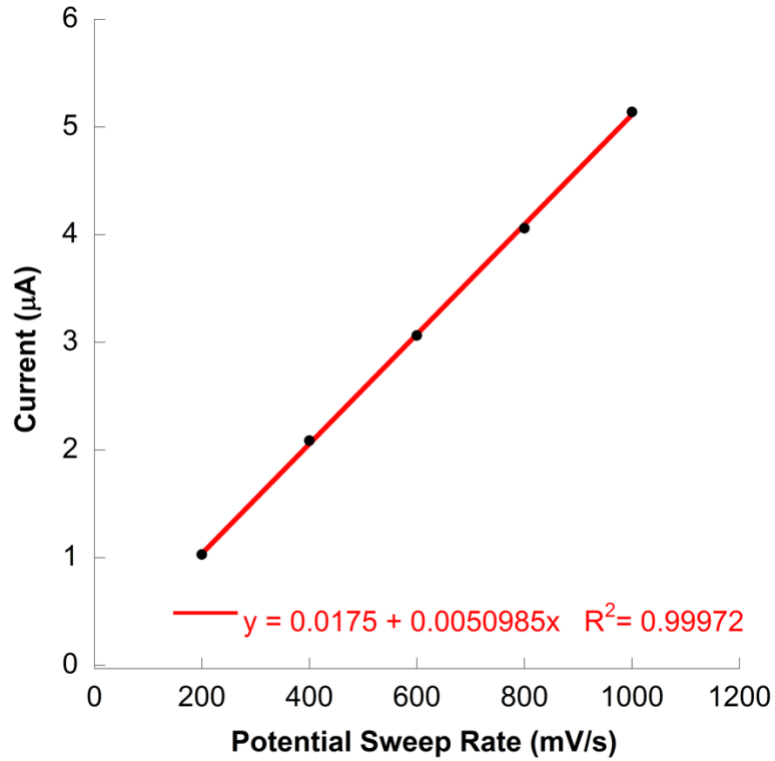


Figure 2.8. Cathodic peak current versus potential sweep rate for **4**.

Using the above relationship between peak current and potential sweep rate, the surface coverage of **4** on the glassy carbon electrode (0.3 cm diameter) at 298 K can be found:

$$i_p = \frac{n^2 F^2}{4RT} v A \Gamma^*$$

$$i_p = \frac{1^2 * 96,485^2}{4 * 8.314 * 298} * v * 0.071 * \Gamma^* = (6.64 * 10^5) * v * \Gamma^*$$

$$\frac{i_p}{v} = slope = 5.09 * 10^{-6} = (6.64 * 10^5) * \Gamma^*$$

$$\Gamma^* = 7.7 * 10^{-11} \text{ mol/cm}^2$$

With a value of 7.7×10^{-11} mol/cm², the surface coverage of **4** is similar to that of Goldsmith's previously-reported naphthalene-functionalized cobalt complex, which was found to have a value of 6.0×10^{-11} mol/cm².³

To confirm that the adsorption behavior observed was a specific result of pi-stacking interactions between the naphthalene moiety and the electrode surface, similar iron complexes with different functional groups were tested. This includes the unsubstituted parent complex **6** in addition to nitro- **7**, dinitro- **8**, and dichloro- **9** substituted iron polypyridyl complexes. However, when CVs were taken using electrodes soaked overnight in individual solutions of these complexes, no electrochemical response was observed (Figure 2.9). Since each tested catalyst has the same basic framework, this indicates that adsorption functionally is granted by the naphthalene moiety alone and not due to other structural features of the catalyst.

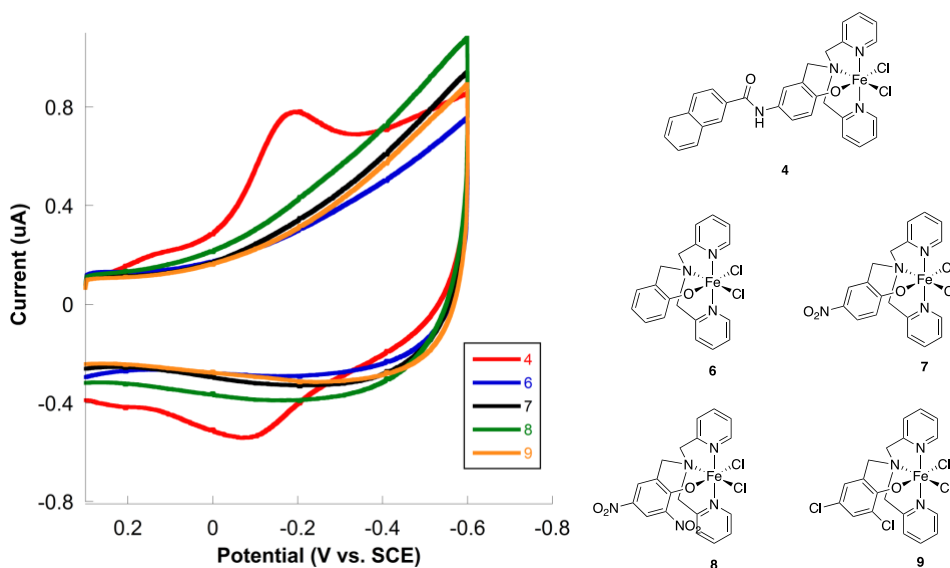


Figure 2.9. Variable catalyst adsorption study. Cyclic voltammograms were scanned at 200 mV/s in 5 mL of 0.1 M TBAPF₆ in CH₃CN.

After confirming that adsorption on the glassy carbon surface was specific to the naphthalene-functionalized complex, the adsorption kinetics as a function of time were studied. This was performed in order to determine the soak time required for material adsorbed on the electrode surface to reach equilibrium with that of the solution. The glassy carbon electrode was polished, immersed in a 0.5 mM solution of **4** for a specific time period, rinsed with acetonitrile, added to a fresh electrochemical cell, and scanned from +0.22 to -0.55 V to view only the Fe(III)/Fe(II) redox couple (Figure 2.10). Data was collected at time points of 1, 5, 10, 20, 30, 60, 120, 180, 360, 720, 1110, and 1710 minutes.

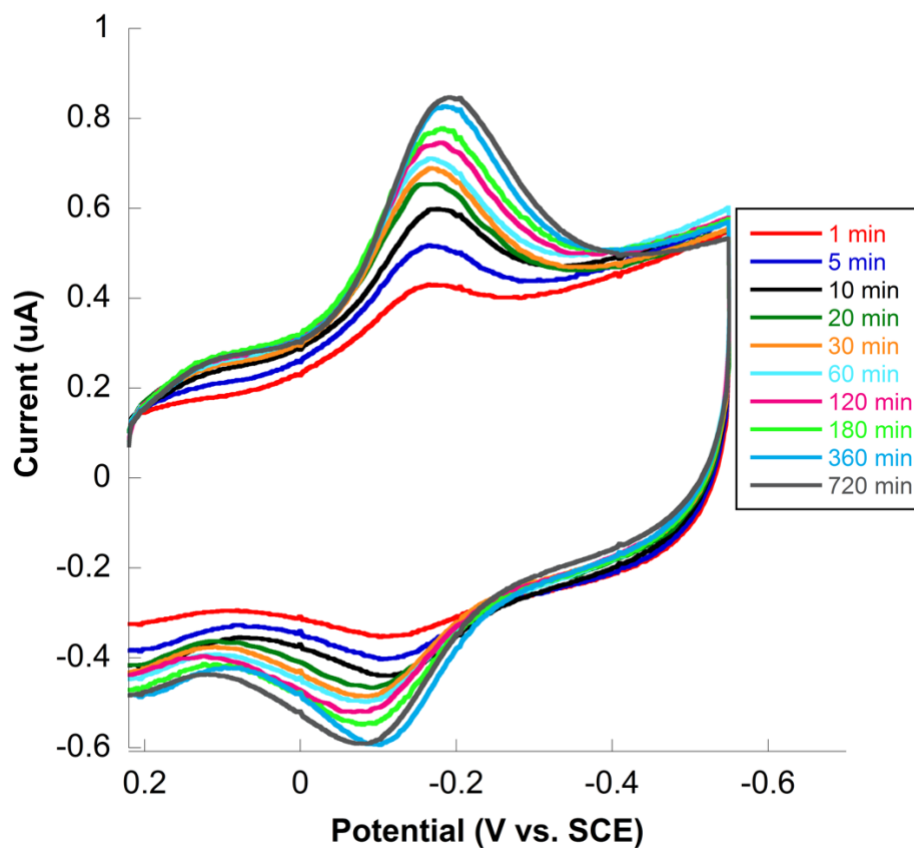


Figure 2.10. Cyclic voltammograms, taken in 5 mL of 0.1 M TBAPF₆ in CH₃CN at 200 mV/s, for the time-dependent soak study of **4**.

As anticipated, the measured current, which is linearly related to the surface coverage of the catalyst, initially grows with soak time. The most rapid growth is seen within the first 60 minutes, in which the cathodic peak current reaches 83% of its maximum value (Figure 2.11). Though slowly, i_{cp} continues to rise and reaches a peak around 720 minutes, which marks the point at which the adsorbed material is at equilibrium with the freely-diffusing material in the solution. However, a slight decrease in the maximum cathodic current is observed in the longer timepoints; 98% and 96% of the peak current is seen in the 1110 and 1710 minute scans respectively. Though not severe, this decrease may be attributed to contamination of the soak solution with atmospheric water over time, which could interfere with and limit adsorption.

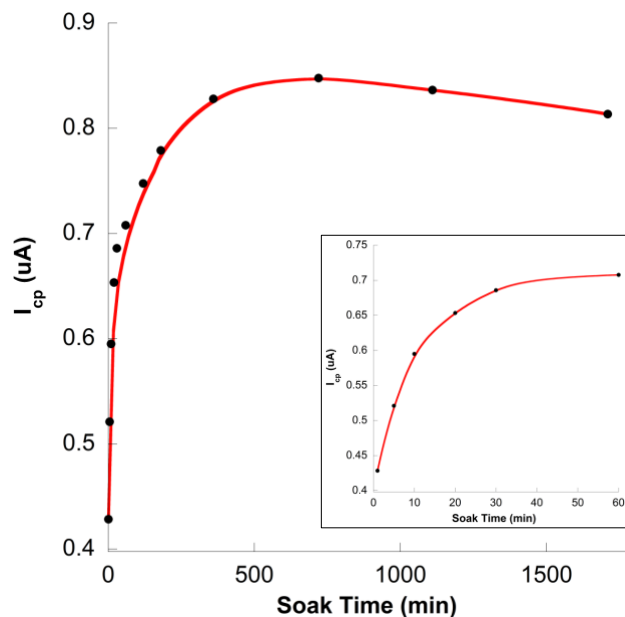


Figure 2.11. Adsorption kinetics of **4** as a function of time. Inset plot highlights rapid adsorption during the first 60 minutes.

Lastly, the strength and stability of the adsorbed naphthalene complex on the electrode surface was tested in a variety of solvents: acetonitrile, dichloromethane, pentane, acetone, ethanol, and water. A glassy carbon electrode was polished, soaked in a solution of **4** to the point of adsorption saturation, removed, rinsed, and immersed in one of the pure solvents for 30 minutes. After which, the electrode was removed, rinsed, added to a fresh electrochemical cell containing only 0.1 M TBAPF₆ in acetonitrile, and cyclic voltammograms were obtained using the standard procedure. Data from these solvent-soaks were compared to a scan of a glassy carbon electrode fully-saturated with the naphthalene-functionalized complex (Figure 2.12).

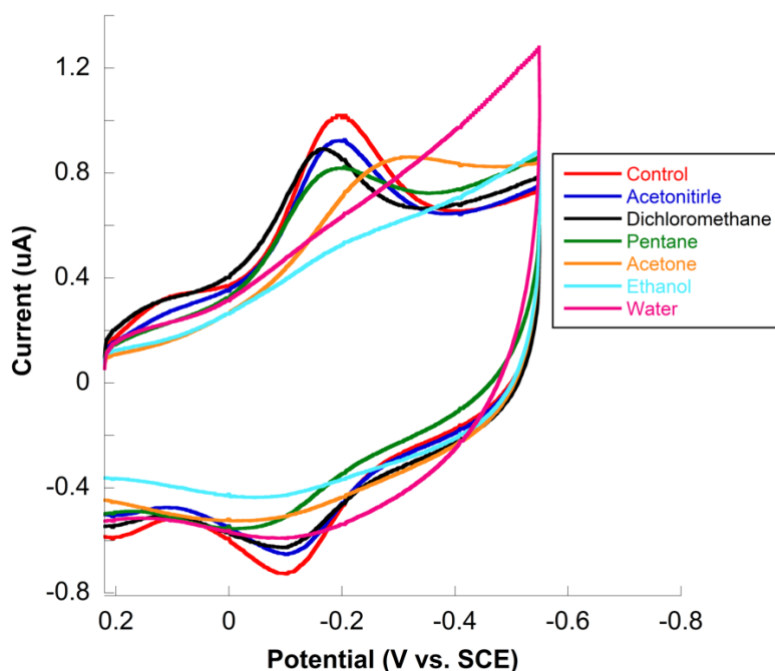


Figure 2.12. Impact of 30-minute solvent soaks on the adsorption of **4** to the surface of a glassy-carbon electrode. Cyclic voltammograms were scanned at 200 mV/s in 5 mL of 0.1 M TBAPF₆ in CH₃CN.

The highest degree of surface stability of the naphthalene complex on the glassy carbon electrode surface is seen in acetonitrile and dichloromethane; the 30-minute electrode soaks in each solvent only resulted in a 10 and 13 % decrease in the peak cathodic current respectively compared to the control electrode saturated with **4**. However, surface stability of the complex is more limited in pentane, in which the 30-minute soak resulted in a 20% loss in i_{cp} . The acetone soak also led to instability, which is evident by the catalyst's broad cathodic peak and lack of an anodic peak, which indicates desorption. Lastly, **4** did not exhibit any surface stability in the presence of either ethanol or water, as no appreciable redox event can be seen in these scans. This may be attributed to the hydrogen bonding capability of these solvents; hydrogen bonding between these solvents and the amide in **4** may be a more favorable interaction than pi-stacking between the naphthalenyl group and the glassy carbon electrode surface, leading to rapid desorption.

Another noticeable feature in the acetonitrile- and dichloromethane-soak voltammograms is the variation in the cathodic peak potential (E_{cp}), which occurs at -0.20 and -0.16 V vs. SCE respectively. Since both scans were taken in acetonitrile, the difference in E_{cp} may arise from a CH_3CN coordination effect: soaking the electrode overnight in a solution of **4** in acetonitrile alters the original complex and leads to some degree of CH_3CN coordination. The subsequent 30-minute soak in dichloromethane solvates and releases CH_3CN from the coordination sphere of the of the complex. When this electrode is removed from the soak solution, rinsed, and added to an electrochemical cell containing

acetonitrile, there isn't enough time for full coordination to reoccur before the voltammogram is acquired, which accounts for a positive shift in E_{cp} .

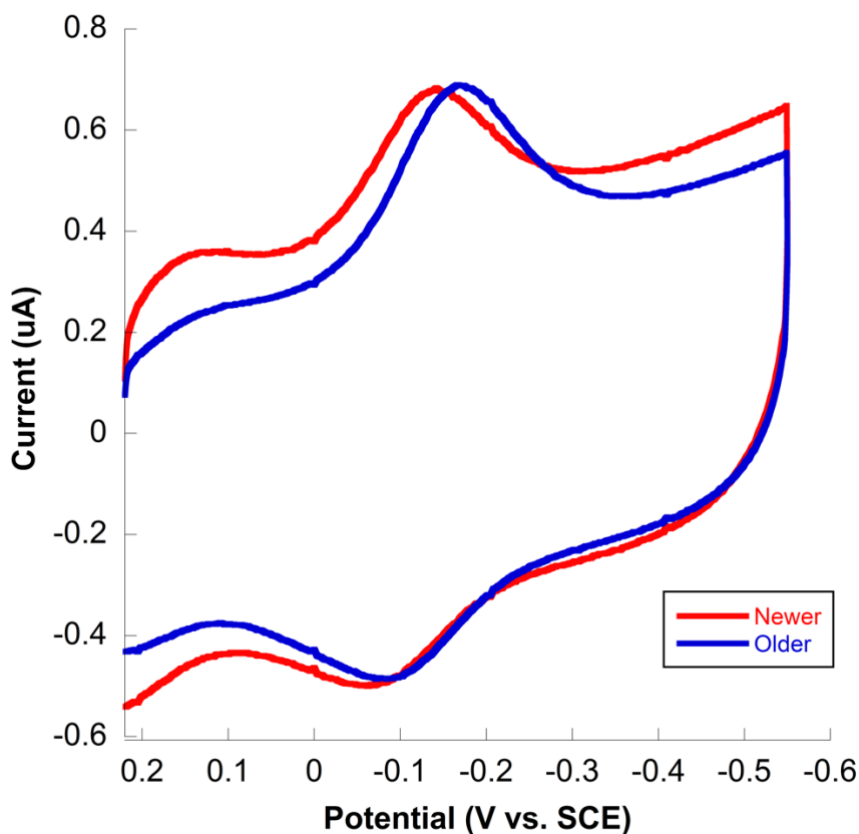


Figure 2.13. Variation in the peak cathodic potential arising from a freshly-prepared soak solution and a day old soak solution of **4** in acetonitrile. Cyclic voltammograms were scanned at 200 mV/s in 5 mL of 0.1 M TBAPF₆ in CH₃CN.

This theory is also supported based on data collected for short electrode soaks in freshly-made and day-old solutions of **4** in acetonitrile (Figure 2.13). A polished electrode was immersed in each 0.5 mM solution for 30 minutes, and cyclic voltammograms were obtained as per usual. In comparison to the day-old solution soak, the E_{cp} in the scan of the electrode soaked in the fresh solution of **4** is positively offset by 30 mV. As with the difference seen in the acetonitrile and

dichloromethane soaks, this positive shift can be rationalized by considering the impact of acetonitrile coordination: in the freshly-made solution of **4**, equilibrium has not yet been reached between acetonitrile and the coordination sphere of the complex. As such, the complex exhibits slightly different electrochemical behavior.

Electrocatalytic Proton Reduction: TFA Additions

In addition to monitoring adsorption behavior, cyclic voltammetry can be used to assess the ability of a complex to function as a catalyst for proton reduction. Upon the addition of a weak acid as a proton source, an active electrocatalyst for the hydrogen evolution reaction will result in an irreversible cathodic wave, corresponding to the reduction of protons, that is otherwise not present. Previously, the parent complex **6** has been proven to be an active electrocatalyst for such proton reduction; upon addition of TFA, an irreversible reduction event, corresponding to proton reduction, is observed at -1.17 V vs. SCE, and this current is enhanced with higher concentrations of TFA (Figure 2.14). A second-order dependence on the proton concentration is evident based on the linear relationship between i_c and [TFA]. Additionally, a shift, corresponding to the protonation of the phenol group and indicating a CECE mechanism, in the Fe(III)/Fe(II) redox couple from -0.28 to +0.10 V vs. SCE is observed for **6**.¹⁰

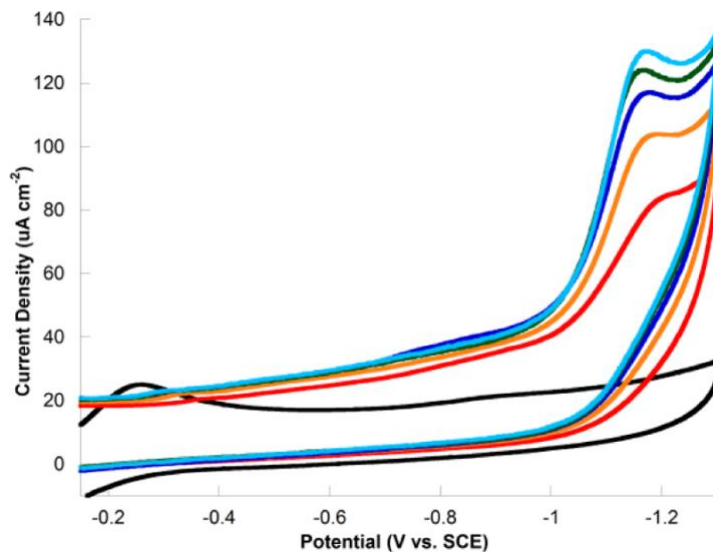


Figure 2.14. Cyclic voltammograms of 0.5 mM **6** in 0.1 M TBAPF₆ in CH₃CN at 200 mV/s without acid (black), and upon the addition of 2.2 mM TFA (red), 4.4 mM TFA (orange), 6.6 mM TFA (dark blue), 8.8 mM TFA (green), and 11.0 mM TFA (light blue).¹⁰

The naphthalene-functionalized complex **4** was also found to be an active electrocatalyst for proton reduction (Figure 2.15). Upon addition of TFA, an irreversible catalytic wave is observed at -1.13 V vs. SCE, and there is a slight, steady positive shift in this potential as [TFA] increases. At the same TFA concentration, the catalytic wave for **4** occurs at a potential 120 mV more positive than that of **6**. The peak current of this proton reduction wave increases linearly with [TFA], suggesting a second order dependence on [H⁺]. Additionally, a positive shift of up to 340 mV in the Fe(III)/Fe(II) redox couple potential, which occurs at -0.20 V in the absence of acid, was observed with increasing [TFA] (Table 2.3). This behavior mirrors that of **6**.

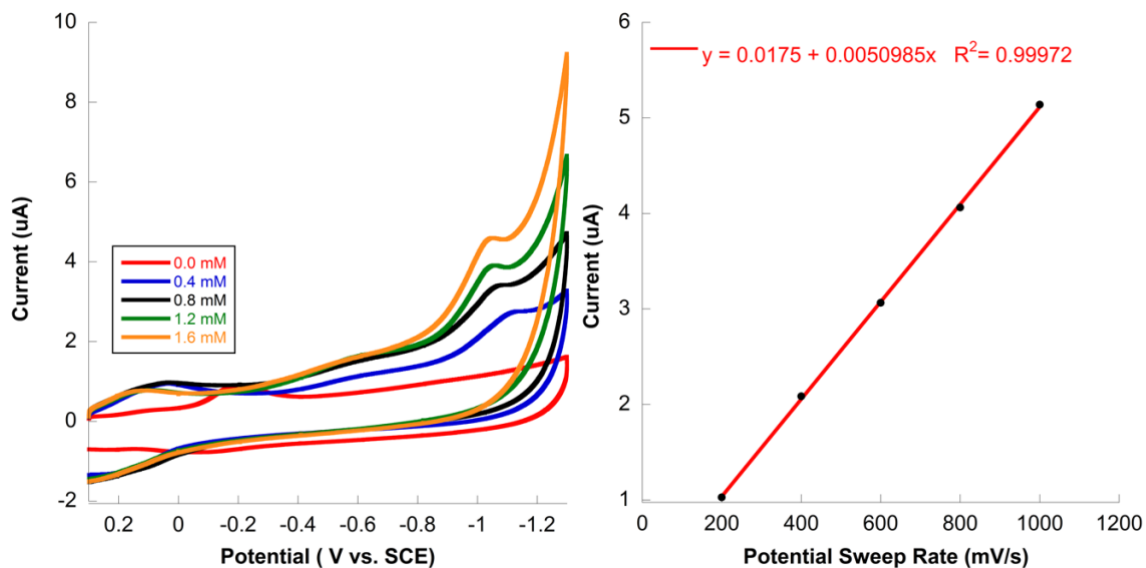


Figure 2.15. *Left:* Cyclic voltammograms of surface-adsorbed **4** in 5 mL of 0.1 M TBAPF₆ in CH₃CN at 200 mV/s without acid (red) and in the presence of increased concentrations of TFA. A catalytic reduction is visible at -1.08 V vs. SCE. *Right:* Peak current of the proton reduction peak vs. [TFA]. A linear relationship between the two is indicated by $R^2=0.9997$.

Table 2.3. Catalytic-wave features upon TFA addition for **4**.

[TFA] (mM)	Fe(III)/Fe(II) redox couple (V vs. SCE)	Proton Reduction Wave (V vs. SCE)
0.0	-0.20	N/A
0.4	0.04	-1.13
0.8	0.07	-1.09
1.2	0.10	-1.06
1.6	0.14	-1.05

The catalytic activity can be determined by taking a ratio of the peak height of the irreversible catalytic wave (i_c) and the peak height of the catalytic

reduction wave (i_p) (Figure 2.16). A larger i_c/i_p indicates higher catalytic activity for proton reduction.¹⁰ The i_c/i_p at 200 mV/s was determined to be 5.46 compared to 7.83 for that of **6**.

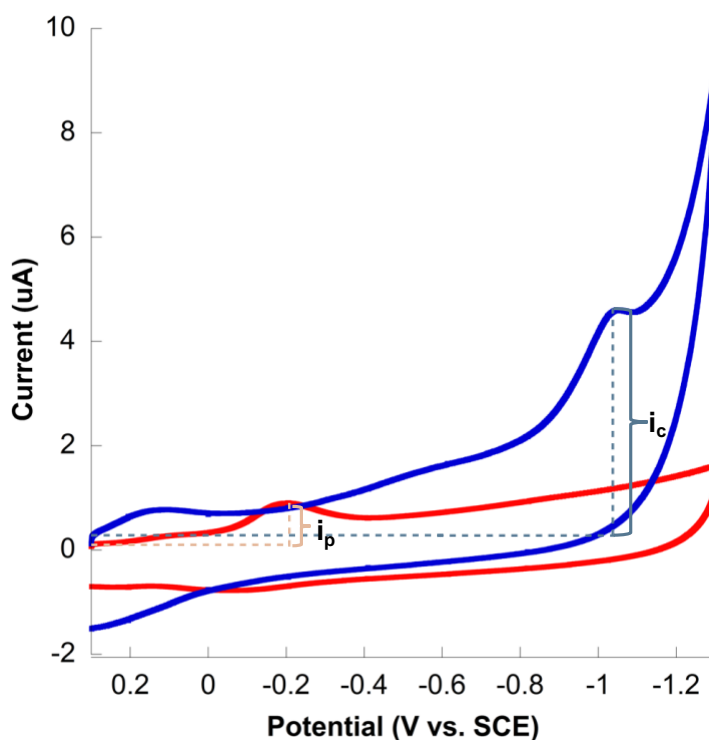


Figure 2.16. Cyclic voltammograms of surface-adsorbed **4** in 5 mL of 0.1 M TBAPF₆ in CH₃CN at 200 mV/s without acid (red) and in the presence of 1.6 mM TFA (blue) with i_c and i_p , highlighted.

In order to evaluate the efficiency of **4** as a catalyst for proton reduction, it is useful to determine its overpotential, an electrochemical parameter that can be compared to that of other catalytic systems. Overpotential is the potential difference between a half-reaction's thermodynamically determined reduction potential and the potential at which the redox event is experimentally observed.⁹ Therefore, a lower overpotential indicates that less energy input is wasted in the

driving of the catalytic cycle. The overpotential can be determined by taking the difference between the half-wave potential ($E_{1/2}$) of the catalytic reduction event and a reference potential of the proton source (E_{ref}), which is TFA in this case. This reference potential considers and corrects for the effects of homoassociation exhibited by TFA in acetonitrile. Homoassociation is a phenomenon in which there is an association between an acid and its conjugate base through a hydrogen bond. The association of this pair leads to the enhancement of the acidity of an acid, and this effect is amplified at higher acid concentrations. As a result, ionization of an acid varies nonlinearly with concentration.¹¹ Without correction, catalytic activity can be overestimated.

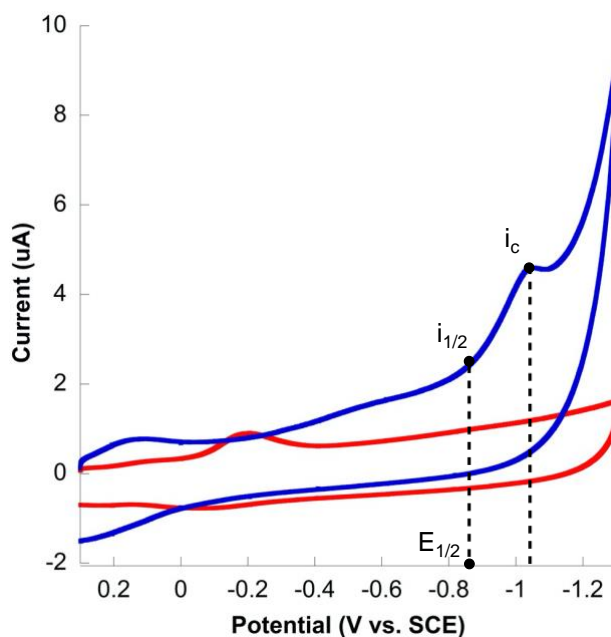


Figure 2.17. Cyclic voltammograms of surface-adsorbed **4** in 5 mL of 0.1 M TBAPF₆ in CH₃CN at 200 mV/s without acid (red) and in the presence of 1.6 mM TFA (blue) with i_c , $i_{1/2}$, and $E_{1/2}$ highlighted.

To calculate the overpotential of **4**, E_{ref} for 1 mM TFA in CH₃CN, which is given to be -0.33 V vs. SCE, can be subtracted from $E_{1/2}$ of **4** in the presence of 1 mM TFA, which is determined to be -0.81 V vs. SCE (Figure 2.17).¹² Therefore, the overpotential is calculated as such (Equation 2.2):

$$\begin{aligned} \text{Overpotential} &= |E_{1/2} - E_{ref}| \quad \text{(2.2)} \\ &= |(-0.81 \text{ V vs SCE}) - (-0.33 \text{ V vs SCE})| \\ &= 480 \text{ mV} \end{aligned}$$

Compared to **6**, which operates with an overpotential of 660 mV in acetonitrile, **4** operates at a lower overpotential, which indicates higher catalytic efficiency. This decrease in overpotential is a consequence resulting from modification of the catalyst's electronic properties through the addition of the naphthalenyl group. The mild electronic-withdrawing properties of this group may facilitate reduction of the metal and lead to a lower overpotential. While **4** operates with a modest overpotential, values as low as 300 mV for homogeneous iron complexes and below 250 mV for cobalt complexes have been reported.¹³ Heterogeneous systems incorporating Pt-loaded CNTs for electrocatalytic hydrogen generation have reported overpotentials less than 50 mV; however, reliance on a noble metal limits their widescale expansion and practicality.¹⁴ Though these systems are more efficient, **4** remains the first known iron-based heterogeneous electrocatalyst for proton reduction that utilizes pi-stacking to adhere to carbon surfaces.

Electrocatalytic Proton Reduction: Tonic and Acetic Acid Additions

In addition to TFA, tonic and acetic acid were tested as proton sources for hydrogen generation catalyzed by **4**. Of the three, tonic acid is by far the strongest, as it has a pK_a of 8.3 in CH_3CN compared to 12.7 and 22.3 for that of TFA and acetic acid respectively.¹² The nitro-functionalized complex **7** has previously been demonstrated to be active upon the addition of tonic acid, so it was of interest to examine the behavior of **4** under similar conditions as well.⁵ In the presence of 0.4 mM tonic acid, an irreversible catalytic wave corresponding to proton reduction is observed at -1.03 V vs. SCE (Figure 2.18). The magnitude of this peak is larger than what is seen in the 0.4 mM TFA addition, and this is likely attributed to the difference in each acid's strength. However, in contrast to the TFA additions, the area of the proton reduction peak decreases with increasing tonic acid concentrations. In the presence of 4.0 mM tonic acid, no proton reduction activity is observed at all. Since **7** has shown to be active in the presence of tonic acid and has the same core structure, desorption, rather than degradation, of **4** from the electrode surface is the most probable cause of diminishing catalytic activity at higher concentrations of tonic acid.

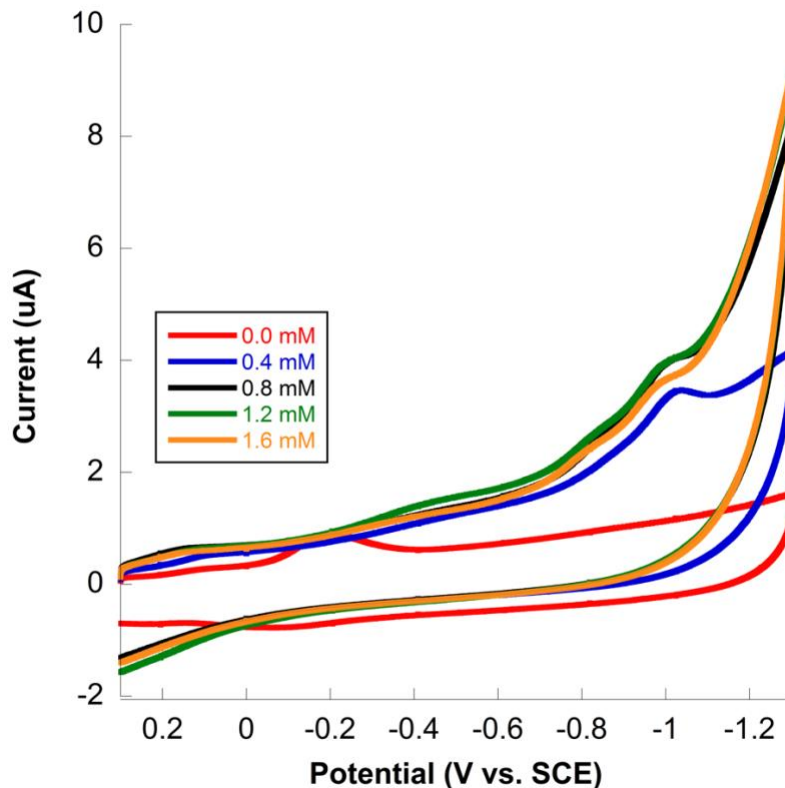


Figure 2.18. Cyclic voltammograms of surface-adsorbed **4** in 5 mL of 0.1 M TBAPF₆ in CH₃CN at 200 mV/s without acid (red) and in the presence of increased concentrations of tosic acid. A catalytic reduction is visible at -1.03 V vs. SCE.

Since the relatively high strength of tosic acid leads to desorption, it is of interest to examine how **4** behaves in the presence of acids weaker than both tosic and TFA. To that end, acetic acid was selected as a proton source due to its low background reduction within the catalytic potential window being examined. However, upon addition of acetic acid, there is no clear reduction event corresponding to hydrogen generation (Figure 2.19). The E_{ref} for acetic acid is -0.91 V vs. SCE, so a catalytic wave is expected around -1.4 V after taking into account the overpotential of **4**.¹² In addition to lack of proton reduction capacity of this system, the Fe(III)/Fe(II) redox couple does not shift to a more

positive potential upon acetic acid addition. This indicates that acetic acid is not strong enough to protonate the phenol, which is an essential step in the catalytic cycle. When the behavior of **6** was tested upon incorporation of acetic acid, no shift in the Fe(III)/Fe(II) redox couple and no proton reduction activity was observed (Figure A.7). This indicates that lack of catalytic activity in the presence of acetic acid is characteristic to this class of iron polypyridyl complexes rather than being specific to just the naphthalene-functionalized heterogeneous complex.

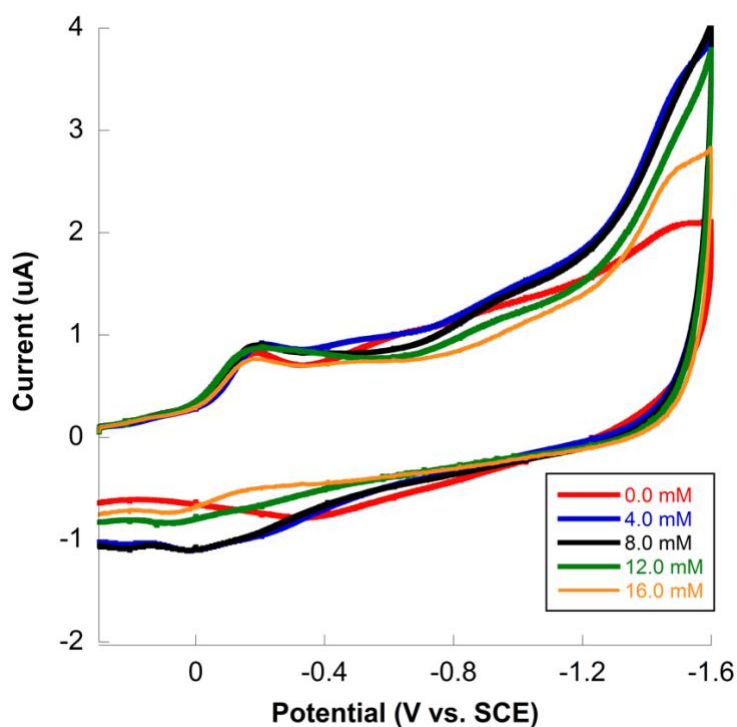


Figure 2.19. Cyclic voltammograms of surface-adsorbed **4** in 5 mL of 0.1 M TBAPF₆ in CH₃CN at 200 mV/s without acid (red) and in the presence of increased concentrations of acetic acid.

Electrocatalytic Proton Reduction: Activity in Aqueous Buffer Solutions

Since an ideal proton reduction catalyst for incorporation into an AP system should be active in aqueous environments, it is of interest to examine the behavior of **4** in aqueous solutions. On that account, the catalytic activity of **4** was examined in aqueous citrate-phosphate buffer solutions with a pH range of 3.8 – 6.2. Catalytic reduction waves were observed in each scan, with the proton reduction current increasing with decreasing pH (Figure 2.20). While proton reduction activity in these aqueous buffer solutions is evident, stability in these buffer solutions was time-restricted; if the electrode saturated with surface-adsorbed **4** is immersed in these buffer solutions for >15 minutes, desorption from the surface occurs, resulting in no catalytic activity. As such, cyclic voltammograms were obtained 2 minutes after the addition of the glassy carbon working electrode.

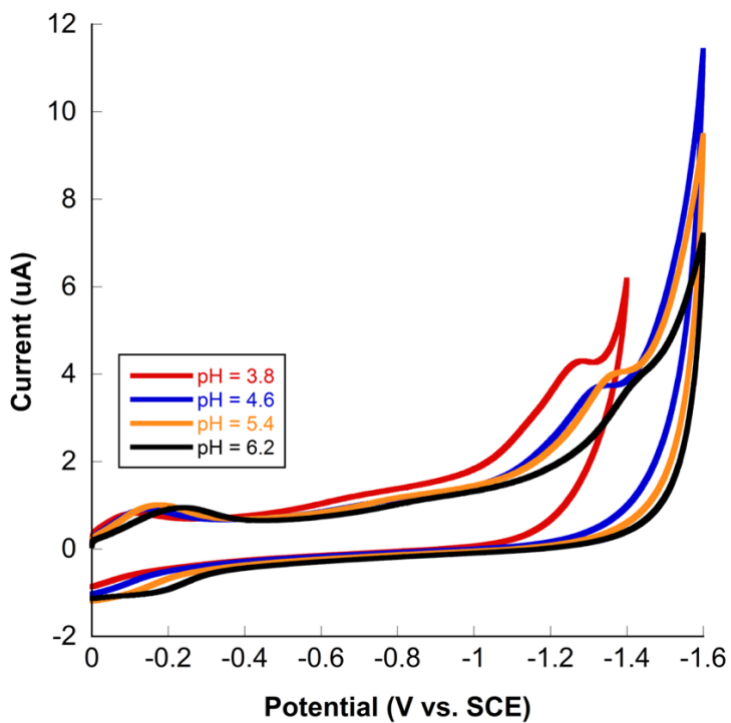


Figure 2.20. Cyclic voltammograms of surface-adsorbed **4** in 5 mL aqueous citrate-phosphate buffer solutions (pH = 3.8 – 6.2) at 100 mV/s from 0.0 to -1.4 V at pH = 3.8 and from 0.0 to -1.6 V at pH = 4.6 – 6.2.

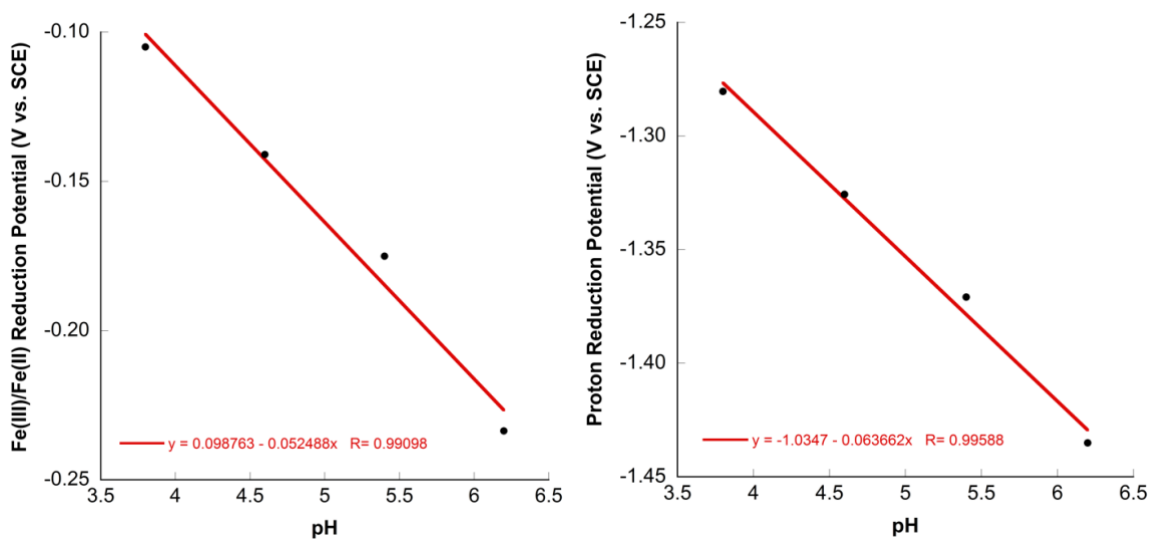


Figure 2.21. *Left:* Linear relationship ($R^2 = 0.991$) between Fe(III)/Fe(II) reduction potential and pH. *Right:* Linear relationship ($R^2 = 0.996$) between catalytic proton reduction wave potential and pH.

Results from the buffer study show that the potential at which the Fe(III)/Fe(II) reduction and the proton reduction events occur vary with pH (Figure 2.21). Based on each regression equation, variation of 52 and 64 mV per pH unit are seen respectively. This behavior can be investigated with the Nernst Equation, which relates the reduction potential of an electrochemical reaction to the standard electrode potential, temperature, and concentrations of the chemical species undergoing reduction and oxidation (Equation 2.3):

$$E_{cell} = E_{cell}^{\circ} - \frac{RT}{nF} \ln (Q_r) \quad (2.3)$$

where E_{cell}° is the standard cell potential, R is the universal gas constant, T is the temperature, n is the number of electrons transferred in the cell reaction or half-reaction, and Q_r is the reaction quotient.¹⁵ Converting from natural log to base-10 logarithms and assuming a temperature of 298 K, variation in the reaction potential can be given by:

$$- \frac{0.0591 V}{n} \log (Q_r)$$

Simplifying further, Q_r is 10 for one change in pH unit, making $\log (Q_r)$ one, which results in:

$$- \frac{0.0591 V}{n}$$

This expression gives the expected variation in cell potential per pH unit as a function of the number of electrons transferred. Based on this relationship, -59 and -30 mV change per pH unit is expected for one- and two-electron reduction events respectively. Since variation of -52 and -64 mV per pH unit are

experimentally observed for the Fe(III)/Fe(II) reduction and catalytic proton reduction events respectively, both are confirmed to be one-electron events.

Proposed Mechanism

Based on the cyclic voltammograms gathered for the acetic, tosic, and TFA additions and the analysis of the Nernst equation, it is possible to assemble a mechanism for the catalytic hydrogen production by **4**. In the absence of acid, the Fe(III)/Fe(II) redox couple occurs at -0.20 V vs. SCE. Upon the addition of an appropriate acid, such as tosic or TFA, the redox shifts about 240 – 340 mV more positively. This shift implies a chemical change, most likely protonation of the phenol, to the catalyst. Without this protonation step, the catalyst is not active for proton reduction, and this behavior is observed when using acetic acid, which is not strong enough to protonate the catalyst. Once protonated, the catalyst undergoes subsequent electrochemical reduction and protonation steps (Figure 2.22). Since the reduction potential of the protonated complex **4** matches that of the protonated parent complex **6** and its nitro-derivative **7**, protonation may result in the phenol group becoming hemilabile. This would leave the Fe-NNN core intact and explain why each protonated complex is reduced at the same potential. Later in the mechanism, the phenol group likely recoordinates to the iron center, which would account for differences in the proton reduction potential between each iron polypyridyl complex.

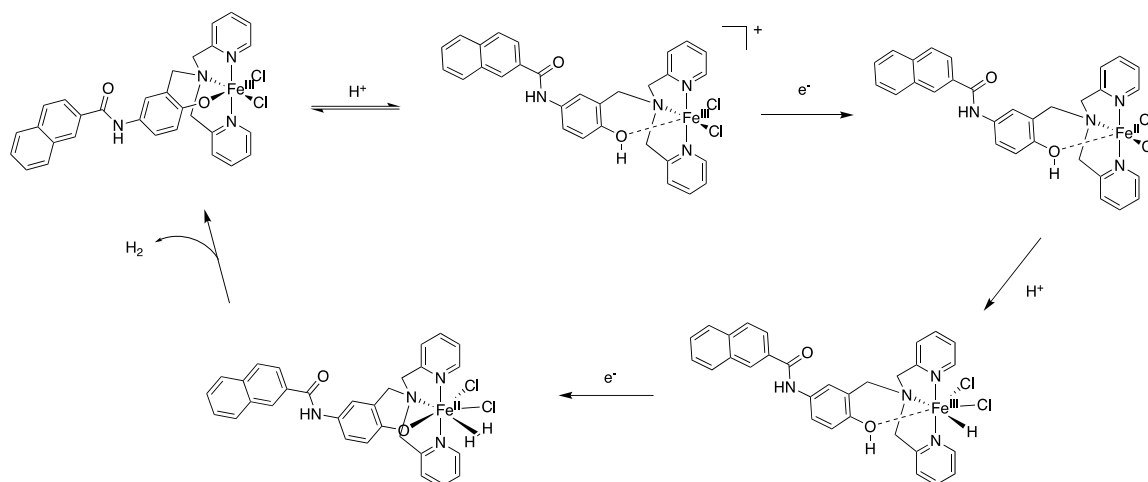


Figure 2.22. Proposed CECE mechanism for proton reduction by **4**.

Conclusion

The work reported focuses on the characterization, adsorption behavior, and electrocatalytic abilities of a naphthalene-terminated iron polypyridyl complex for the functionalization of carbon surfaces. The naphthalene functionality of **4** allows for its successful adsorption onto carbon surfaces in the form of a glassy carbon electrode via pi-stacking interactions. Adsorption is indicated by a linear relationship between i_{cp} and the potential sweep rate in addition to a vastly smaller ΔE_p than that of the parent complex **6**. Electrode-surface adsorption saturation is reached after 720 minutes with a maximum surface coverage of $7.7 \cdot 10^{-11}$ mol/cm². The complex is relatively surface-stable in solvents lacking hydrogen-bond donors or acceptors.

Additionally, electrocatalytic proton reduction is achievable using **4**; upon addition of TFA, an irreversible catalytic wave corresponding to proton reduction is observed at -1.13 V vs. SCE, and higher concentrations of acid lead to enhancement of this wave. The complex operates with an overpotential of 480

mV in acetonitrile, which is lower than that of the unfunctionalized parent catalyst **6**. A shift in the Fe(III)/Fe(II) redox couple, which is observed in TFA and tosic acid additions, suggests protonation of the phenolate is an essential step in the catalytic cycle. Acetic acid is not strong enough to protonate the complex, resulting in no shift in the Fe(III)/Fe(II) redox couple and an absence of an irreversible proton reduction peak. On the contrary, acids that are too strong, such as tosic, result in the instability of **4** on the electrode surface and lead to desorption. **4** was also successful at reducing protons in aqueous citrate-phosphate buffer systems of pH = 3.8 – 6.2. Proton reduction catalysis becomes more favorable as the pH decreases. The successful functionalization of carbon surfaces and electrocatalytic proton reduction capacities of **4** show significant promise for its incorporation into a heterogeneous AP system for photocatalytic hydrogen generation.

References

1. Yakout, S. M.; Daifullah, A. A. M.; El-Reefy, S. A. Adsorption of Naphthalene, Phenanthrene and Pyrene from Aqueous Solution Using Low-Cost Activated Carbon Derived from Agricultural Wastes. *Adsorption Science and Technology*. **2013**, 31 (4), 293-302.
2. Kim, K. T.; Jo, W. H. Non-destructive functionalization of multi-walled carbon nanotubes with naphthalene-containing polymer for high performance Nylon66/multi-walled carbon nanotube composites. *Carbon*. **2011**, 49 (3), 819-826.
3. Smith, H. L.; Usala, R. L.; McQueen, E. W.; Goldsmith, J. I. Novel Polyaromatic-Terminated Transition Metal Complexes for the Functionalization of Carbon Surfaces. *Langmuir*. **2010**, 26 (5), 3342-3349.
4. Harris, P. J. F. Fullerene-related structure of commercial glassy carbons. *Philos. Mag.* **2004**, 84 (29), 3159-3167.
5. Hartley, C. L.; DiRisio, R. J.; Screen, M. E.; Mayer, K. J.; McNamara, W. R. Iron polypyridyl complexes for photocatalytic hydrogen generation. *Inorg. Chem.* **2016**, 55, 8865-8870.
6. Zhang, W. Dye-Sensitized TiO₂ Modified with Iron Polypyridyl Catalyst for Photocatalytic Hydrogen Evolution. *Master's Thesis, College of William and Mary*. **2016**.
7. Race, N. A.; Zhang, W.; Screen, M. E.; Barden, B. A.; McNamara, W. R. Iron polypyridyl catalysts assembled on metal oxide semiconductors for photocatalytic hydrogen generation. *Chem. Comm.* **2018**, 54, 3290-3293.
8. Elgrishi, N.; Rountree, K.; McCarthy, B.; Rountree, E.; Eisenhart, T.; Dempsey, J. A practical beginner's guide to cyclic voltammetry. *J. Chem. Edu.* **2018**, 95 (2), 197-206.
9. Bard, A. J.; Faulkner, L. R. *Electrochemical Methods, 2nd ed.* J. Wiley & Sons: New York, **2001**; Chapter 14.
10. Connor, G. P.; Mayer, K. J.; Tribble, C. S.; McNamara, W. R. Hydrogen evolution catalyzed by an iron polypyridyl complex in aqueous solutions. *Inorg. Chem.* **2014**, 53, 5408-5410.
11. Kütt, A.; Leito, I.; Kaljurand, I.; Sooväli, L.; Vlasov, V.; Yagupolskii, L.; Koppel, I. A comprehensive self-consistent spectrophotometric acidity scale of neutral Brønsted acids in acetonitrile. *J. Org. Chem.* **2006**, 71 (7), 2829-2838.
12. Fourmond, V.; Jacques, P.; Fontecave, M.; Artero, V. H₂ Evolution and Molecular Electrocatalysts: Determination of Overpotentials and Effect of Homoconjugation. *Inorg. Chem.* **2010**, 49, 10338-10347.
13. (a) McKone J. R.; Marinescu S. C.; Brunschwig B. S.; Winkler J. R.; Gray H. B. Earth-abundant hydrogen evolution electrocatalysts. *Chem. Sci.*

- 2014**, 5, 865-878. (b) McCrory C.; Uyeda C.; Peters J. C. Electrocatalytic Hydrogen Evolution in Acidic Water with Molecular Cobalt Tetraazamacrocycles. *J. Am. Chem. Soc.* **2012**, 134, 3164-3170.
14. Bhalothia, D.; Krishnia, L.; Yang, S.; Yan, C.; Hsiung, W.; Wang, K.; Chen, T. Recent advancements and future prospects of noble metal-based heterogenous nanaocatalysts for oxygen reduction and hydrogen evolution reactions. *Appl. Sci.* **2020**, 10, 7708.
15. Vidal-Iglesias, F. J.; Solla-Gullon, J.; Rodes, A.; Herrero, E.; Aldaz, A. Understanding the Nernst Equation and Other Electrochemical Concepts: An Easy Experimental Approach for Students. *J. Chem. Educ.* **2012**, 89 (7), 936-939.

Appendix A

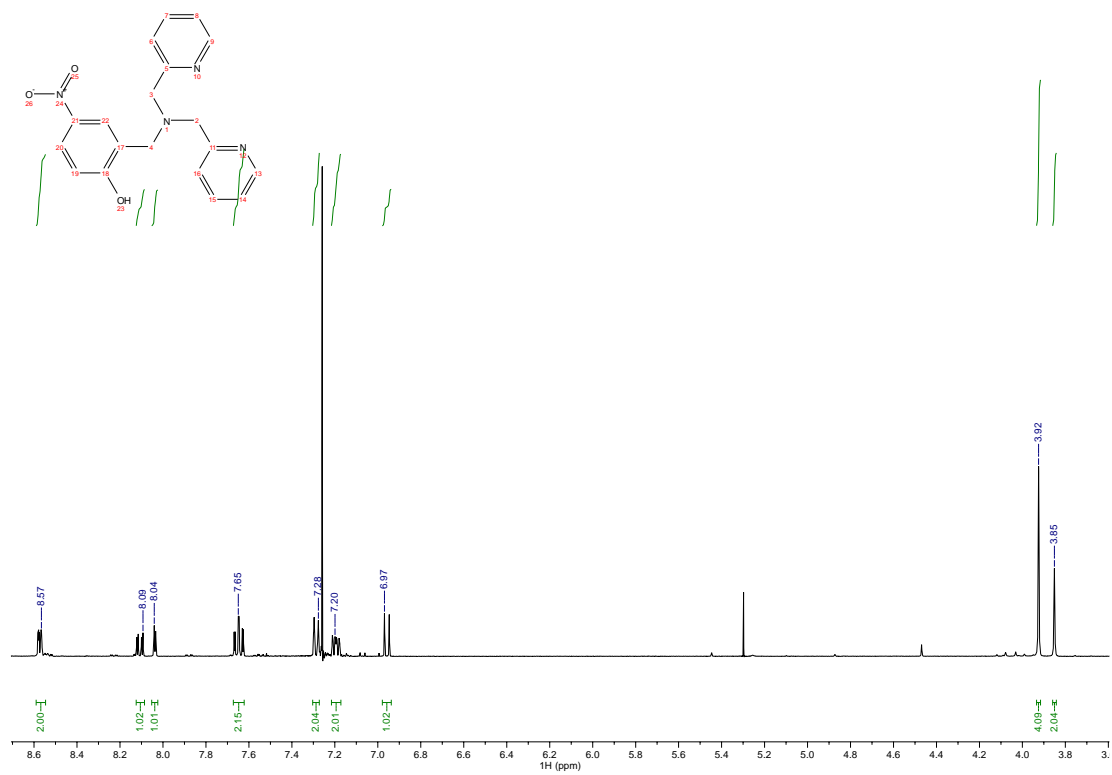


Figure A.1. ^1H NMR spectrum of **1** with integrals in green.

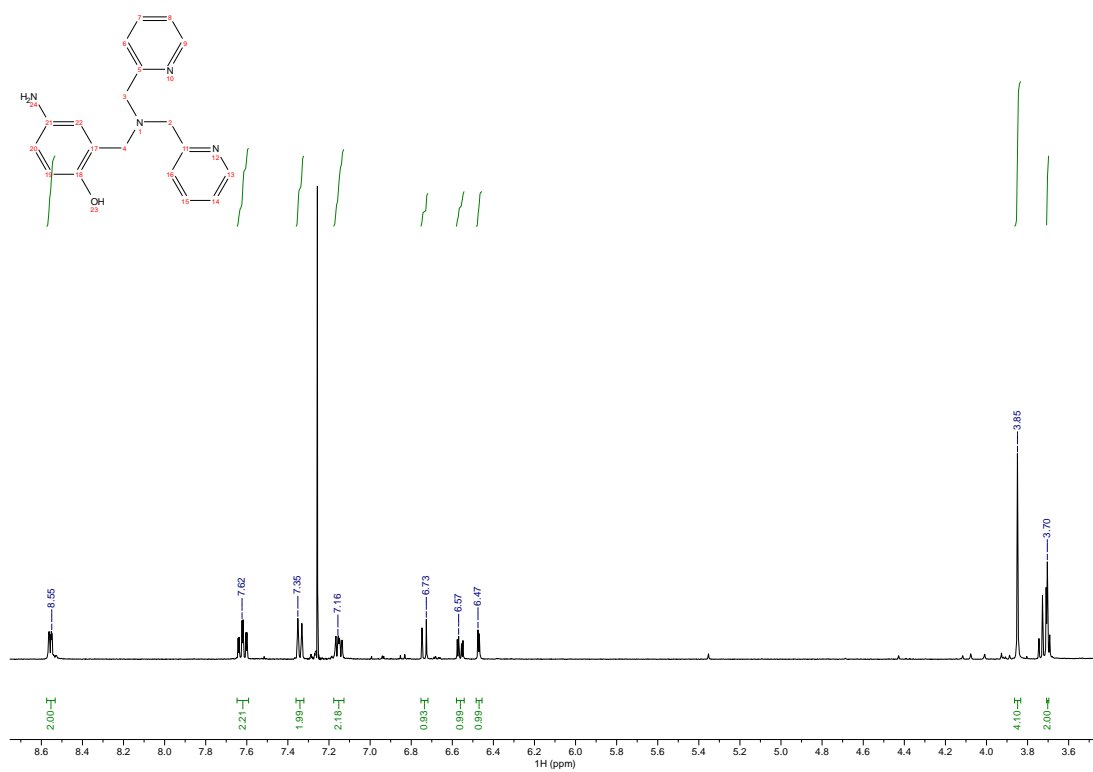


Figure A.2. ¹H NMR spectrum of **2** with integrals in green. The quartet at 3.73 ppm corresponds to residual ethanol.

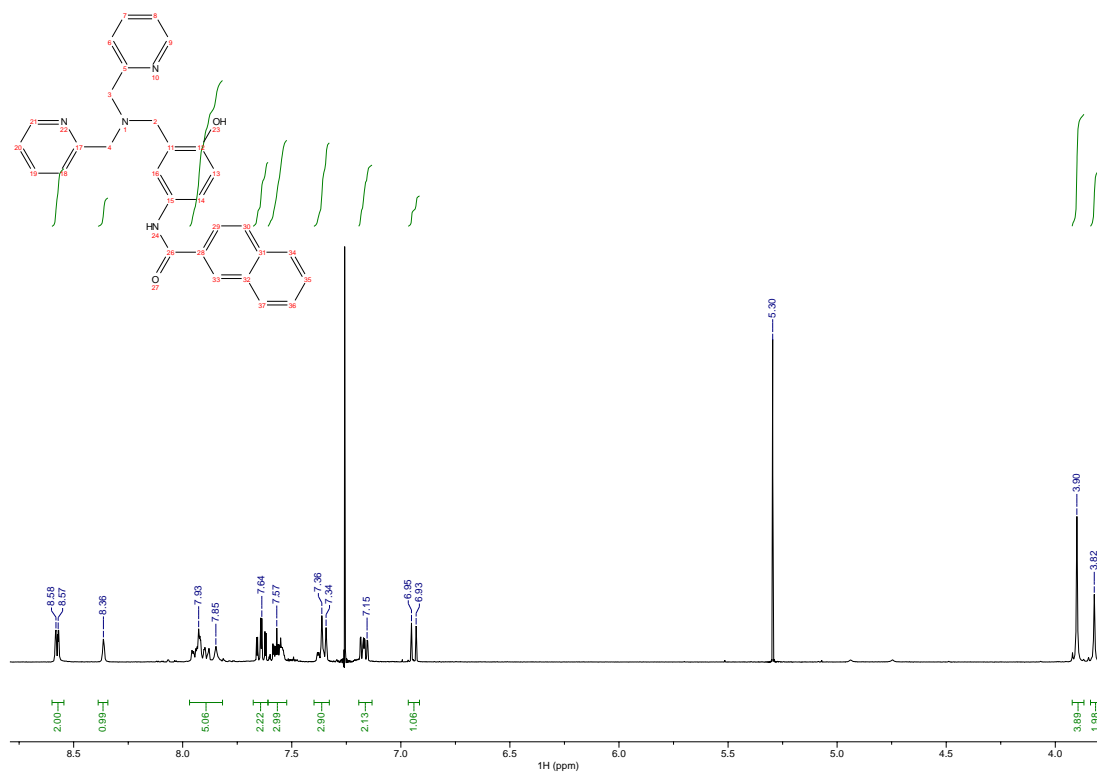


Figure A.3. ¹H NMR spectrum of **3** with integrals in green.

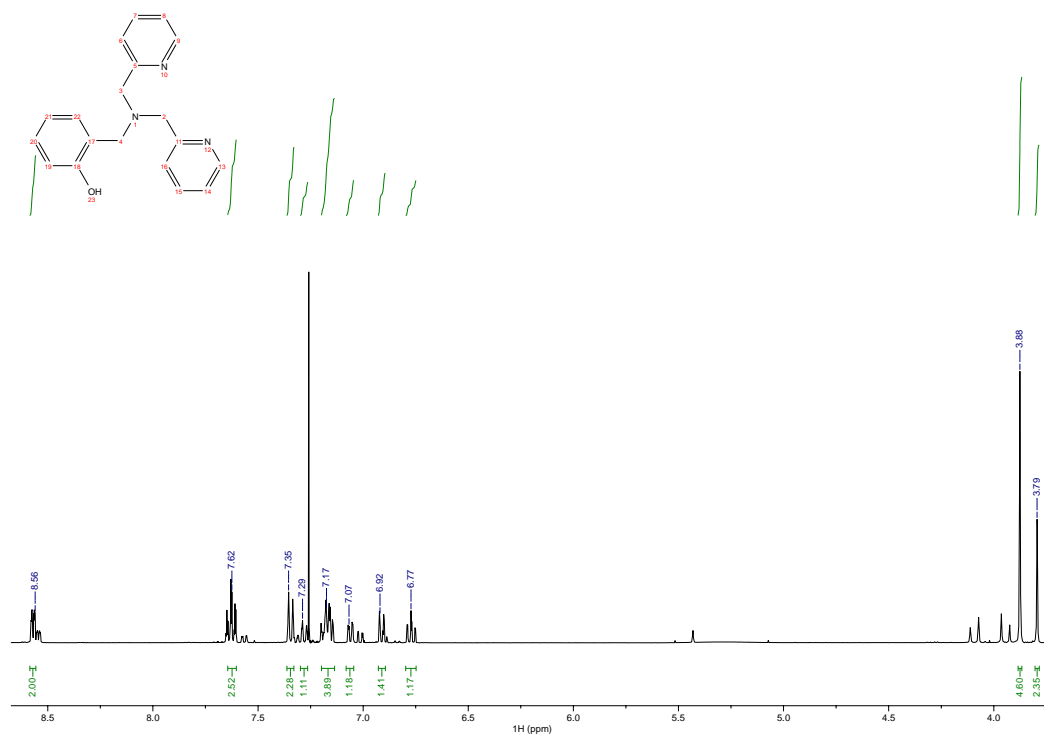


Figure A.4. ^1H NMR spectrum of **5** with integrals in green.

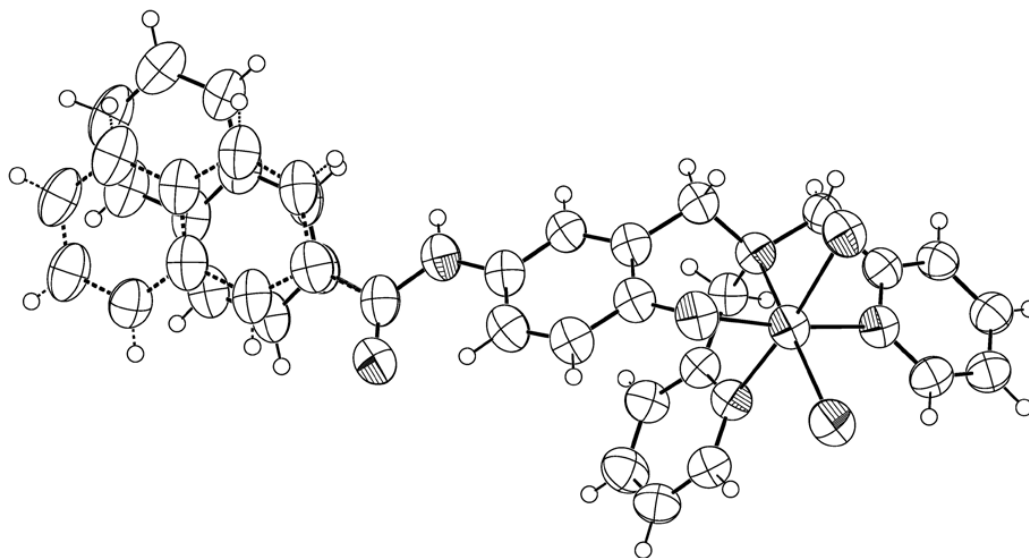


Figure A.5. ORTEP diagram of **4** with disorder visible in the naphthalenyl group.

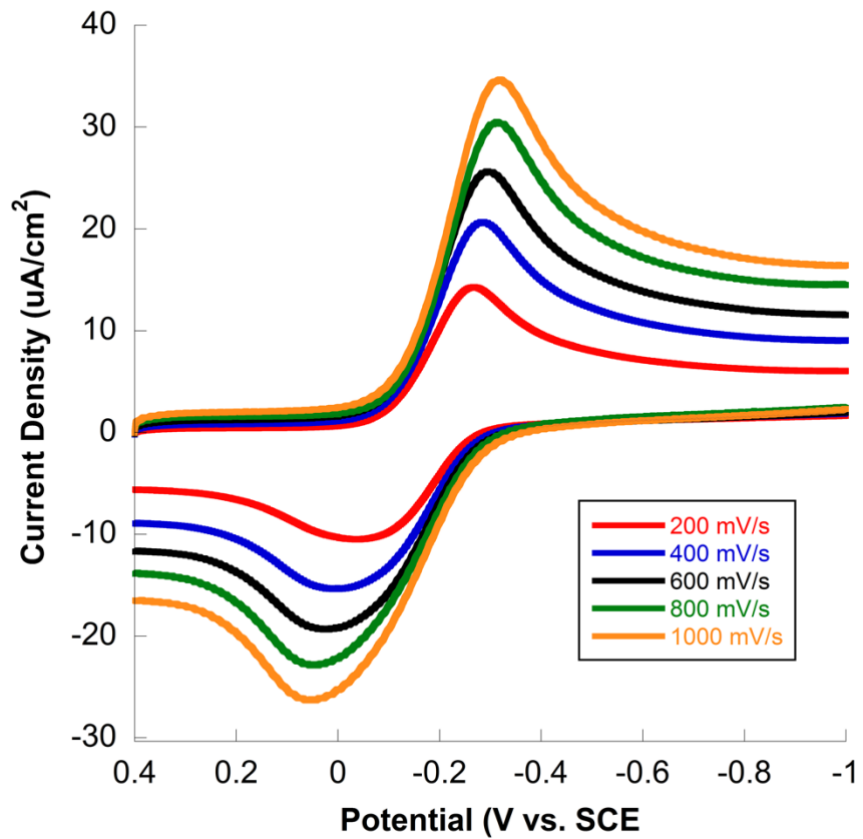


Figure A.6. Cyclic voltammograms of 0.1 mg **6** in 5 mL of CH₃CN with 0.1 M TBAPF₆ at various scan rates.

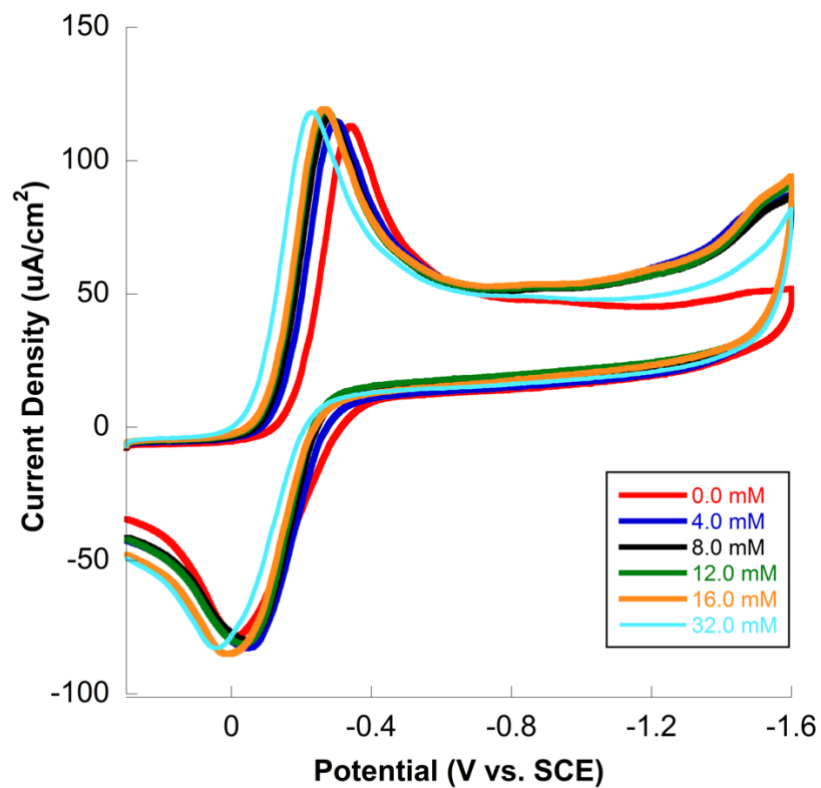


Figure A.7. Cyclic voltammograms of 0.8 mg **6** in CH₃CN with 0.1 M TBAPF₆ at 200 mV/s without acid (red) and in the presence of increased concentrations of acetic acid.

Table A.1. Crystal data and structure refinement for **4**.

Empirical formula	C30 H25 Cl2 Fe N4 O2
Formula weight	600.29
Temperature	99.98(10) K
Wavelength	1.54184 Å
Crystal system	orthorhombic
Space group	<i>Pbca</i>
Unit cell dimensions	$a = 11.4056(2)$ Å $b = 22.8180(4)$ Å $c = 25.3841(5)$ Å
Volume	6606.3(2) Å ³
Z	8
Density (calculated)	1.207 Mg/m ³
Absorption coefficient	5.388 mm ⁻¹
<i>F</i> (000)	2472
Crystal color, morphology	blue, plate
Crystal size	0.19 x 0.102 x 0.028 mm ³
Theta range for data collection	3.482 to 78.003°
Index ranges	-14 ≤ <i>h</i> ≤ 13, -28 ≤ <i>k</i> ≤ 25, -30 ≤ <i>l</i> ≤ 32
Reflections collected	41178
Independent reflections	6941 [<i>R</i> (int) = 0.0590]
Observed reflections	5181
Completeness to theta = 74.504°	99.7%
Absorption correction	Multi-scan
Max. and min. transmission	1.00000 and 0.35954
Refinement method	Full-matrix least-squares on <i>F</i> ²
Data / restraints / parameters	6941 / 250 / 447
Goodness-of-fit on <i>F</i> ²	1.049
Final <i>R</i> indices [<i>I</i> > 2σ(<i>I</i>)]	<i>R</i> 1 = 0.0556, <i>wR</i> 2 = 0.1556
<i>R</i> indices (all data)	<i>R</i> 1 = 0.0724, <i>wR</i> 2 = 0.1695
Largest diff. peak and hole	0.768 and -0.692 e.Å ⁻³

Chapter 3: Preparation of a Pyrene-Terminated Iron Electrocatalyst and Future Directions

Introduction

Though the naphthalene-terminated complex was successfully able to functionalize carbon surfaces, was electrocatalytically active for proton reduction, and exhibited sufficient stability in organic solvents, its major weakness lies within its rapid desorption in aqueous solutions. One method to address this issue and improve the strength of adsorption is to increase the size of the polyaromatic anchor, as highly correlated quantum mechanical calculations on the strengths of π - π -stacking interactions between aromatic molecules and CNTs suggest that binding energies are in the range of 10-25 kJ/mol per benzene ring.¹

As such, incorporation of pyrene functionality to the established polypyridyl ligand framework shows much promise, as its binding energy would be twice that of naphthalene based on its network size. Previous work focusing on the adsorption of both naphthalene and pyrene on activated carbon derivatives showed that, while adsorption kinetics are similar, the adsorption affinity of pyrene to the carbon surface was over twice as great than that of naphthalene.² Additionally, Goldsmith et al. found that, while both of their polyaromatic functionalized cobalt complexes were able to adsorb to the surfaces of glassy carbon electrodes, pyrene functionality provided enhanced-surface stability; whereas the naphthalene complex exhibited rapid desorption, the

pyrene complex demonstrated modest surface stability over a 2-hour period of continuous cycling. Quantitatively, this behavior is reflected in the free energy of adsorption, which was found to be -41 kJ/mol for $[\text{Co}(\text{tpy}\sim\text{py})_2]^{2+}$ and -30 kJ/mol for $[\text{Co}(\text{tpy}\sim\text{nap})_2]^{2+}$.¹ As such, incorporation of pyrene functionality shows much promise for enhancing carbon-surface stability.

Herein, this work presents the modification of the parent catalyst **[FeCl₂(L)]**, previously shown to be electrocatalytically and photocatalytically active in homogeneous systems, through the addition of a terminal pyrene group to enable functionalization of carbon surfaces (Figure 3.1). Multiple syntheses for pyrene incorporation into the polypyridyl ligand framework were explored. This includes amide bond formation between **L-NH₂** and different pyrene substrates in addition to carbon-nitrogen bond formation using a palladium-catalyzed cross coupling. ¹H and ¹³C NMR are used to assess the validity of each synthesized ligand. Following complexation of the pyrene-functionalized ligand to iron, cyclic voltammetry was used to assess the heterogeneous behavior and adsorption properties of the catalyst on a glassy carbon electrode surface.

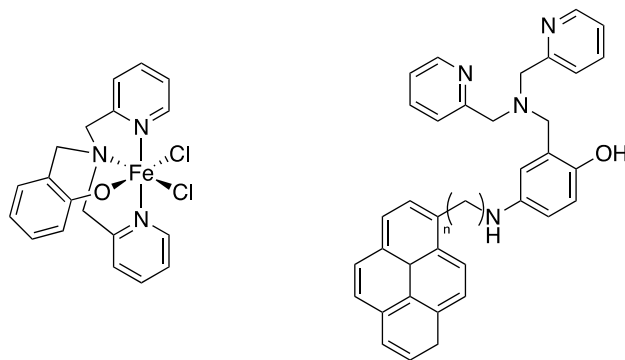


Figure 3.1. *Left:* Structure of iron polypyridyl parent complex **[FeCl₂(L)]** and *Right:* proposed structure for a pyrene-functionalized complex **[FeCl₂(L-Py)]**.

Experimental Procedure

Materials

All experiments were carried out using standard Schlenk techniques under an Ar atmosphere unless otherwise indicated. All reagents were purchased from Acros Organics, Alfa Aesar, Fisher Scientific, or TCL and were used without further purification.

Instrumentation

^1H and ^{13}C NMR spectra were recorded on an Agilent 400MR DD2 spectrometer operating in the pulse Fourier transform mode. Chemical shifts are reported in ppm and referenced to residual solvent.

Syntheses

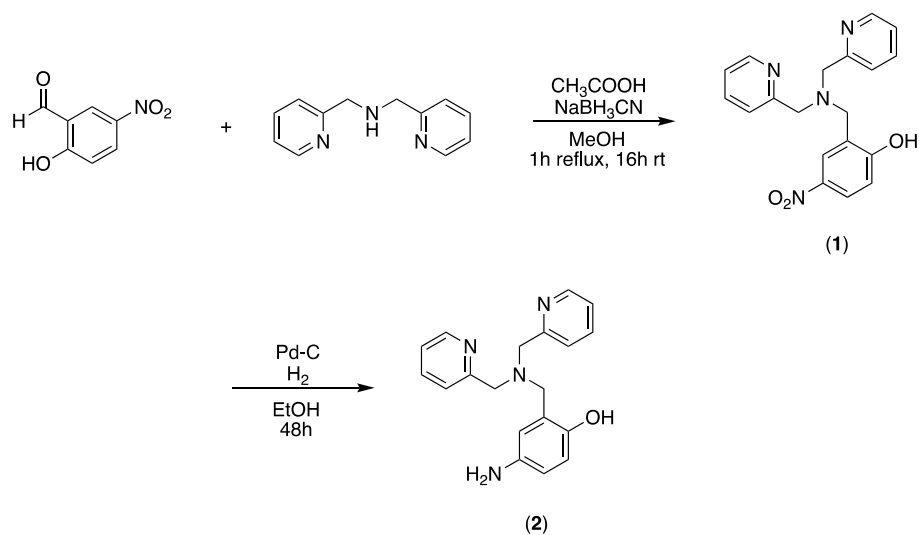


Figure 3.2. Synthesis of the amino-functionalized polypyridyl ligand (**L-NH₂**, **2**).

Synthesis of 2-((bis(pyridin-2-ylmethyl)amino)methyl)-4-nitrophenol (1, L-NO₂)

Compound **1** was synthesized using a modified literature procedure (Figure 3.2).³

To a solution of 2-hydroxy-5-nitrobenzaldehyde (3.34 g, 20 mmol) in 100 mL of MeOH was added bis(pyridine-2-ylmethyl)amine (3.6 mL, 20 mmol). Glacial acetic acid (3 drops) was added followed by a solution of sodium cyanoborohydride (0.62 g, 10 mmol) in 30 mL of MeOH. After refluxing for 1 hour, the solution was stirred at room temperature overnight. 1 M HCl was added to the resulting solution until it reached pH = 4. The red solution was evaporated to dryness, dissolved in 100 mL of saturated Na₂CO₃, and extracted with chloroform (3 x 100 mL). The organic layers were combined, dried with Na₂SO₄, and filtered through celite. The solvent was removed under vacuum to yield a red oil, which was purified using silica gel chromatography with 9:1 dichloromethane:methanol to give 1.80 g of **1** (62% yield). ¹H NMR (CDCl₃): δ 8.58 (m, 2H), 8.12 (d, 1H), 8.05 (d, 1H), 7.66 (td, 2H), 7.30 (d, 2H), 7.21 (t, 2H), 6.95 (d, 1H), 3.93 (s, 4H), 3.85 (s, 2H) (Figure B.1). ¹³C NMR (CDCl₃): δ 164.27, 157.71, 148.69, 139.68, 137.06, 126.54, 125.61, 123.52, 123.08, 122.41, 117.17, 58.67, 56.10.

Synthesis of 4-amino-2-((bis(pyridin-2-ylmethyl)amino)methyl)phenol (**2**, L-NH₂)

Compound **2** was synthesized using a literature procedure (Figure 3.2).⁴ To a solution of **1** (1 g, 2.86 mmol) in 180 mL EtOH, palladium on activated carbon (10% Pd) (0.1 g) was added. The reaction vessel was degassed, replenished with hydrogen gas, and allowed to stir at room temperature for 2 days. The brown solution was filtered through celite and evaporated to dryness to give 0.87 g of **2** (95 % yield). ¹H NMR (CDCl₃): 8.56 (m, 2H), 7.63 (td, 2H), 7.34 (d, 2H), 7.15 (m, 2H), 6.74 (d, 1H), 6.57 (dd, 1H), 6.48 (d, 1H), 3.85 (s, 4H), 3.71 (s, 2H) (Figure B.2).

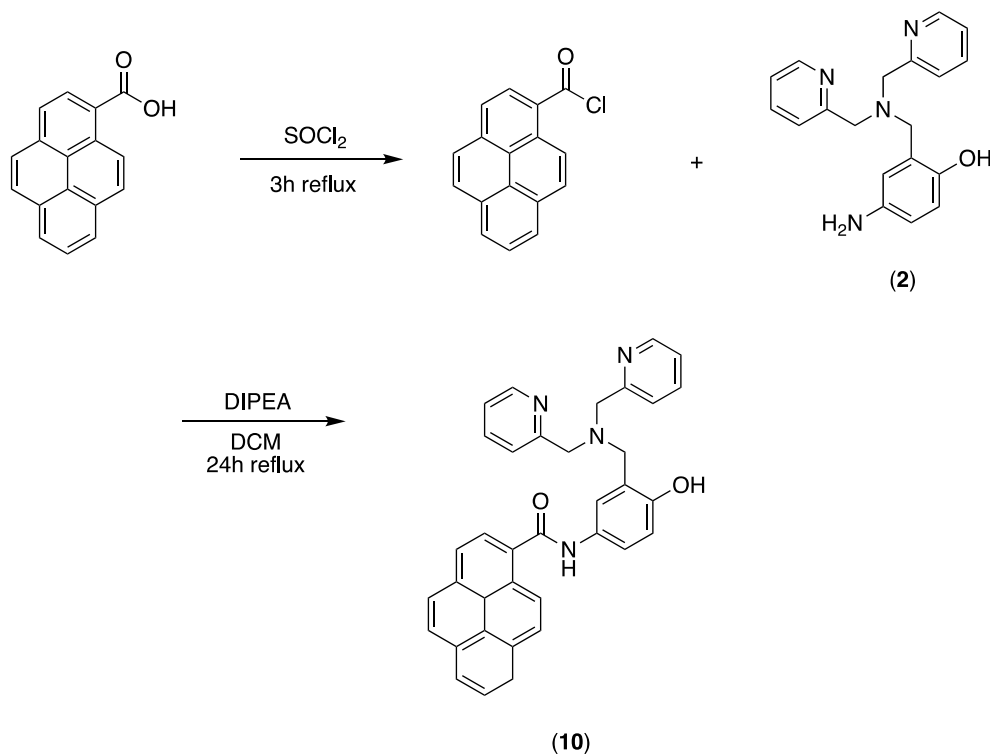


Figure 3.3. Method 1: Synthesis of the pyrene-functionalized polypyridyl ligand (L-Py1, **10**).

Synthesis of N-(3-((bis(pyridin-2-ylmethyl)amino)methyl)-4-hydroxyphenyl)-3a¹,8-dihydropyrene-1-carboxamide (L-Py1, 10)

This compound was synthesized using modified literature procedures (Figure 3.3).^{5,6} To an oven-dried flask containing 1-pyrenecarboxylic acid (0.20 g, 0.81 mmol) was added SOCl₂ (5.50 mL, 75.70 mmol). After refluxing for 3 hours, excess SOCl₂ was removed by liberally bubbling argon through the solution to leave behind 1-pyrenoyl chloride. A solution containing **L-NH₂** (0.26 g, 0.81 mmol) and DIPEA (0.15 mL, 0.81 mmol) in 20 mL of anhydrous DCM was added. The solution was refluxed for 24 hours before being diluted with 30 mL H₂O and extracted with DCM (3 x 30 mL). The organic layers were combined and washed with a saturated NaHCO₃ solution (3 x 30 mL). The organic layer was collected, dried with MgSO₄, and filtered. The volatiles were removed to yield a viscous brown oil. Many purification methods were attempted, including using silica gel chromatography with 9:1 dichloromethane:methanol, 19:1 dichloromethane:methanol, and 97:3 chloroform:methanol. Additionally, the crude was dissolved in DCM and was allowed to sit for 2 days, resulting in the accumulation of a yellow solid on the solution surface, which was filtered off. Crystallization in hot pentane was also attempted, though was unsuccessful.

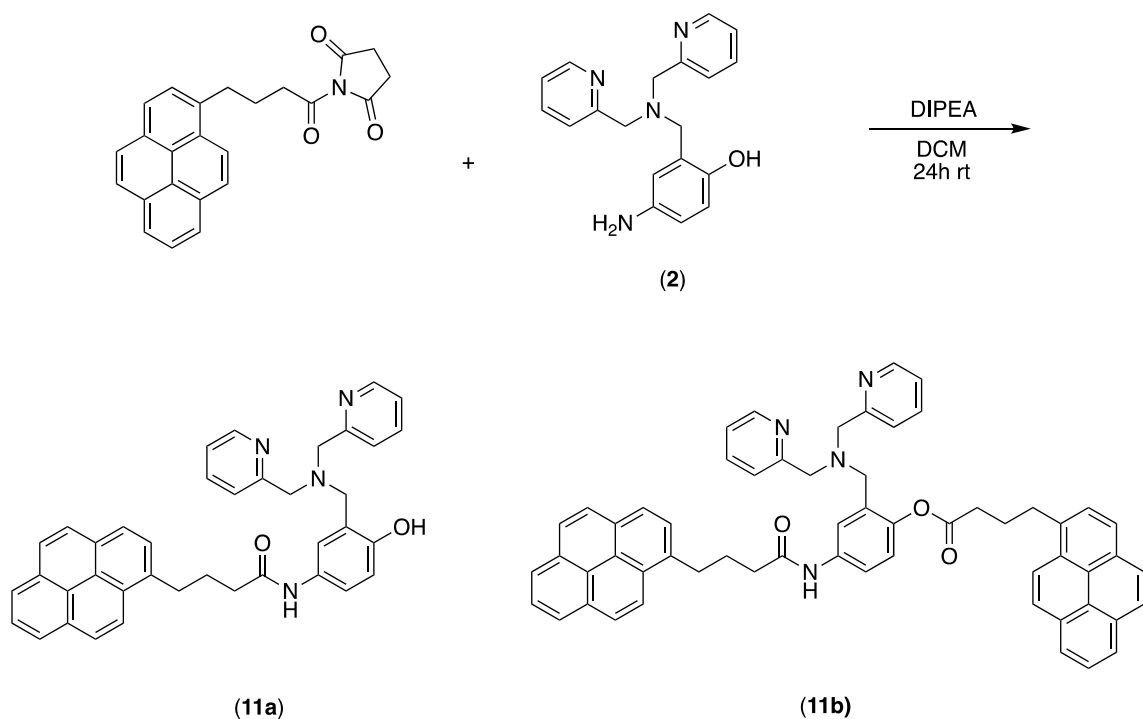


Figure 3.4. Method 2: Synthesis of the pyrene-functionalized polypyridyl ligand and byproduct (**L-Py2a**, **11a** + **L-Py2b**, **11b**).

Synthesis of 11a and 11b

This compound was synthesized using a modified literature procedure (Figure 3.4).¹ To a flask containing **L-NH₂** (0.37 g, 1.17 mmol) dissolved in 12 mL DCM was added a solution containing 1-pyrenebutyric acid n-hydroxysuccinimide ester (0.45 g, 1.17 mmol) and DIPEA (0.20 mL, 1.17 mmol) in 12 mL DCM. The solution was stirred overnight at room temperature. The clear brown solution was diluted with 100 mL H₂O and extracted with DCM (3 x 100 mL). The organic layers were combined and washed with a saturated NaHCO₃ solution (3 x 100 mL). The organic layer was collected, dried with MgSO₄, and filtered. The volatiles were removed to yield a viscous brown oil, which was purified using silica gel chromatography with 9:1 dichloromethane:methanol followed by a

second column run with 19:1 dichloromethane:methanol to give 0.07 g of **11b** product (7% yield). **11a** was unable to be identified or isolated. ^1H NMR (CDCl_3): δ 8.56 (m, 2H), 8.29 (d, 2H), 8.14 (dd, 3H), 8.09 (m, 3H), 8.01 (m, 5H), 7.86 (dd, 1H), (td, 7.60), 7.31 (d, 2H), 7.27 (d, 1H), 7.14 (m, 3H), 7.00 (s, 1H), 6.84 (d, 1H), 3.85 (s, 4H), 3.72 (s, 2H), 3.42 (m, 4H), 2.50 (t, 2H), 2.29 (m, 6H) (Figure B.3). ^{13}C NMR (CDCl_3): δ 170.59, 158.07, 154.40, 148.73, 136.91, 135.74, 131.39, 130.88, 129.95, 129.23, 128.81, 128.73, 127.46, 127.41, 127.35, 126.71, 126.68, 125.84, 125.81, 125.07, 124.97, 124.90, 124.88, 124.80, 124.78, 124.74, 123.38, 123.33, 123.29, 123.03, 122.70, 122.28, 121.36, 116.68, 58.91, 56.81, 36.65, 33.61, 32.76, 32.60, 27.25, 26.75 (Figure B. 4).

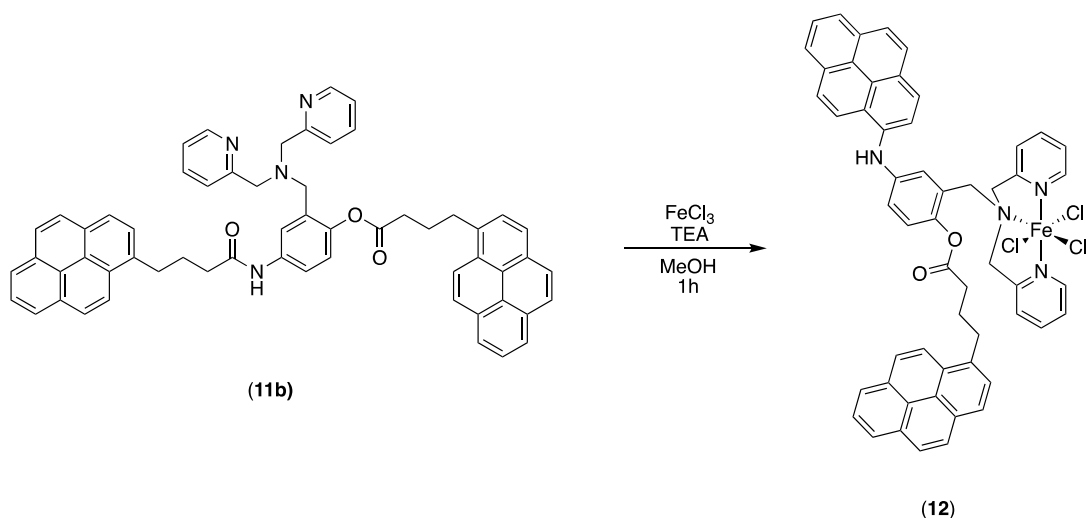


Figure 3.5. Synthesis of the bi-pyrene-functionalized iron polypyridyl complex ($[\text{FeCl}_2(\text{L-Py2b})]$, **12**).

Synthesis of $[\text{FeCl}_2(\text{L-Py2b})]$

Compound **12** was synthesized using a modified literature procedure (Figure 3.5).³ To a solution of **11b** (0.07 g, 0.08 mmol) and triethyl amine (0.01 mL, 0.08

mmol) in 5 mL MeOH was added a solution of $\text{FeCl}_3 \cdot 6\text{H}_2\text{O}$ (0.02 g, 0.08 mmol) in 5 mL MeOH. The solution immediately turned green with a visible precipitate. The reaction was stirred at room temperature for 1 hour and filtered. The solid was collected and washed with cold MeOH (3 x 5 mL). Crystallization, though unsuccessful, of the product was attempted by diffusion of diethyl ether into a concentrated solution of **12** in DCM.

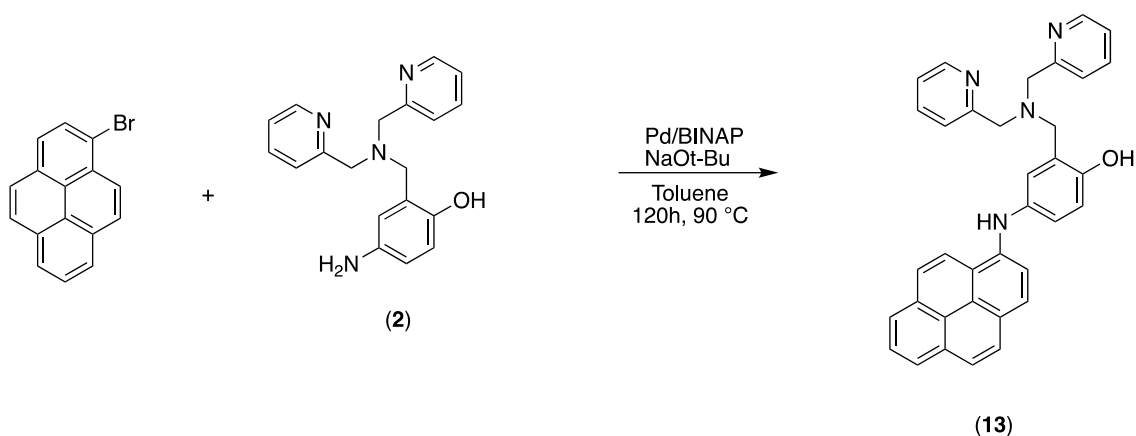


Figure 3.6. Synthesis of pyrene-functionalized iron polypyridyl complex (**L-Py3**, **13**).

Synthesis of 2-((bis(pyridin-2-ylmethyl)amino)methyl)-4-(pyren-1-ylamino)phenol (**L-Py3**, **13**)

Compound **13** was synthesized using a modified literature procedure (Scheme 3.6).⁷ An oven-dried Schlenk flask was purged with argon followed by the addition of (\pm)-BINAP (0.0094 g, 0.015 mmol). The flask was quickly sealed with a rubber septum and purged with argon before 1 mL of toluene was added. The mixture was heated to 90°C and stirred until BINAP dissolved. The solution was cooled to room temperature, the septum was removed, and $\text{Pd}(\text{OAc})_2$ (0.0045 g,

0.020 mmol, 1 mol%) was added. The flask was resealed, purged with argon, and allowed to stir for ~1 minute. The septum was removed, and **L-NH₂** (0.6660 g, 2.08 mmol), 1-bromopyrene (0.5351 g, 1.89 mmol), and NaOt-Bu (0.3814 g, 3.97 mmol) were added. The flask was resealed, and ~10 mL toluene was added to rinse down the sides of the flask and ensure all reagents were dissolved. The contents were purged with argon, and the reaction was stirred at 90°C for 5 days. The viscous green-brown solution was dissolved in DCM and transferred to a round bottom. The volatiles were removed, and the contents were passed through a short alumina column with DCM followed by 19:1 DCM:MeOH to remove the Pd catalyst. The eluant was evaporated to dryness to give a thick brown oil, which was purified using silica gel chromatography with 9:1 dichloromethane:methanol to give 0.285 g of **12** (29% yield). ¹H NMR (CDCl₃): δ 8.58 (m, 2H), 8.12 (d, 1H), 8.05 (t, 2H), 8.00 (m, 2H), 7.93 (m, 2H), 7.87 (d, 1H), 7.68 (d, 1H), 7.62 (td, 2H), 7.36 (d, 2H), 7.17 (qt, 2H), 7.07 (dd, 1 H), 6.97 (d, 1H), 6.93 (d, 1H), 6.22 (s, 1H), 3.90 (s, 4H), 3.77 (s, 2H) (Figure B.5). ¹³C NMR (CDCl₃): δ 158.11, 153.36, 148.84, 139.60, 136.91, 134.88, 132.05, 131.58, 127.54, 126.43, 126.09, 125.98, 125.83, 125.44, 125.30, 124.39, 124.28, 123.78, 123.74, 123.32, 123.02, 122.31, 122.02, 120.50, 119.81, 117.43, 114.85, 59.02, 56.84 (Figure B.6).

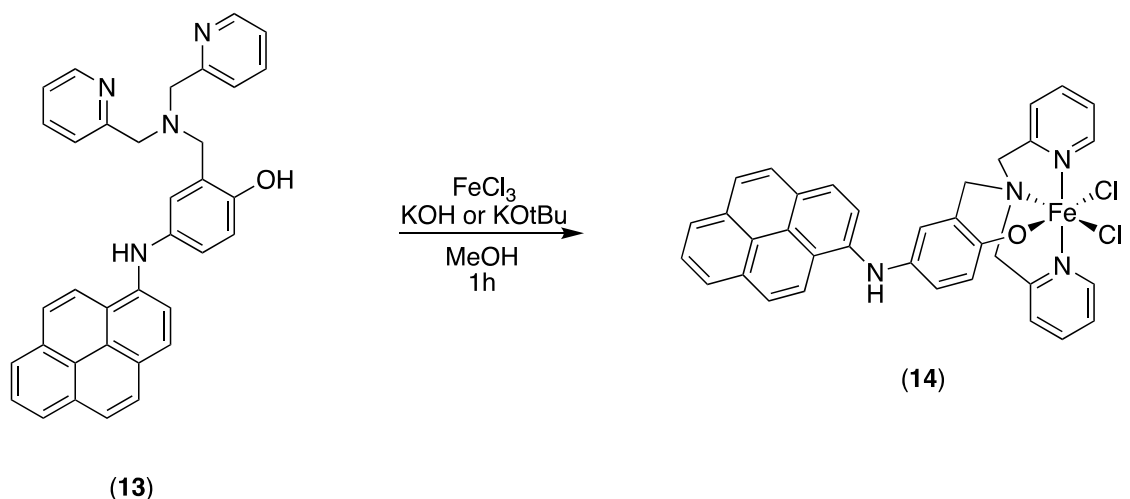


Figure 3.7. Synthesis of pyrene-functionalized iron polypyridyl complex ($[\text{FeCl}_2(\text{L-Py}_3)]$, **14**).

Synthesis of $[\text{FeCl}_2(\text{L-Py}_3)]$ (**14**)

Compound **14** was synthesized using a modified literature procedure (Figure 3.7).⁶ To a solution of **13** (0.17 g, 0.32 mmol) in 5 mL DCM was added a solution of $\text{FeCl}_3 \cdot 6\text{H}_2\text{O}$ (0.09 g, 0.32 mmol) in 5 mL MeOH followed by addition of either KOH or KOtBu (0.02 g, 0.32 mmol or 0.04 g, 0.32 mmol) in 5 mL MeOH. The solution immediately turned green with a visible precipitate. The reaction was stirred at room temperature for 1 hour and then placed in the refrigerator to cool overnight. After filtering the mixture, the solid was collected and washed with cold MeOH (3 x 10 mL), and the filtrate was evaporated to dryness. Crystallization of both samples was attempted using a variety of methods: [liquid-liquid diffusion of either toluene, pentane, or diethyl ether into a concentrated solution of **14** in either DCM, CH_3CN , or nitrobenzene], [vapor diffusion of diethyl ether into a concentrated solution of **14** in DCM], [slow evaporation of a concentrated solution

of **14** in DCM], and [slow cooling of a concentrated solution of **14** in either DCM or CH₃CN].

Electrochemistry Experiments

Cyclic Voltammetry

All electrochemical experiments were performed under an atmosphere of Ar using a CH Instruments 620D potentiostat with a CH Instruments 680 Amp booster. Cyclic voltammograms were acquired using a standard three-electrode cell. A saturated calomel reference electrode (SCE) was used for all experiments. Prior to each acquisition, the platinum auxiliary electrode was polished using 0.05 μm alumina powder paste on a cloth-covered polishing pad, followed by rinsing with water and acetonitrile. The glassy carbon working electrode (diameter = 0.30 cm) was polished in the same manner and was subsequently added to either the electrochemical cell or catalyst-soak solution depending on the experiment (specific details below). Ferrocene was used as an internal standard to correct for drifting of the reference electrode.

Scan Rate Dependence Study

A polished glassy carbon electrode was soaked overnight in a 0.5 mM solution of **[FeCl₂(L-Py₃)]** in acetonitrile. The electrode was thoroughly rinsed with acetonitrile and added to an electrochemical cell containing 5 mL of 0.1 M

TBAPF₆ in CH₃CN. Cyclic voltammograms were taken from 0.3 to -0.6 V vs. SCE at 200, 400, 600, 800, and 1000 mV/s respectively.

Acid Addition Studies

A polished glassy carbon electrode was soaked overnight in a 0.5 mM solution of **[FeCl₂(L-Py₃)]** in acetonitrile. The electrode was rinsed with acetonitrile and added to an electrochemical cell containing 5 mL of 0.1 M TBAPF₆ in CH₃CN. Cyclic voltammograms, which were taken 10 minutes after addition of the working electrode, were taken without acid and after additions of 10, 20, 30, and 40 μ L of either trifluoroacetic acid (2.0 M) or p-toluenesulfonic acid (0.2 M). The working electrode was polished and resoaked overnight in **[FeCl₂(L-Py₃)]** before each scan.

Results and Discussion

Synthesis

Whereas the synthesis of the naphthalene-functionalized ligand was relatively facile, a ligand with pyrene functionality proved to be much more difficult to isolate. Several variants of and syntheses for a pyrene-functionalized polypyridyl ligand were explored (Figure 3.8).

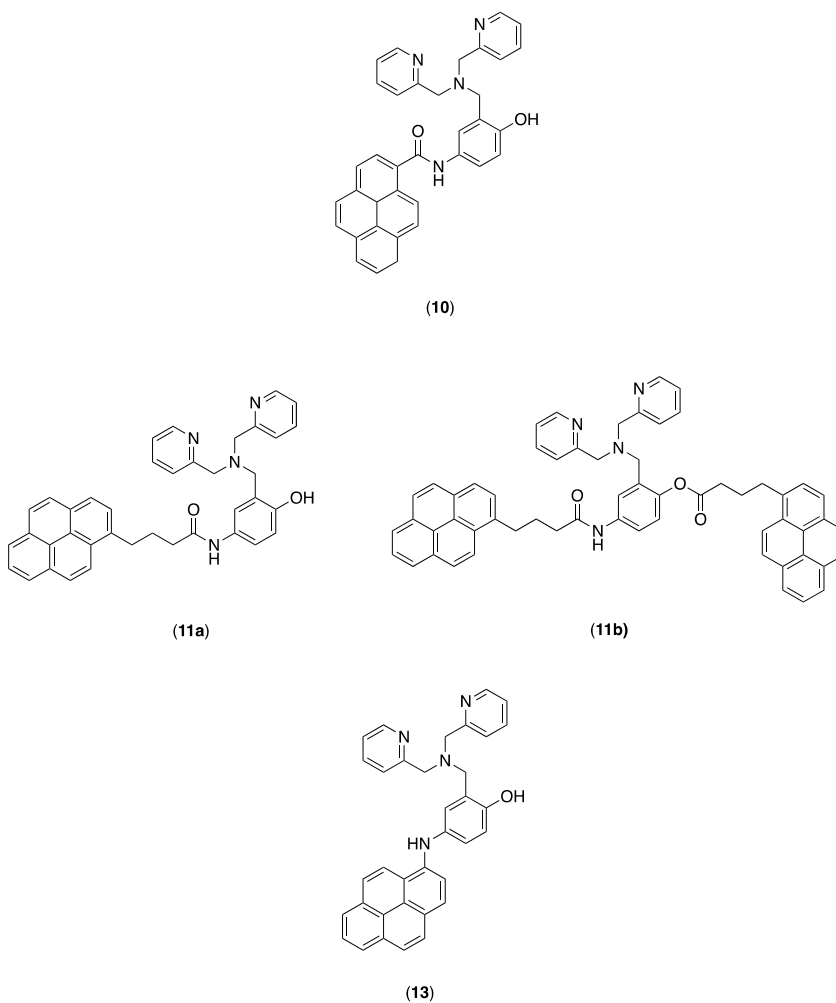


Figure 3.8. Proposed structures for a pyrene-functionalized polypyridyl ligand.

Initial efforts began with using the same framework that had been established in and successful for the synthesis of **L-Nap**: 1-pyrenoyl chloride was prepared from 1-pyrenecarboxylic acid using thionyl chloride and was subsequently coupled with **L-NH₂** through amide-bond formation in the presence of a non-nucleophilic base. However, the suspected product, **10**, was inseparable from the impurities using silica gel chromatography. After testing numerous solvent systems, 97:3 CHCl₃:MeOH was found to provide the best separation, but even this system wasn't adequate enough for proper isolation of the product. Crystallization of the crude product was also attempted unsuccessfully. Difficulties in separation likely arise from similar structural features and electronic properties of the impurities compared to that of the desired product.

Moving on, an alternative, but similar, approach was designed involving coupling 1-pyrenebutyric acid N-hydroxysuccinimide ester with **L-NH₂** through amide-bond formation to give **11a**. Like acyl chlorides, N-hydroxysuccinimide esters are active for amide bond formation whereas normal carboxylic acids would just form salts with an amine. This synthesis method seemed promising, as similar coupling attempts involving this specific pyrene substrate have been successful in the literature.¹ Using this coupling procedure, a single product, though in low yield, was able to be isolated from the remaining starting materials and byproducts.

However, ¹H integrations and ¹³C peak numbers were higher than expected for the proposed structure of **11a** (Figures B3 and B4). Since the aromatic region is quite crowded, the aliphatic region of each NMR provides the

most insight. In this region of the ^1H NMR, there are 12 hydrogens in addition to the 6 on the polypyridyl moiety. This is double the amount of what is expected in the desired product. This same behavior is reflected in the ^{13}C NMR, which shows 3 additional distinct-aliphatic carbons than the anticipated result. These features, in addition to excess aromatic hydrogens and carbons indicate that the isolated compound is a result of coupling of 1-pyrenebutyric acid N-hydroxysuccinimide ester to both the $-\text{NH}_2$ and $-\text{OH}$ groups of **L-NH₂** to give **11b**. This outcome is unexpected, as the phenol is less nucleophilic than the amine.

Despite failing to achieve the desired structure, **11b** was coupled to Fe(III) to examine whether or not the resulting complex could functionalize carbon surfaces and act as a catalyst for the hydrogen evolution reaction. Unfortunately, the resulting complex **12** quickly decomposed. This outcome isn't particularly surprising since, in previous work, instability has been identified in such iron polypyridyl complexes lacking a phenolate moiety, which likely provides stabilization by increasing the coordination number of the ligand set.⁸ Therefore, **12** fails to meet the criteria necessary for its incorporation to an AP system.

Since both methods involving amide bond formation to unite the pyrene unit to **L-NH₂** had been unsuccessful, an alternative approach, known as the Buchwald-Hartwig amination, was utilized to form a carbon-nitrogen bond through the palladium-catalyzed coupling of an amine with an aryl halide (Figure 3.9).⁷ The cycle begins with the oxidative addition of an aryl halide to the Pd(0) catalyst. After the amine coordinates to the complex, it is deprotonated by base

in the solution. The complex then undergoes reductive elimination to give the desired product and regenerate the Pd(0) catalyst.

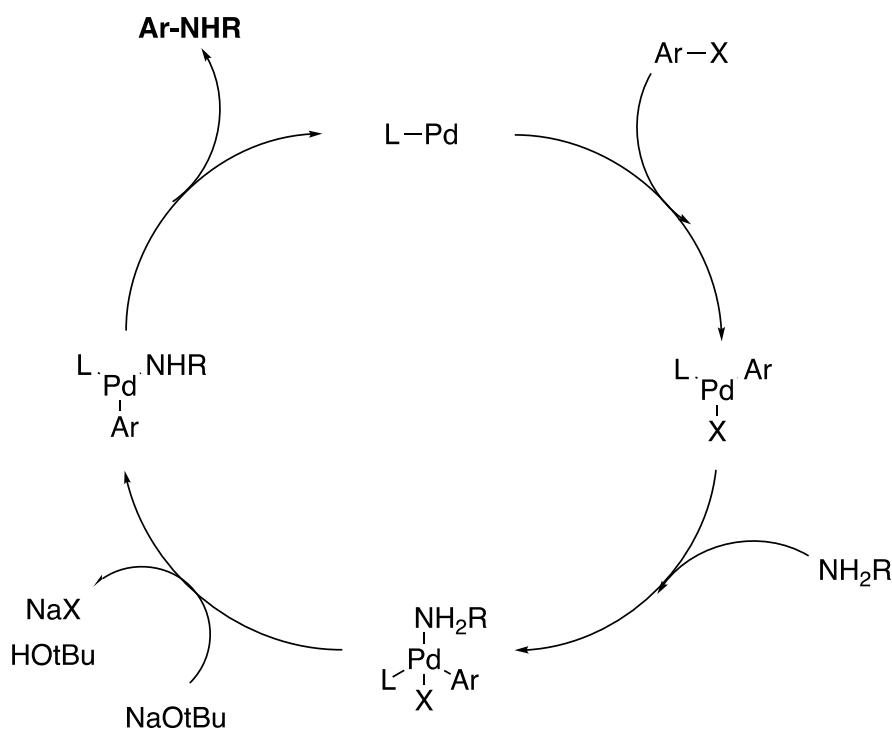


Figure 3.9. Simplified catalytic cycle of the Buchwald-Hartwig amination.

For synthesis of a pyrene-functionalized polypyridyl complex, **L-NH₂** and 1-bromopyrene were used as the amine and aryl halide. Combination of these two substrates under catalytic conditions successfully resulted in the formation of **13**, though in low yield (29%) and with a long reaction time (5 days). Since the ligand was insoluble in MeOH and CH₃CN, complexation of **13** to Fe(III) took place in a 1:2 ratio of DCM:MeOH to ensure dissolution. Upon addition of Fe(III) to **13**, there was a visible green precipitate **14**, which was collected and rinsed with MeOH. Typically, the next stage involves crystallization of the coordination product in order to verify its structure. However, crystallization of **14** was

complicated due to its lack of solubility in applicable solvents, such as DCM, CH₃CN, MeOH, toluene, and acetone. Though more exotic solvents, such as nitrobenzene, were found to dissolve the complex, crystals were unable to be grown. After several rounds of filtration and sonication in DCM, a small fraction of the original precipitate was able to be dissolved in CH₃CN and used for electrochemical examination. However, altered solubility can likely be attributed to chemical changes, such as substitution of a chloro group with hydroxide, in the original structure.

Electrochemical Characterization

Electrochemical examination of **14** began with using cyclic voltammetry to observe and characterize its adsorption behavior on the surface of glassy carbon electrodes. These electrodes were soaked overnight in a concentrated solution of **14** in acetonitrile before being removed, rinsed with CH₃CN, and added to an electrochemical cell containing pure 0.1 M TBAPF₆/CH₃CN. The working electrode was cycled between +0.30 and -0.60 V vs. SCE to observe only Fe(III)/Fe(II) redox couple and to minimize the possibility of reductive desorption. Since there was no redox-active material added to the electrochemical cell, the observed response must come from catalyst adsorbed to the surface of the electrode. Cyclic voltammograms of **14** taken at 200 mV/s show a Fe(III)/Fe(II) reduction at -0.21 V vs. SCE, which is about 100 mV more negative than the naphthalene-functionalized complex **4** (Figure 3.10). However, the anodic peak of **14** lacks clear distinction, indicating some degree of chemical irreversibility.

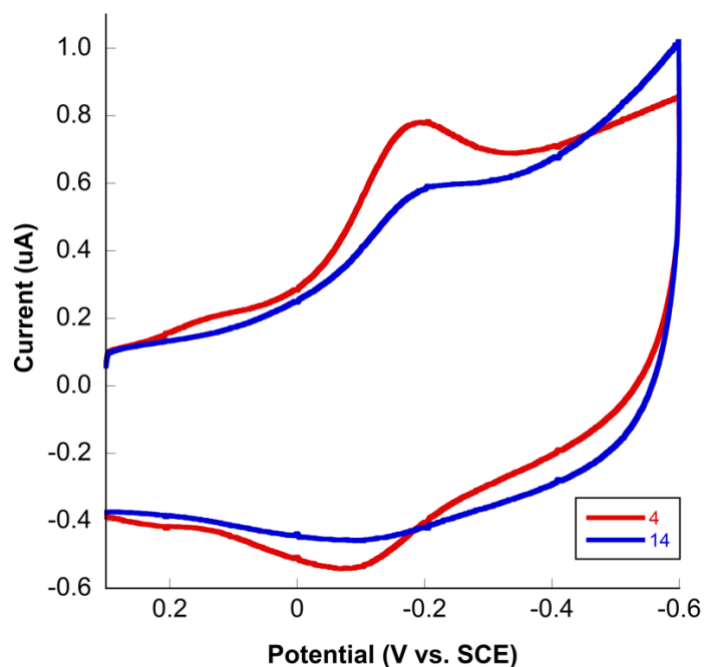


Figure 3.10. Cyclic voltammograms of surface-adsorbed **4** and **14** respectively in 5 mL of 0.1 M TBAPF₆ in CH₃CN at 200 mV/s.

The linearity observed ($R^2 = 0.99975$) in the plot of cathodic peak current (i_{cp}) versus potential sweep rate for **14** confirms that the electrochemical response is due to material adsorbed on the surface of the glassy carbon working electrode rather than from material freely diffusing in solution (Figure 3.11). Using the same analysis demonstrated in Chapter 2, the surface coverage of **14** on the glassy carbon electrode at 298 K was found to be 3.9×10^{-11} mol/cm², which is almost half of the surface coverage found for **4**. This difference may stem from the larger size of the pyrene anchor, which occupies more space than naphthalene and leads to lower-packing density, as similar behavior was

reported for Goldsmith's naphthalene and pyrene functionalized cobalt complexes.¹

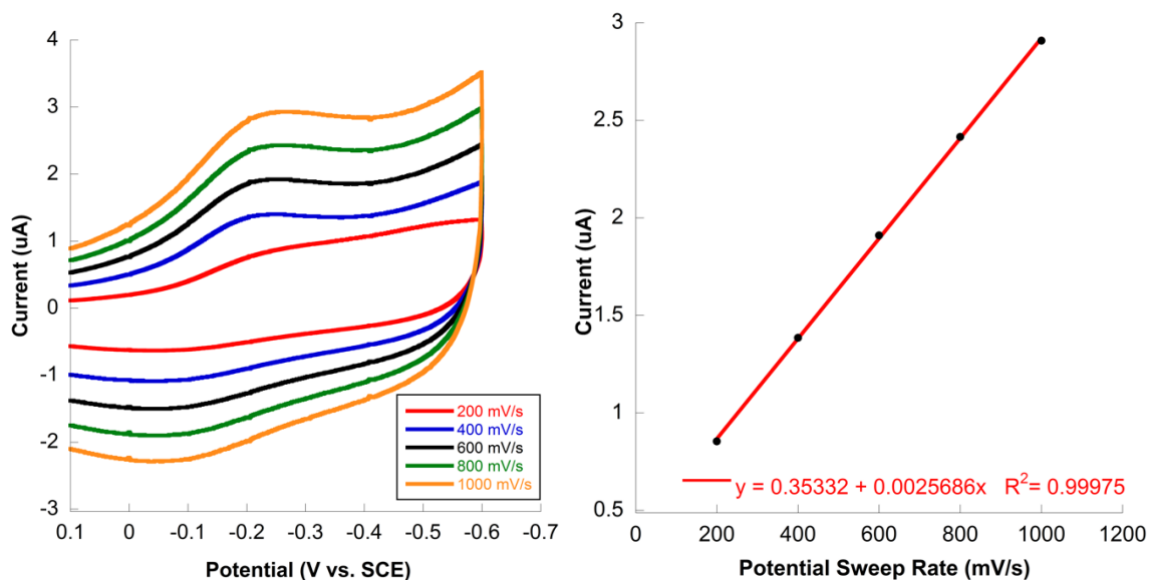


Figure 3.11. *Left:* Cyclic voltammograms of **14** adsorbed to the surface of a glassy carbon electrode in 5 mL of 0.1 M TBAPF₆ in CH₃CN taken at scan rates of 200 – 1000 mV/s. *Right:* Cathodic peak current versus potential sweep rate for **14**.

Electrocatalytic Proton Reduction: TFA Additions

Whereas **4** demonstrated high activity for proton reduction upon TFA addition, **14** proved to be a much weaker electrocatalyst. In the presence of TFA, a shift, corresponding to the protonation of the phenol group, in the Fe(III)/Fe(II) redox couple from -0.21 to +0.10 V vs. SCE is observed for **14** (Figure 3.12). However, no proton reduction was detected in the [TFA] = 0.4 – 1.6 mM range, which contrasts the behavior of **4**. In the window of [TFA] = 4.0 – 16.0 mM, a small irreversible catalytic wave is observed at -1.00 V vs. SCE, and the magnitude of this wave increases with [TFA]. However, at [TFA] >16 mM, the irreversible wave diminishes, likely as a result of desorption. Further

quantification is complicated by the presence of obscuring, unanticipated signals, which likely arise from impurities present in the uncrystallized material.

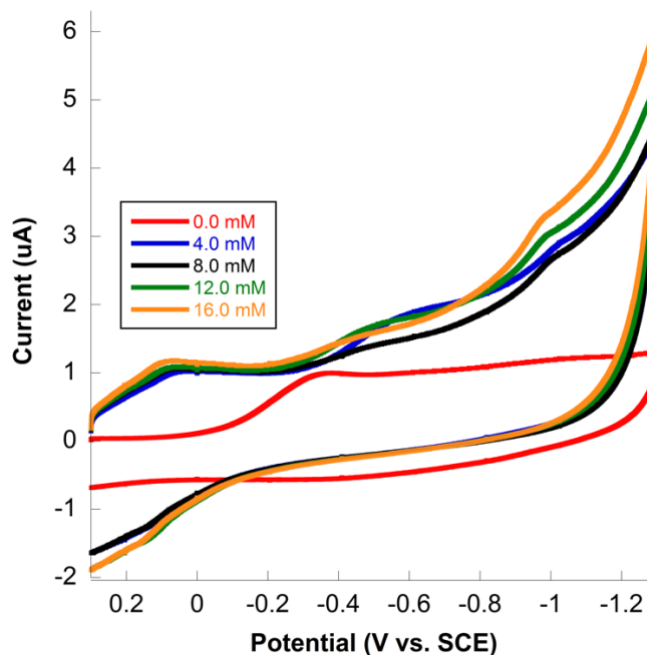


Figure 3.12. Cyclic voltammograms of surface-adsorbed **14** in 5 mL of 0.1 M TBAPF₆ in CH₃CN at 200 mV/s without acid (red) and in the presence of increased concentrations of TFA. A small catalytic reduction is visible at -1.00 V vs. SCE.

Electrocatalytic Proton Reduction: Tonic Acid Additions

In addition to TFA, tonic acid was tested as proton sources for hydrogen generation catalyzed by **14**. Similar to the TFA additions, proton reduction activity at all acid concentrations was inferior to that of **4**. A small irreversible peak corresponding to proton reduction is visible at -0.93 V vs. SCE in the presence of 0.4 mM tonic acid (Figure 3.13). However, the size of this peak decreases as the concentration of tonic acid increases, which is the same behavior as that observed for **4** and is likely the result of desorption.

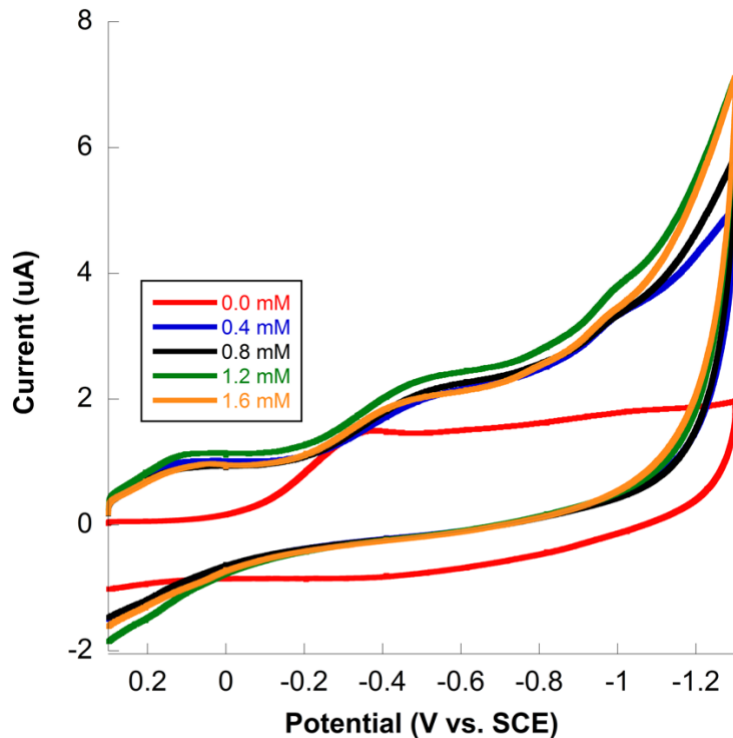


Figure 3.13. Cyclic voltammograms of surface-adsorbed **14** in 5 mL of 0.1 M TBAPF₆ in CH₃CN at 200 mV/s without acid (red) and in the presence of increased concentrations of toxic acid.

Conclusion

This reported work focuses on the synthesis, adsorption behavior, and electrocatalytic abilities of a pyrene-terminated iron polypyridyl complex for the functionalization of carbon surfaces. Several variants of and syntheses for a pyrene-functionalized polypyridyl ligand were explored, and such ligand was successfully synthesized via a palladium-catalyzed amination, which allowed for the coupling of **L-NH₂** to 1-bromopyrene. The ligand was complexed to Fe(III), but the desired compound was unable to be crystallized.

Electrochemical examination of the crude precipitate shows that the pyrene functionality of **14** allows for its successful adsorption onto carbon

surfaces, which is indicated by a linear relationship between i_{cp} and the potential sweep rate. The surface coverage of **14** on a glassy carbon electrode was found to be 3.9×10^{-11} mol/cm², which is almost twice as low as the surface coverage found for **4**.

Furthermore, **14** acts as a weak electrocatalyst for proton reduction; upon addition of TFA, an irreversible catalytic wave corresponding to proton reduction is observed at -1.00 V vs. SCE, though higher acid concentrations are needed to achieve such activity in comparison to **4**. Instability is observed at high concentrations of TFA (>16 mM) and tosic acid (>0.2 mM), both of which lead to desorption of the complex from the electrode surface.

Future Directions

As it currently stands, the insoluble nature of **14** complicates its crystallization, characterization, and electrochemical examination. Additionally, the synthesis of the ligand itself requires long reaction times and is low-yielding. Therefore, the value and functionality of the pyrene complex could be enhanced by revisiting and modifying the ligand synthesis. One avenue to explore is the incorporation of a carbonyl group, which may elevate both the ligand's and complex's solubilities. This could be accomplished through the synthesis of a polypyridyl compound with carboxylic acid functionality. The carboxylic acid group could then be converted to an acid chloride using a chlorinating reagent and successively coupled with 1-aminopyrene to give the desired ligand (Figure 3.14).

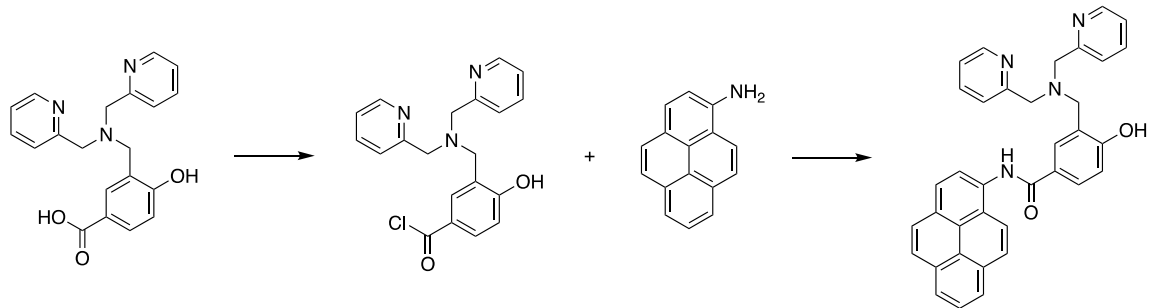


Figure 3.14. Alternative synthesis for a pyrene-functionalized polypyridyl ligand.

In terms of the naphthalene-functionalized complex, work should be directed towards its use in a photocatalytic system since its function as a carbon-surface modifier and electrocatalyst has been established. Particularly, design for a heterogeneous AP system could involve the non-covalent adsorption of both **4** and fluorescein, previously shown to adsorb to carbon surfaces via pi-stacking, on SWCNTs (Figure 3.15).¹⁰ With TEA as an electron donor and under irradiation with visible light, this linked system has the potential to be highly active for hydrogen generation, as it would overcome the diffusion issue that is seen in similar homogeneous systems.

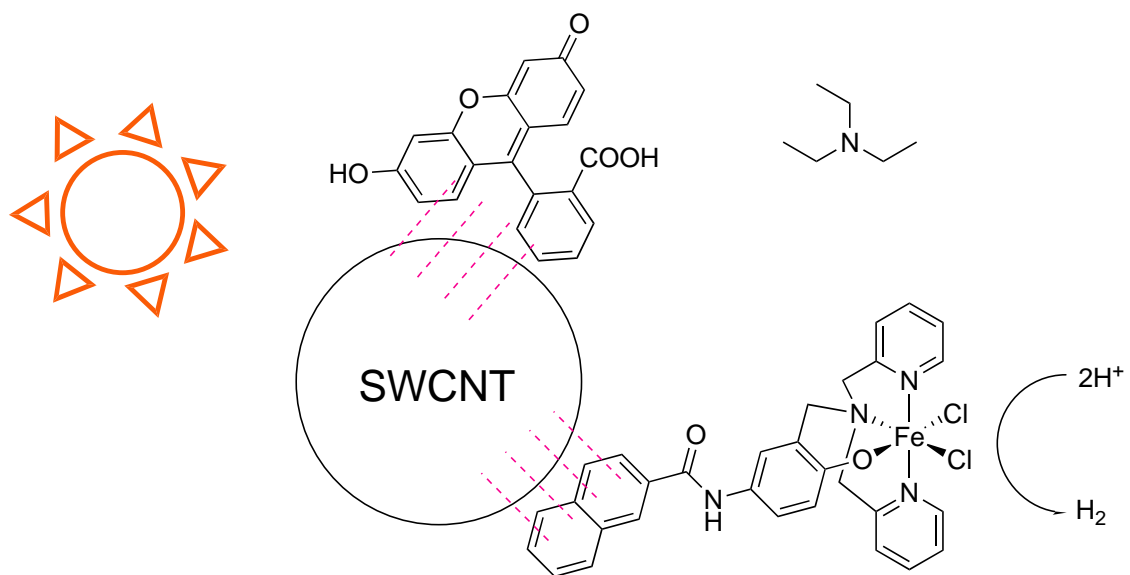


Figure 3.15. Proposed heterogeneous AP system incorporating **4** as the catalyst.

References

1. Smith, H. L.; Usala, R. L.; McQueen, E. W.; Goldsmith, J. I. Novel Polyaromatic-Terminated Transition Metal Complexes for the Functionalization of Carbon Surfaces. *Langmuir*, **2010**, 26 (5), 3342-3349.
2. Yakout, S. M.; Daifullah, A. A. M.; El-Reefy, S. A. Adsorption of Naphthalene, Phenanthrene and Pyrene from Aqueous Solution Using Low-Cost Activated Carbon Derived from Agricultural Wastes. *Adsorption Science and Technology*. **2013**, 31 (4), 293-302.
3. Hartley, C. L.; DiRisio, R. J.; Screen, M. E.; Mayer, K. J.; McNamara, W. R. Iron polypyridyl complexes for photocatalytic hydrogen generation. *Inorg. Chem.* **2016**, 55, 8865-8870.
4. Zhang, W. Dye-Sensitized TiO₂ Modified with Iron Polypyridyl Catalyst for Photocatalytic Hydrogen Evolution. *Master's Thesis, College of William and Mary*. **2016**.
5. Tamminen, J.; Lappalainen, K.; Laihia, K.; Maenttaeri, P.; Salo, H.; Kolehmainen, K. ¹³C NMR spectral assignments of 3 α ,3' α -bis(arylcarboxy)-5 β -cholan-24-oic acid ethane-1,2-diol diesters: new lithocholic acid-based molecular clefts. *Magn. Reson. Chem.* **1999**, 37 (2), 163-165.
6. Race, N. A.; Zhang, W.; Screen, M. E.; Barden, B. A.; McNamara, W. R. Iron polypyridyl catalysts assembled on metal oxide semiconductors for photocatalytic hydrogen generation. *Chem. Comm.* **2018**, 54, 3290-3293.
7. Wolfe, J. P.; Buchwald, S. L. Scope and limitations of the Pd/BINAP-catalyzed amination of aryl bromides. *J. Org. Chem.* **2000**, 65 (4), 1144-1157.
8. Schiffman, Z. R.; Margonis, C. M.; Moyer, A.; Ott, M.; McNamara, W. R. Tridentate bis(2-pyridylmethyl)amine iron catalyst for electrocatalytic proton reduction. *Inorganica Chim. Acta.* **2020**, 503, 119394.
9. Yau, Y.; Li, G.; Ciston, S.; Lueptow, R.; Gray, K. Photoreactive TiO₂/Carbon Nanotube Composites: Synthesis and Reactivity. *Environ. Sci. Technol.* **2008**, 42 (13), 4952-4957.
10. Nakayama-Ratchford, N.; Bangsaruntip, S.; Sun, X.; Welsher, K.; Dai, H. Noncovalent functionalization of carbon nanotubes by fluorescein-polyethylene glycol: supramolecular conjugates with pH-dependent absorbance and fluorescence. *J. Am. Chem. Soc.* **2007**, 129 (9), 2448-2449.

Appendix B

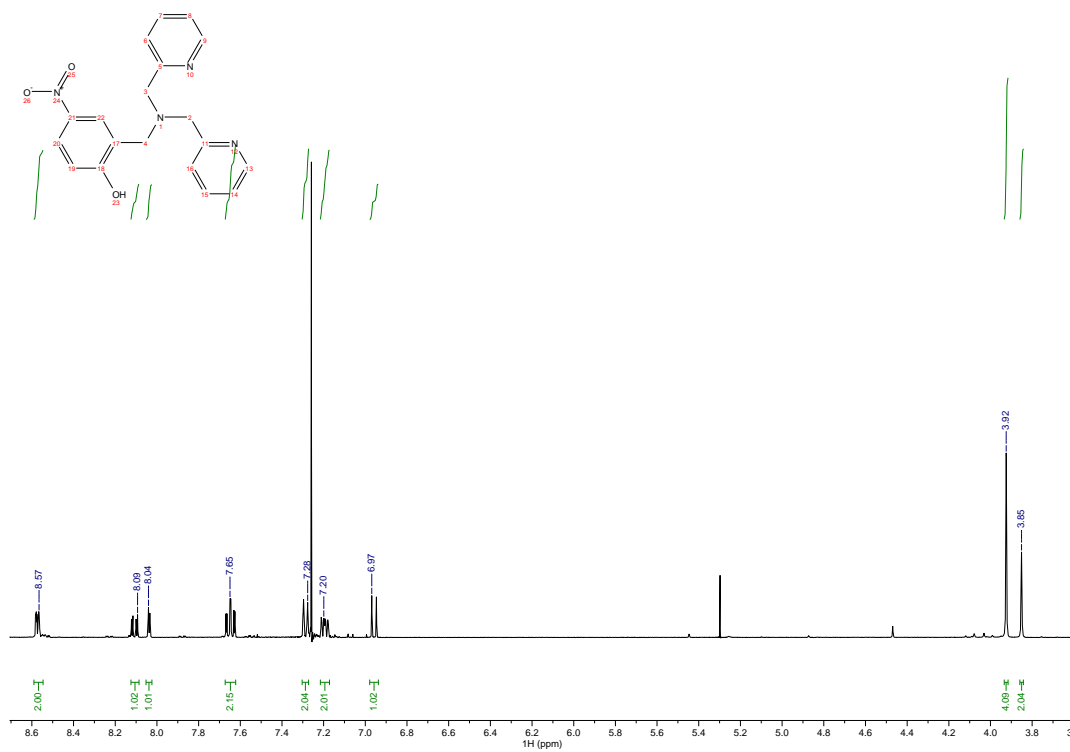


Figure B.1. ^1H NMR spectrum of **1** with integrals in green.

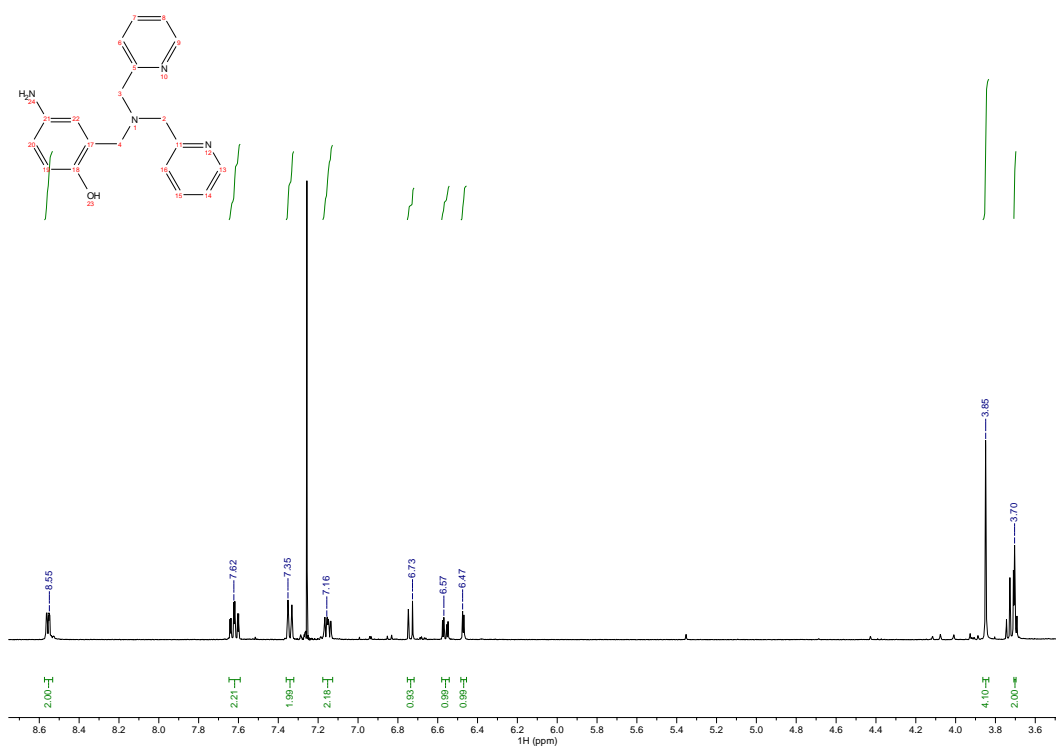


Figure B.2. ¹H NMR spectrum of **2** with integrals in green.

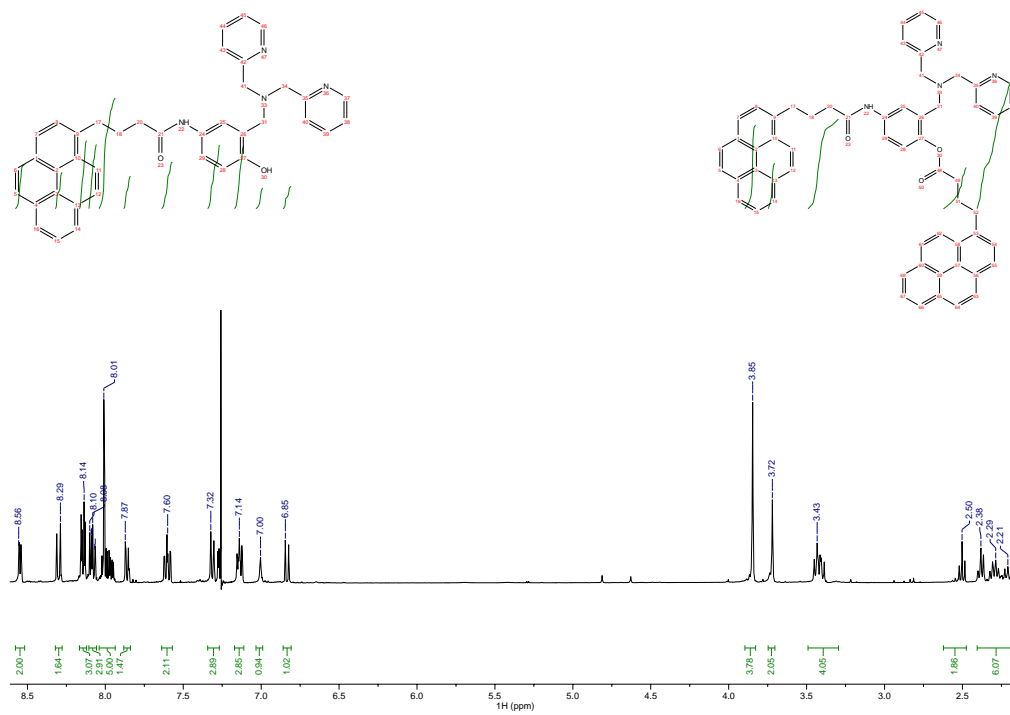


Figure B.3. ¹H NMR spectrum of **11b** with integrals in green. The desired (**11a**) and hypothesized (**11b**) products are displayed in the top left and right corners respectively.

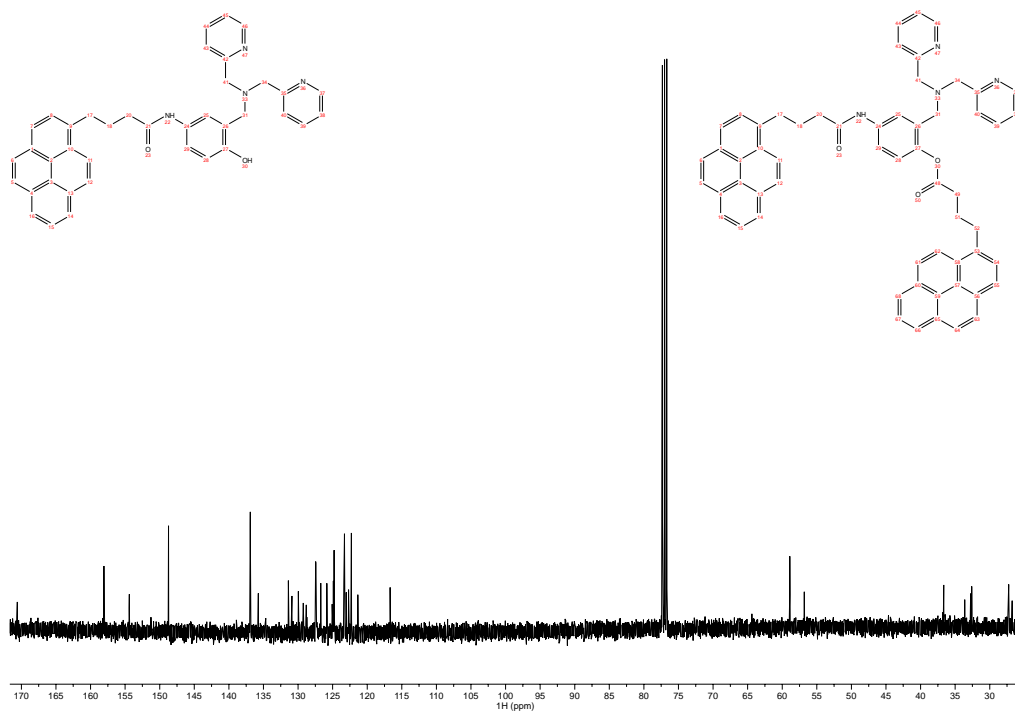


Figure B.4. ^{13}C NMR spectrum of **11b**. The desired (**11a**) and hypothesized (**11b**) products are displayed in the top left and right corners respectively.

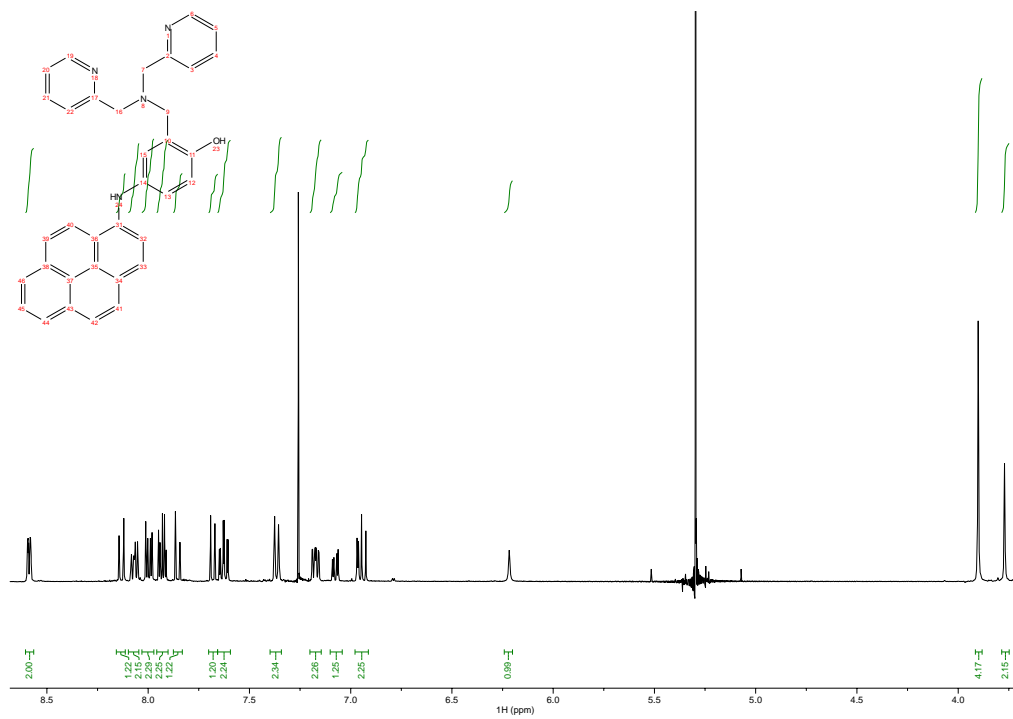


Figure B.5. ¹H NMR spectrum of **13** with integrals in green.

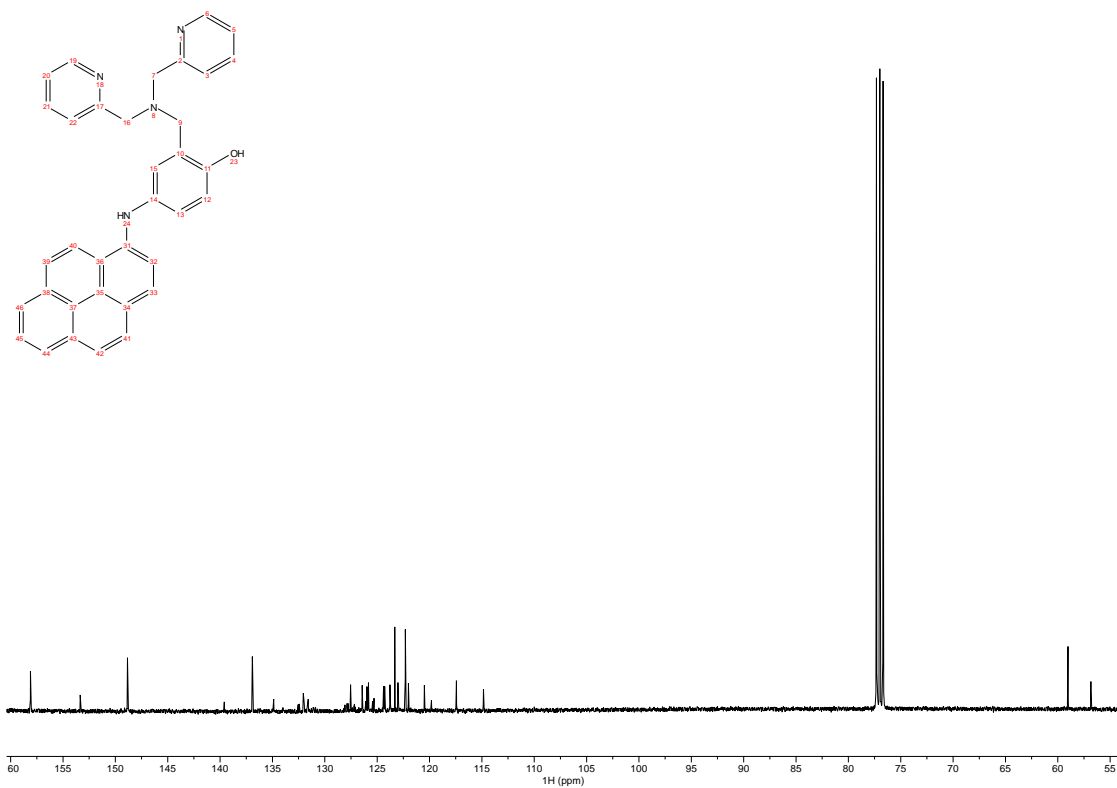


Figure B.6. ^{13}C NMR spectrum of **13**.